INFORMATION TO USERS

This manuscript has been reproduced from the microfilm master. UMI films the text directly from the original or copy submitted. Thus, some thesis and dissertation copies are in typewriter face, while others may be from any type of computer printer.

The quality of this reproduction is dependent upon the quality of the copy submitted. Broken or indistinct print, colored or poor quality illustrations and photographs, print bleedthrough, substandard margins, and improper alignment can adversely affect reproduction.

In the unlikely event that the author did not send UMI a complete manuscript and there are missing pages, these will be noted. Also, if unauthorized copyright material had to be removed, a note will indicate the deletion.

Oversize materials (e.g., maps, drawings, charts) are reproduced by sectioning the original, beginning at the upper left-hand corner and continuing from left to right in equal sections with small overlaps. Each original is also photographed in one exposure and is included in reduced form at the back of the book.

Photographs included in the original manuscript have been reproduced xerographically in this copy. Higher quality 6" x 9" black and white photographic prints are available for any photographs or illustrations appearing in this copy for an additional charge. Contact UMI directly to order.

UMI

A Bell & Howell Information Company
300 North Zeeb Road, Ann Arbor MI 48106-1346 USA
313/761-4700 800/521-0600

Université d'Ottawa · University of Ottawa

Monopole Antennas for Microwave Catheter Ablation of the Myocardium

by
Angeline Blais

A thesis submitted to the
School of Graduate Studies and Research
in partial fulfillment of the requirements for the degree of

Master of Applied Sciences

Ottawa-Carleton Institute for Electrical Engineering

Department of Electrical Engineering
Faculty of Engineering
University of Ottawa

September, 1996

Abstract

We investigate monopole antennas at 2.45 GHz for microwave ablation of the myocardium. Three geometries are considered: open-tip, dielectric-tip, and metal-tip. Their performance is compared using a theoretical model of the antenna radiation in lossy media. The model is implemented using the Galerkin Finite Element Method in the frequency domain. Calculations are made for the magnetic field, the reflection coefficient, and the power deposition pattern of the antennas immersed in normal saline.

The theoretical results are confirmed using experimental measurements of the reflection coefficient and temperature profiles of several prototypes. The temperature profile measurements are made using a phantom tissue with properties similar to those of normal saline. There is good agreement between the experimental and numerical results. The antenna characteristics suggest that the metal-tip monopole best fulfills the requirements of catheter ablation. It has the advantage of having uniform heating along the length of the antenna and an exposed metallic part useful to record electrocardiograms. The computer model is then used to compare metal-tip monopoles of different dimensions and to determine design trade-offs.

Acknowledgment

First and foremost, I thank my thesis supervisors, Dr. S. Labonté and Dr. L. Roy, for their supervision, advice, and encouragement throughout this degree. I also thank Dr. A. Thansandote, G. Gajda, and D. Lecuyer of the Radiation Protection Bureau of Health Canada for the use of their laboratory facilities and equipment as well as for their advice on experimental measurements.

Many thanks to Martin Lee for his help in building the prototypes used in this research and for other technical support.

I am grateful to my peers, Marquis, Andrew, Raja, Hassan, Nick, Yin Lan, Ming, Xizhen, Joey, and all the others for the lively discussions that have enlightened the long hours spent at school.

To Cyril, I wish to express my gratitude for his continual support, patience, and belief in my capabilities. And last but not least, special thanks to my mother Monique, my father Leo, and my brother Eric for their encouragement.

Contents

Abstract i

Acknowledgment ii

1 Introduction 1

1.1 Motivation 1

1.2 Objectives and Approach 2

1.3 Organization of the Thesis 3

2 Background 5

2.1 The Heart 5

2.1.1 Physiology of the Heart 5

2.1.2 Cardiac Arrhythmias 8

2.2 Catheter Ablation 10

2.2.1 DC Ablation 11

2.2.2 RF Ablation 14

2.3 Microwave Ablation 17

2.3.1 Description 17

2.3.2 Literature Review 18

2.4 Conclusion 24

3 Monopole Antennas 25

3.1 Monopole Geometries Studied in this Thesis 25

3.2 Physical Model 27
3.3 Mathematical Model 28
3.3.1 Field Equations 29
3.3.2 Reflection Coefficient 31
3.3.3 SAR Patterns 32
3.4 King's Theory on Antennas in Matter 33
3.5 Conclusion 34

4 Numerical Treatment **36**
4.1 Finite Element Method (FEM) 37
4.1.1 Boundary-value problems 38
4.1.2 Galerkin Method 38
4.1.3 FEM Using the Galerkin Method 39
4.2 Formulation of the Monopole-Myocardium Problem Domain 40
4.2.1 First Step: Discretization of the Domain 41
4.2.2 Second Step: Selection of interpolation functions 41
4.2.3 Third Step: Application of the Galerkin Method 43
4.2.4 Fourth Step: Boundary Conditions 46
4.3 Description of the Programs 47
4.3.1 FDFEM 48
4.3.2 FEMGRID 49
4.3.3 FDGRID 50
4.4 Validation 50
4.5 Conclusion 52

5 Experimental Measurements **54**
5.1 Return Loss Measurements 54
5.1.1 Equipment 54
5.1.2 Prototype Construction 55
5.1.3 Saline Solution 56
5.1.4 Reflection Coefficient Measurements 57

5.2 Temperature Distribution Measurements 58
5.2.1 Equipment 58
5.2.2 Procedure 61
5.3 Conclusion 64

6 Phantom Tissue **65**
6.1 Complex Permittivity Measurements 65
6.1.1 Theory 66
6.1.2 Materials and Methods 69
6.2 Fabrication of the Phantom Tissue 70
6.2.1 Materials and Method 71
6.2.2 Final Recipes and Their Electrical Properties 72
6.3 Conclusion 73

7 Study of Monopole Antennas for Microwave Ablation **74**
7.1 Modeling of Monopoles 75
7.1.1 Magnetic Field 75
7.1.2 Reflection Coefficient 77
7.1.3 Heating Patterns 77
7.1.4 Discussion 81
7.2 Optimization of the MTM 81
7.2.1 Magnetic Field 82
7.2.2 Reflection Coefficient 82
7.2.3 Heating Patterns 82
7.2.4 Discussion 86
7.3 Future Work 90

8 Conclusion **92**

Bibliography **94**

List of Figures

2.1 A schematic representation of the heart showing its principles structures. Taken from [1, p. 81]. 6
2.2 The conduction system of the heart. Adapted from [1, p. 90]. 8
2.3 Mechanism of DC ablation. Taken from [11,p.63]. 13
2.4 The factors involved in the creation of a lesion using RF energy via a catheter positioned on the endocardium. Adapted from [6,p.406]. 15
2.5 Geometry of the helical antenna and its region of heating. 19
2.6 Geometry of the whip antenna inserted in a teflon catheter and its region of heating. 21
2.7 Geometry of the folded dipole antenna. Taken from [34]. 22
2.8 Geometry of the cap-choke antenna. From [38]. 22

3.1 Monopole antennas: a) dielectric-tip monopole (DTM),b) open-tip monopole (OTM), and c) metal-tip monopole (MTM). 26
3.2 Illustration of the use of the monopole applicator. 27
3.3 The feeding coaxial cable and monopole in cylindrical coordinates. 29
3.4 The magnitude of current along a) an open-circuited and b) a short-circuited transmission line [54]. 35

4.1 Example of a nonuniform mesh. 38
4.2 FEM Solution Domain for the OTM configuration. 42
4.3 Mesh of the domain for a MTM configuration. 43

4.4 Illustration of the outward unit vector and its direction cosines for the divergence theorem. 45
4.5 Magnitude of the magnetic field along a section of a short-circuited coaxial line. 51

5.1 Experimental set-up for the measurement of the reflection coefficient. 57
5.2 Experimental set-up and details of the split-block experiment. 62

6.1 The open-ended probe and its equivalent circuit. 67

7.1 Magnitude of H_ϕ around the a) DTM, b) OTM, and c) MTM. The inner and outer conductors of the coaxial cable are at $r = 0$ and $r = 0.84$ mm respectively. 76
7.2 Reflection coefficient for a) OTM, b) DTM, and c) MTM. The solid curves are calculated, the discrete points are experimental. 78
7.3 Calculated SAR patterns at $r = 1.5$ mm for a) OTM, b) DTM, and c) MTM. Curves are normalized to 30 kW m^{-}3. Curve a) peaks at 1.13. 79
7.4 Temperature distribution of the DTM, OTM and MTM produced in Phantom 1. 80
7.5 H_ϕ for 3 MTM's: a) $l = 6.5$, $t = 4$ mm. b) $l = 10$, $t = 4$ mm, and c) $l = 13$, $t = 4$ mm. 83
7.6 Numerical calculations of the magnitude of the reflection coefficient for MTM a) $l = 6.5$, b) $l = 10$, c) $l = 13$, and d) $l = 16$. 84
7.7 Reflection coefficient for MTM a) $l = 6.5$, $t = 4$ mm, b) $l = 10$, $t = 4$ mm. c) $l = 13$, $t = 1$ mm, d) $l = 13$, $t = 2$ mm, and e) $l = 13$, $t = 4$ mm. 85
7.8 Normalized SAR at $r = 1.5$ mm for all MTM's at a) $l = 6.5$, b) $l = 10$, c) $l = 13$, and d) $l = 16$ mm. In each case the dotted line is for $t = 1$, the solid line for $t = 2$ and the dash line for $t = 4$ mm. 87
7.9 SAR patterns for $l = 10$, $t = 2$ mm at a) $z = 5$ and b) $z = 10$ mm. 88
7.10 Temperature distribution of the MTM l=6.5, t=4 mm, l=10, t=4 mm, l=13, t=2 mm, and l=13, t=4 mm produced in Phantom 1. 89

List of Tables

3.1 Dielectric constant and conductivity of average muscle, blood, and 9ppt saline at 2.45 GHz. 28

4.1 Comparison of the magnitude of the magnetic field at various radial distances. 53

5.1 MTM configurations chosen to build prototype antennas. 56

5.2 Colour viewed on the LCS for a given temperature. 60

5.3 Regulation of the power delivered in TEM 1 based on reflection coefficients. . 63

5.4 Regulation of the power delivered in TEM 2 based on reflection coefficients. . 63

6.1 Comparison of dielectric constants and conductivities at 2.45 GHz. 72

Chapter 1

Introduction

1.1 Motivation

Microwave (MW) ablation is a non-invasive medical procedure in which MW energy is radiated to destroy small areas of the heart in order to cure cardiac arrhythmias. A similar procedure involving radio-frequency (RF) energy has had much success in the treatment of many types of cardiac arrhythmias. It has been well investigated and well established. However it remains inadequate in the treatment of ventricular tachycardia (a certain type of cardiac arrhythmia that occurs in the ventricles) because of its inability to create lesions sufficiently large and deep to destroy the diseased tissue. The radiant nature of MW energy allows greater tissue penetration and suggests that larger lesions can be produced than with RF energy.

MW ablation was introduced in the early 90s. In preliminary reports, animal studies *in vivo* and *in vitro* were made to determine the feasibility of MW ablation and to compare the lesion size achievable using MW energy with the lesion size achieved using RF energy. The results as to the size of the lesions were mixed and inconclusive. This was mostly due to the inefficiency of the MW radiator used for the ablation. The radiators (antennas) used in these studies were simple adaptations of those used in other medical applications, such as MW hyperthermia and MW balloon angioplasty, and had not been optimized for the MW ablation application. Up to the time this research was undertaken, in 1995, no publications

were available showing the design of an efficient MW antenna for ablation of the myocardium.

This research is motivated by the desire to gain more insight into the design of a MW antenna for MW ablation. It is felt that with a better theoretical insight, an antenna design can be optimized for more efficient radiation into the myocardium and for the creation of well-defined, uniform lesions. More efficient radiation should lead to the creation of lesions sufficiently large for the treatment of ventricular tachycardia.

1.2 Objectives and Approach

The global objective of this study is to investigate variations of a monopole antenna geometry for use in MW ablation treatment. It is desired to find a geometry that best fulfills the requirements of MW ablation. A theoretical approach is used for this investigation because it is more versatile and to some extent simpler than a study based on experimentation alone. Experiments would require equipment and medical expertise that are not readily available, and they would be time consuming and expensive. A theoretical approach on the other hand can easily show the fundamental characteristics of the antennas. Moreover, theoretical results constitute a convenient basis for the evaluation of the efficiency of the antennas.

The ablation problem is very complex for an analytical treatment due to the dissipative properties of blood and muscle tissue. For this reason, a numerical model must be used. The **first objective** is thus to set up a numerical model that is a reasonable representation of the physical reality. A preliminary verification of the computer programs is made using simple examples with analytical solutions. However, experimental measurements are required to aquire confidence in the numerical model and confirm the simulation results. The **second objective** is therefore to establish accurate and reliable experiments that are to be conducted on several prototypes of the antennas. More specifically, the experiments are conceived for measuring the return loss and temperature profiles of the prototypes. A novel approach for performing the temperature profile measurements is presented which calls for the use of a gelatinous solution (phantom tissue) having specific electrical properties. Thus, to fulfill the second objective, an investigation into the preparation of the phantom tissue and complex permittivity measurements is also required.

The **third objective** of the thesis is to carry out a series of simulations using the model and to conduct the experimental measurements. The results are used to assess and compare the characteristics of the monopoles and to identify the geometry that best fulfills the requirements for MW ablation. An optimization of this geometry, using simulations and measurements of various configurations, highlights its achievable performance which allows some conclusions to be drawn about the monopoles.

1.3 Organization of the Thesis

Chapter 2 of this thesis presents background information of a medical nature. The physiology of the heart is reviewed followed by a brief description of catheter ablation techniques using direct-current, RF, and MW. The requirements of MW ablation for efficient antenna radiation are discussed and a literature review of MW ablation is given, highlighting the types of antennas used in these studies.

In Chapter 3, the geometries of three monopole antennas under study are presented. A model of the monopole antennas is presented in terms of their physical surroundings and the differential equation that governs them. The mathematical developments required for the theoretical analysis of the antennas are given. Finally, as a preliminary step to the study, a prediction of the current distribution on the antennas is made using a theory of insulated antennas.

Chapter 4 contains all the necessary details of the numerical treatment used on the monopole antenna model. The application of the Finite Element Method is discussed. The computer programs required are described. The last section contains a preliminary validation of the programs using examples having an analytical solution.

Chapter 5 describes the methodology used for the experimental measurements performed on prototypes of the antennas. These measurements are made to confirm the results of the reflection coefficient and SAR patterns obtained from the numerical model. Details of the equipment, procedure, and test set-up used for the measurements of the reflection coefficient and temperature profiles are given in the first and second sections respectively.

Chapter 6 provides the details of the gel required for the temperature profile measure-

ments. The theory of complex permittivity measurements is investigated. The procedures used for these measurements and for developing the recipes of the gel are discussed. The final recipes and the properties of the gel are given.

The results obtained from the numerical model and from the experimental measurements are presented in Chapter 7. Plots of the magnetic field, the reflection coefficient, the heating patterns, and the temperature profiles are given. The three monopole antenna geometries are compared in a discussion of the results and an optimization is performed on the most attractive geometry. The various results and tradeoffs encountered in the optimization are presented and discussed.

The final chapter concludes by summarizing the work done and suggesting avenues for further work.

Chapter 2

Background

The goal of this chapter is to provide information indicating the scope of the research at hand. Since the focus of this work is the treatment of cardiac arrhythmias, it seems fitting to start with a brief overview of the physiology of the heart and the genesis of cardiac arrhythmias. The methods of treatment using catheter ablation techniques are then presented. A review is given of the ablation procedure using direct-current, radiofrequency, and microwave energy.

2.1 The Heart

In this section, we take a quick glance at the physiology of the human heart. A description of its electrical activity proves to be helpful in understanding cardiac arrhythmias. We then proceed to the origin and causes of arrhythmias along with a discussion of their various types. This section serves a secondary purpose of introducing and defining technical terms that are specific to this area of research. The information that follows is based on the references [1–6].

2.1.1 Physiology of the Heart

The heart is a muscular organ which plays a crucial role in the circulatory system of the human anatomy. It can be considered as a mechanical pump timed by an electrical system, and fueled by blood. An attempt is made here to give a succinct description of the parts and functions of the heart. For greater details, any of the references cited before may be consulted.

The heart is composed of walls made of muscle fibers called *myocardium*. A thin membrane, the *endocardium*, lines the inside surface of the myocardium. The *pericardium* is a thin membranous sac that encloses the heart. The inner most layer of the pericardium is called the *epicardium*.

The heart can be divided into two similar halves, each half containing two cavities (see Figure 2.1). The top cavities are called *atria* (sing. atrium), and below are the *ventricles*. The atria are thin-walled receiving chambers. They collect blood before it is passed to the ventricles. The ventricles are thicker muscular chambers used for pumping blood out of the heart. The two halves of the heart are separated by a median septum. The *atrial septum* separates the two atria and the *ventricular septum* separates the ventricles.

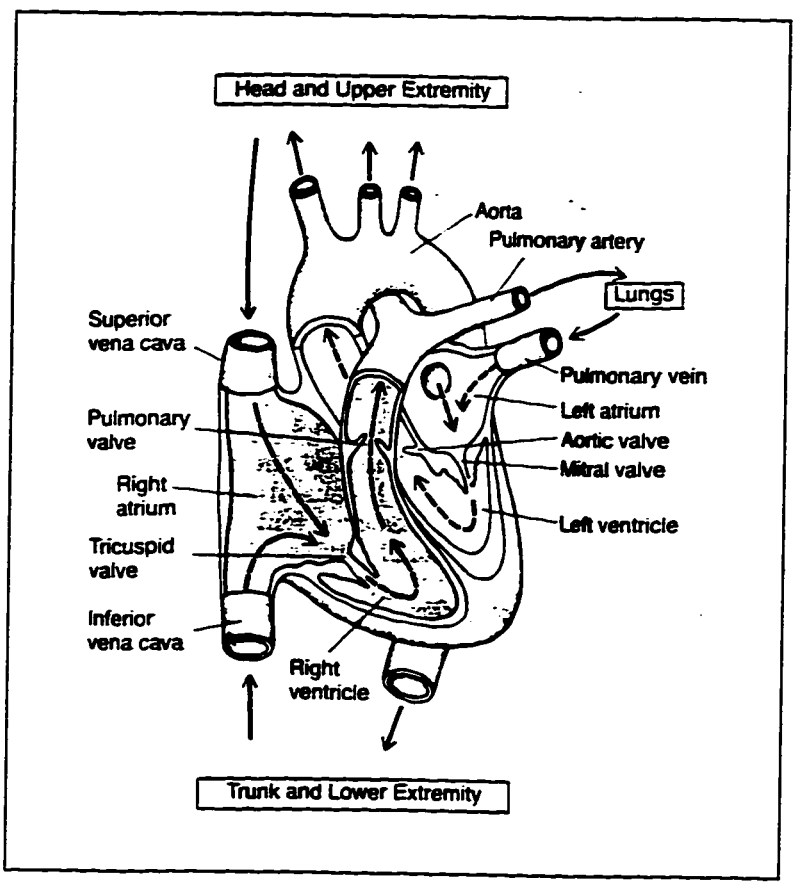

Figure 2.1: A schematic representation of the heart showing its principles structures. Taken from [1, p. 81].

As shown in Figure 2.1, blood is conducted in and out of the heart by means of the great vessels. The right atrium receives deoxygenated blood from the head and upper extremity of the body through the *superior vena cava*, and deoxygenated blood from the trunk and lower extremity of the body flows through the *inferior vena cava*. The *pulmonary vein* brings oxygenated blood from the lungs into the left atrium. Once the atria are full, contraction occurs and the blood is pushed to the respective ventricle. A contraction of the ventricles will let blood flow from the left ventricle to the upper and lower body by the *aorta*, and from the right ventricle to the lungs by the *pulmonary artery*. The flow of blood is regulated by passive valves at the orifice of the chambers. They allow the passage of blood in one direction and prevent flowing backwards when the pressure gradient is reversed.

The contraction of muscles (including myocardial fibers) in the human body occurs in response to a sudden flow of ions in both directions across their membrane. The flow of ions causes a change in voltage difference across the membrane; a phenomenon called *depolarization*. Although there are many regions in the heart that contain cells capable of spontaneous rhythmic depolarization, the contraction of myocardial fibers is normally initiated at the *sinuatrial (SA) node*. In the normal heart, cells in the SA node are the quickest to depolarize to threshold and initiate impulse; therefore, the SA node is usually the dominant pacemaker. It is located in the superior lateral wall of the right atrium near the opening of the superior vena cava (see Figure 2.2).

In the normal heart, depolarization travels freely over the myocardium but cannot travel between the atria and the ventricles because they are separated by a layer of isolating fibrous tissue. The only conduction pathway between the atria and the ventricles constitutes the *atrioventricular (AV) node* and the *bundle of His*. The AV node is made of the same kind of tissue as the SA node. It is located in the posterior septal wall of the right atrium. The bundle of His is a strand of specialized myocardium that creates an electrical connection between the AV node the ventricles. The bundle of His passes from the AV node into the ventricular septum where it separates into a left branch and a right branch. Both branches run subendocardially down either side of the septum toward the apex and connect with the *Purkinje fibers*. The Purkinje fibers are responsible for diffusing the excitation to all parts of the ventricular myocardium in a semi-simultaneous contraction of all ventricular fibers.

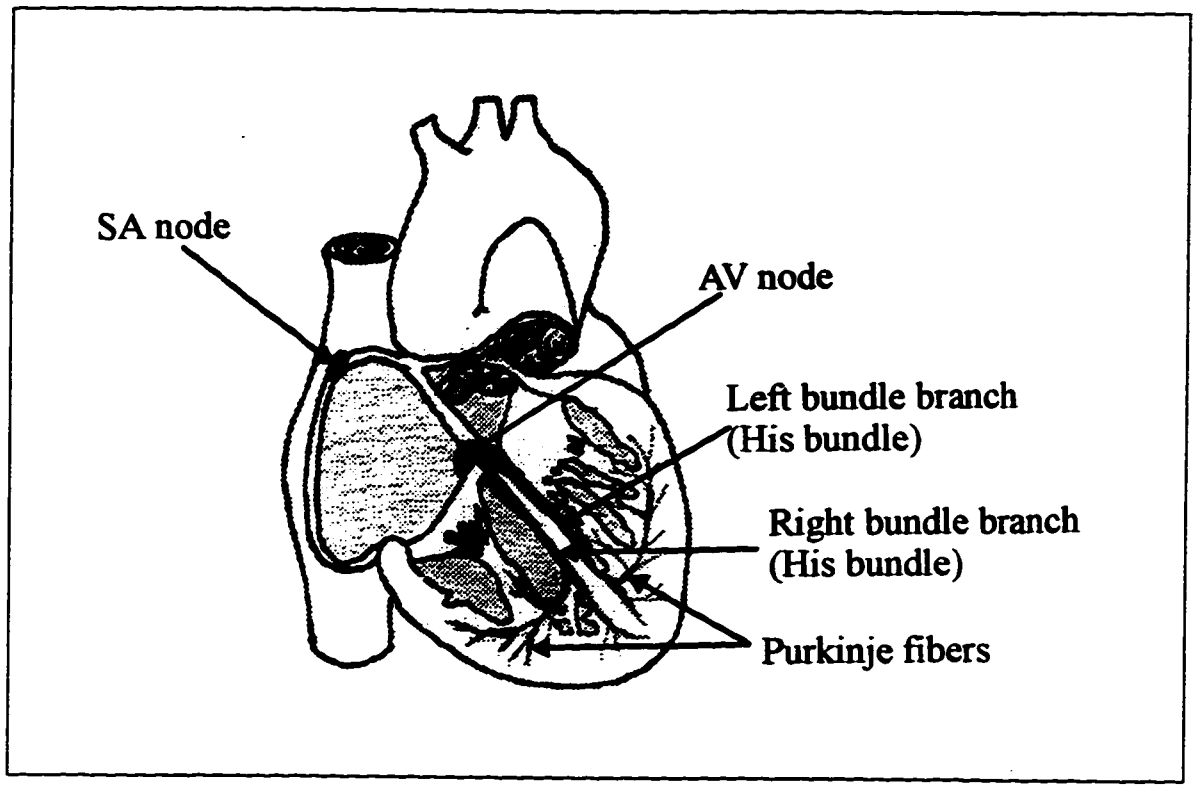

Figure 2.2: The conduction system of the heart. Adapted from [1, p. 90].

An impulse generated from the SA node travels rapidly across both atria by myocardial conduction, and reaches the AV node. While atrial contraction occurs, the impulse propagation from the atria to the ventricles is delayed by the AV node. After its release, it propagates along the bundle of His to the Purkinje fibers and ventricular contraction is initiated. The period of atrial and ventricular contraction, called *systole*, is followed by a rest period, called *diastole*, where all chambers are relaxed.

2.1.2 Cardiac Arrhythmias

For efficient blood pumping, the heart must beat at a regular pace. Any anomaly of the heart that results in loss of synchronization or departure from the normal pace, is called an arrhythmia. The principle tool for the analysis and diagnosis of arrhythmias is the electrocardiogram. Electrocardiograms are graphical representation of the electrical activity in the heart. They are obtained by recording the electrical potentials between two electrodes placed

on the skin (or one inside the heart) on opposite sides of the heart. Electrical potentials are generated by the propagation of cardiac impulses.

The following is a definition of terms often used in the diagnosis of arrhythmias. *Bradycardia* signifies abnormally slow pulse rate. *Tachycardia* signifies excessively rapid heart action. The term *heart block* is used when there is partial or complete interruption of the conduction pathway between the atrium and the ventricle so that they beat independently of each other. In a complete heart block, some part of the His bundle or the Purkinje fibers may begin discharging rhythmically (at a much lower rate than the SA node) and initiate the pacemaking of the ventricles. A permanent artificial pacemaker is required to maintain adequate ventricular excitation.

There are a multitude of different types of arrhythmia each with its own specific name. However, in most cases they can be grouped into two very general types of arrhythmias: those that are initiated by an *ectopic focus* and those that are caused by *reentry*.

An ectopic focus is a cell or group of cells that develops spontaneous rhythmic activity and imposes its pace on the rest of the heart. Ectopic foci are prone to spontaneous and sometimes rapid firing and account for tachycardia. They can occur both in the atria and the ventricles. Possible causes of ectopic foci are local areas of ischemia[1], small calcified plaques, or toxic irritation caused by drugs, nicotine, caffeine, or other agents.

After muscle depolarization, there is a short refractory period before repolarization. During this period, the muscle is not conductive. Hence, when an impulse has traveled through its entire path, it dies out and the heart awaits a new signal to begin in the SA node. However, under certain conditions, the impulse may follow a path of reentry into the muscle that has already been excited. Reentry may be caused by zones where the velocity of the impulse decreases or the refractory period is shortened. In these zones, by the time the impulse finishes its path, the muscle will be repolarized and ready for depolarization, allowing an endless cycle. Reentry between the atria and the ventricles may also become established if an alternate conduction pathway, other than the bundle of His, is formed between them.

Some authorities place active arrhythmias into two fundamental categories: supraventricular and ventricular. Supraventricular arrhythmias are those that occur in the atria or

[1]Ischemia: A temporary lack of blood supply in an organ or tissue.

the AV junction, such as atrial premature beats, junctional premature beats, AV accessory pathways, AV nodal reentrant tachycardia, multifocal atrial tachycardia, atrial flutter, and atrial fibrillation. Ventricular arrhythmias occur in the ventricles. Representative of this category are ventricular premature beats, ventricular tachycardia, bundle branch reentry, and ventricular fibrillation.

Cardiac arrhythmias can take form of an irregular or an accelerated pace resulting in less effective blood pumping. In the worst case, ventricular fibrillation can occur. It consists of an unsynchronized contraction of all ventricular fibers due to the existence of several ectopic foci or instantaneous patterns of reentry caused by electric shock or ischemia. During fibrillation no blood is pumped and unless emergency procedures are undertaken, it is fatal.

Some types of arrhythmia can be controlled by pharmaceutical treatment but when it is not possible, the abnormal tissues responsible must be ablated. This was traditionally accomplished surgically by resecting or cryogenically freezing the section of tissue. Now it is done using catheter techniques which consist of introducing a catheter in a great vessel and advancing it into the heart chamber. Some form of energy is then applied through the catheter, destroying the tissue in contact with its tip. Although this method is more complex in terms of accessing the tissues and effectively delivering the energy, it has proven to be less traumatic for the patient and less expensive than surgery. Recent research has also been conducted which led to positive findings on the advantages of using catheter ablation techniques to replace pharmaceutical treatments with the additional benefit of lower long-term cost and no side-effects [7]. The various methods proposed for catheter ablation are reviewed in the next section.

2.2 Catheter Ablation

Catheter ablation of internal heart tissues presents an interesting advantage over conventional techniques. It eliminates the need for open-heart surgery, and in some cases, drug therapy. Cardiac catheterization consists of advancing a catheter through one of the great blood vessels (through an arm, a leg, or the neck) and into the heart chambers, usually under fluoroscopic control (real-time X-rays).

Catheters are measured in units called French (F). Three French correspond to a diameter of 1 mm. Catheters used for cardiac ablation are typically 6 to 8 F [6]. They usually consist of an insulated conductor exposed at the distal end to form an electrode. The proximal end is connected to an electronic instrument for the recording or generation of electrical signals. To locate the site to be ablated, electrocardiograms are recorded via the catheter which is moved around until a suitable pattern of electrical activity is identified.

Many methods of ablation amenable to catheter use in cardiology have been proposed. One method is called direct-current (DC) ablation and consists of applying a high-current pulse at the target site. Another approach is radio-frequency (RF) ablation which involves the flow of an alternating current through the tissue to be ablated. Direct current shocks and radiofrequency energy are by far the most extensively used at present in treating patients, and their efficacy and safety have been well documented. Other methods still under investigation include laser, ultrasound, and microwave treatments. In laser techniques, a laser beam is used to vaporize the target. Ultrasound ablation uses a transducer to produce a mechanical pressure wave (at frequencies higher than 18 kHz) that is propagated through the medium. Microwave (MW) ablation consists of radiating high frequency energy into the tissue. Of all the alternative treatments investigated to replace DC and RF ablation, MW ablation seems to be the most feasible and inexpensive. The following sections present a review of DC, RF, and MW ablation. A description and references for laser and ultrasound ablation, as well as cryoablation and intracoronay ethanol ablation, can be found in a review article by Nath and Haines [8].

2.2.1 DC Ablation

Direct current shock was the first type of energy used for transcatheter cardiac ablation. Investigations in using DC shock to achieve AV block began in the early 1980s. Since then, DC ablation techniques have been used to ablate the AV junction, accessory pathways and ventricular ectopic foci. Despite its relative success this procedure is not free of complications and can have very serious side effects. DC ablation techniques are well documented with a great deal of information and many references in books edited by Fontaine and Scheinman [9. 10].

Description

The DC ablation procedure consists of an electrical discharge through a catheter to produce a local burn. The standard technique uses a conventional cardiac defibrillator (consisting of a capacitor and an inductor in series) to deliver 40–400 J of total energy per pulse with peak voltage and current of 1–3 kV and 40–60 A for a duration of less than 10 ms (and as little as 10 μs) [5, 8, 11]. Two modes of discharge can be used: the *unipolar mode* where the current flows between a catheter electrode at the distal end of the catheter and a large dispersive grounded electrode positioned on the chest or the back of the patient; and the *bipolar mode* where the discharge is produced between two catheter electrodes near the target.

When high energy direct current is delivered to the tip of an electrode catheter, a series of events occurs, resulting in the generation of a shock wave (see Figure 2.3). The delivery first results in temperature increase and causes electrolysis of water into hydrogen and oxygen gas (the plasma is vaporized). An insulating gas bubble develops resulting in an increased impedance (Figure 2.3a). Current continues to flow to the tip of the catheter despite the rise in impedance, which results in a voltage gradient across the bubble. When this voltage gradient reaches a critical value, a flash or arc develops (Figure 2.3b). Once arcing occurs, there is a tremendous rise in temperature, causing the bubble to expand generating a shock wave (Figure 2.3c). The shock wave then causes barotrauma[2] to adjacent cardiac tissue. A combination of three factors are responsible for tissue injury: barotrauma, Joule heating (conversion of electrical energy into thermal energy), and direct electrical injury [6]. This last factor arises from the high-voltage electrical field at the catheter tip which causes irreversible cellular depolarization and injury.

Several investigators [12, 13, 14] have modified DC techniques by creating defibrillators that deliver higher voltages in shorter times, thereby giving a large current density at a lower energy level. A lower energy level eliminates the possible barotrauma caused by the gas bubble formation and arcing.

The lesion size created by the DC ablation technique was found to be directly proportional to the amount of energy delivered (up to 2 cm in depth) [11].

[2]Barotrauma is tissue damage occurring from exploding vapor pockets. It can create unpredictable and potentially serious side effects.

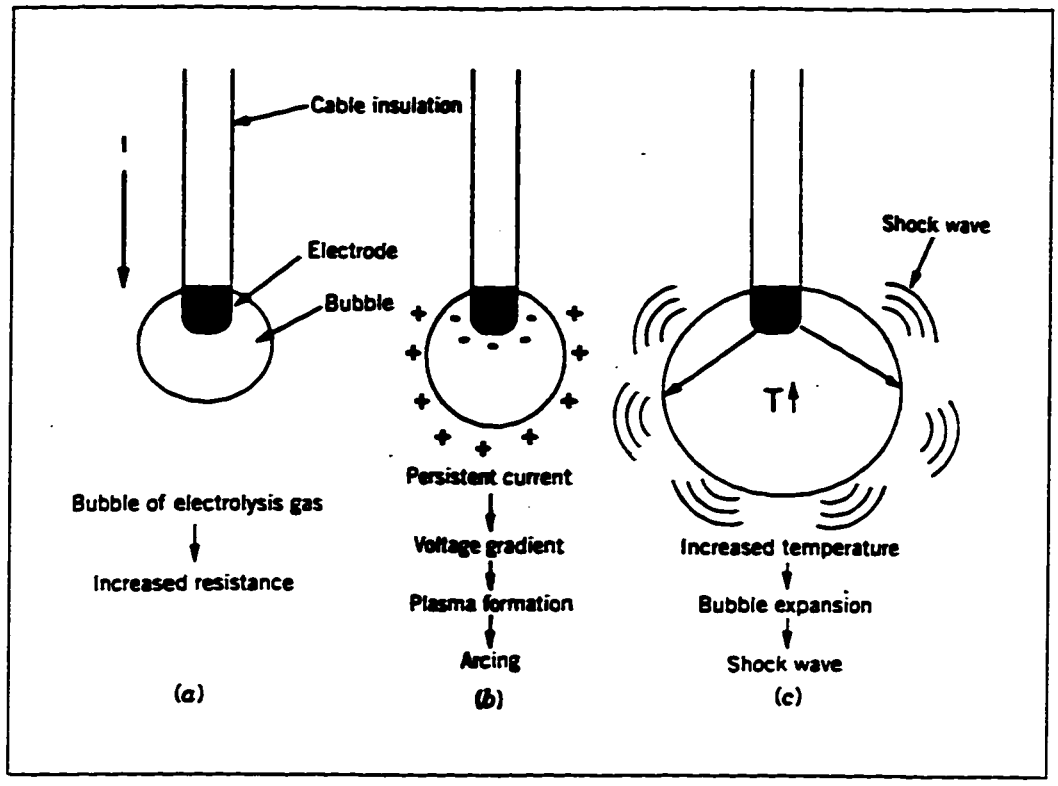

Figure 2.3: Mechanism of DC ablation. Taken from [11,p.63].

Advantages and Disadvantages of DC Ablation

DC catheter ablation is a very attractive alternative to surgery for the treatment of drug refractory cardiac arrhythmias. It is used to create AV block by ablation of the AV junction. The procedure is as successful (greater than 65% success rate [15]), cheaper to perform, and associated with lower morbidity and mortality. However, there is great difficulty in controlling the myocardial damage, and the tissues surrounding the target site are often unnecessarily damaged.

The lesions created during DC ablation present a disadvantage to this technique because they are nonhomogeneous and may themselves be arrhythmogenic. A further disadvantage is the requirement for anesthesia during the intervention because DC current stimulates muscles and nerves. These complications have encouraged the search for other forms of energy that would render catheter ablation safer and more easily controllable.

2.2.2 RF Ablation

Investigations in using radiofrequency energy as an alternative to DC shock for catheter ablation started in the mid 80s. The technique using RF energy rapidly evolved and over the last several years, RF has become the dominant mode of energy delivery in catheter ablation. The efficacy and safety of using this type of energy have been well documented, and many centers in the US and Canada presently use RF ablation on a routine basis. This technique is relatively inexpensive partly due to the fact the RF generators have been available in hospitals for neurosurgery since the late 50s. Very good references that describe the biophysics and pathology of RF catheter ablation can be found in [6, 8, 11, 16]. Detailed references of clinical results using this method of ablation are found in [17, 18, 19].

Description

The RF ablation procedure involves the delivery of an electrical alternating current via a catheter. The current traverses from an ablation electrode located at the distal end of the catheter, through the intervening tissue to a dispersive electrode located on the skin of the patient. RF energy is usually provided by commercially available radiofrequency generators. Typically, the generators are used to deliver about 50 W by a continuous sinusoidal unmodulated waveform at frequencies between 300 and 1000 kHz with a peak voltage usually less than 100 V (40–60 V [11]), and currents of 0.2–0.6 A. The unipolar mode is most commonly used although RF current may occasionally be delivered using the bipolar mode.

The passage of an alternating current through the tissue results in electromagnetic heating that is termed resistive or ohmic heating. Water is driven out of cells resulting in coagulation necrosis. Direct resistive heat production per unit volume, decreases in proportion to the radial distance from the electrode to the fourth power. Because the power density is highest immediately contiguous to the catheter electrode, significant resistive heating only occurs within a narrow (<1 mm) border of tissue in direct contact with the electrode (see Figure 2.4). Deeper tissue heating occurs as a result of the thermal transfer phenomenon that takes place over time. A significant amount of energy transmitted from the generator is also dissipated through the portion of the electrode exposed to blood flow. This is referred to as convective

heat loss. Figure 2.4 illustrates the creation of a lesion using RF energy. As shown on the figure, the catheter is positioned perpendicularly to the ablation site because the energy is dissipated at the tip of the electrode.

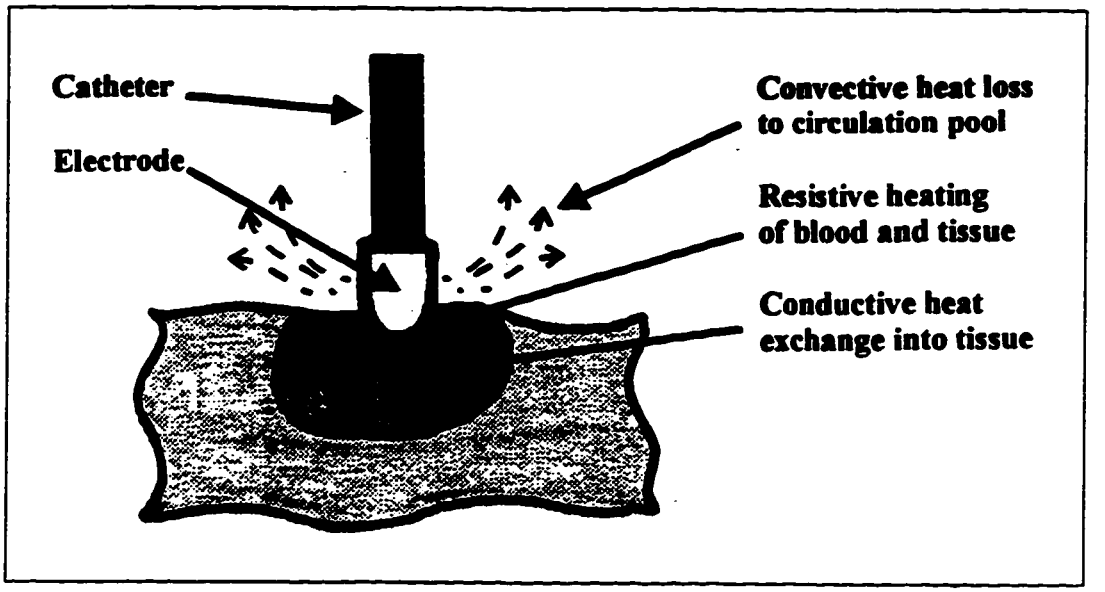

Figure 2.4: The factors involved in the creation of a lesion using RF energy via a catheter positioned on the endocardium. Adapted from [6,p.406].

The RF range (300–1000 kHz) selected for catheter ablation is high enough so that it does not result in cardiac muscle contraction, nervous tissue stimulation, and does not cause cellular depolarization. Therefore, its use is almost painless and free of the risk of ventricular fibrillation.

The isotherm for irreversible myocardial injury at RF is reported in [11] as 48–50 °C. Thus, the region heated above approximately 50°C becomes nonviable and defines the lesion volume. However, the tissue temperature must be kept below 100°C to avoid charring and micro-explosions of subendocardial cells, which may cause complications [6].

There is a linear relationship between delivered power and lesion size. However, the power can only be increased up to a certain limit. When it reaches a certain level, coagulation occurs and the effective electrode surface in direct contact with the myocardium becomes smaller. A smaller surface creates a rise in impedance, and in turn creates a rise in power which

can cause arcing. The maximum lesion size is said to be achieved by heating the catheter electrode at a minimum temperature of 80-90°C (but below 100°C) for 30–40 s [8, 11].

Examination of cardiac tissue sustaining radiofrequency energy injury usually shows a relatively small, homogeneous, and sharply demarcated scar. The homogeneous nature of these lesions suggests that they are less likely to be arrhythmogenic than those created by DC shock. RF energy is also associated with a lower risk of cardiac perforation because of the small size of the lesions.

Advantages and Disadvantages of RF Ablation

RF catheter ablation has become the treatment of choice for many forms of supraventricular tachycardia, with a greater than 95% success rate, and low morbidity and mortality rates [18, 19, 21]. It is also a preferred technique for creating AV block. Although the success rate for this procedure is similar to that obtained with DC ablation, RF ablation is much safer for the reasons listed below:

- The application of RF energy does not cause arcing or barotrauma.
- General anesthesia is not required during RF ablation.
- RF ablation leaves well delineated homogeneous scars with no intact myocardial fibers.
- It is associated with fewer cases of life-threatening complications than DC ablation.
- The RF ablation technique offers better control of the delivery of the energy.

Unfortunately RF ablation is not as successful in treating ventricular arrhythmias. Only two clinical syndromes are reliably cured by RF catheter ablation with greater than 90% success rate. For ventricular tachycardia (VT), it can be difficult to define the area for ablation. The arrhythmia arises from reentry within zones of slow conduction that occur from old myocardial infarction[3]. The reentry circuit may be formed by multiple pathways which may be located at variable depths below the endocardium. In addition, the infarction creates a layer of insulation (low conductivity) between the pathways and the electrode. Since

[3]Infarction: an area of necrosis resulting from a sudden insuffiency of arterial or venous blood supply.

resistive heating depends on conductivity, little heating can occur when the electrode is in contact with a region of low conductivity. Thus the lesions created with RF ablation are inadequate to treat VT. Larger and deeper lesions are required[4].

To summarize, the major limitations of RF ablation are the precise mapping required due to the relatively small size of the lesions, the critical contact between the electrode and the tissue for efficient energy transfer, and the inability to penetrate an insulation layer.

2.3 Microwave Ablation

Research in microwave catheter ablation has been prompted by the inefficiency of lesions created by RF ablation for the treatment of VT. The radiant nature of MW energy suggests that it can penetrate an insulation layer and produce larger lesions than RF energy. Although MW energy has been used for many years in other medical applications such as hyperthermia, it is still under investigation for myocardial ablation and only limited data is available.

In this section, we start with a description of the MW ablation procedure followed by a literature review. The review is focused on the antenna designs used for MW ablation.

2.3.1 Description

The MW ablation procedure involves the delivery of a high frequency current from a MW generator through a coaxial catheter to a radiating antenna. The frequencies used for MW ablation are 915 and 2 450 MHz which are ISM frequencies[5]. At these high frequencies, absorbed MW energy is converted into heat by the dielectric loss mechanism that characterizes biological tissue at microwave frequencies. MW energy causes the oscillation of molecular dipoles (most notably, water molecules) in cells which produces tissue heating. If the heating is high enough, cell death occurs. As with RF, MW frequencies do not induce cardiac muscle contraction or nervous tissue stimulation; therefore, general anesthesia is not required during the procedure.

[4]To treat VT, the lesion size should be of the order of 1 cm in diameter with a penetration depth of 1 to 2 cm, according to [23]

[5]ISM frequencies are frequencies reserved for industrial, scientific or medical purposes.

MW energy can penetrate insulating tissue (i.e. myocardial infarction) since its heating mechanism is dielectric and its radiant nature does not depend on current flow from the ablation electrode to the tissue as in RF ablation. In view of this, the resulting volume of direct dielectric heating is potentially larger than the direct resistive heating achieved with RF energy. Combined with conductive heating, the overall heating can result in increased lesion size.

There are three major components of a clinical MW ablation system; a MW power source, a transmission cable (the catheter) and the antenna. MW power sources capable of delivering high power are commercially available at a relatively low cost. The interface of the MW source and a flexible coaxial transmission line is relatively trivial, even with the small size cables required for ablation. The transmission line must have low power loss and must be resistant to high powers. Cables that meet these requirements are also available commercially.

The most critical element in the design of a MW ablation system is the distal antenna. In order to radiate the incoming power efficiently, the antenna must have a low reflection coefficient at the frequency of operation to avoid excessive heating along the catheter that is caused by reflected power. The antenna must also conform well to the catheter for easy catheterization (i.e. small physical dimensions). It should have exposed metallic parts to record electrocardiograms necessary for its positioning inside the heart chamber. In addition, the antenna should possess a uniform heating pattern to achieve well-defined uniform lesions.

The following presents a literature review of the geometry of the antennas used in the published studies of MW ablation to date. The results obtained in these studies pertaining to lesion formation are also summarized.

2.3.2 Literature Review

Microwave energy has been used for many years in the field of hyperthermia therapy for cancer. The requirements of this treatment are quite different from ablation. It consists of localized heating of tissue by 2–3°C to selectively destroy cancer cells which are less tolerant to a temperature rise than healthy cells (ablation techniques require a temperature rise of 10–20°C to burn the site). Because the application is different, the numerous studies published on antenna designs for hyperthermia are not directly applicable to ablation. The antennas

tend to be too large and too long for cardiac use. They are also used inside a teflon catheter embedded in the tumor, thereby preventing direct electrical contact with the tissue (contrary to cardiac ablation). Nevertheless, these designs have served as a starting point for the design of ablation antennas.

Helical Antenna

Satoh and Stauffer [24] designed a helical antenna for hyperthermia. Its configuration is shown in Figure 2.5. The antenna is made by coiling a wire connected to the inner conductor of a coaxial cable along a section of bare dielectric. The antenna is embedded in a plastic catheter and its overall length and diameter are 11 mm and 1.2 mm respectively, which is small enough for catheter ablation. Heating occurs along the length of the antenna and at its tip.

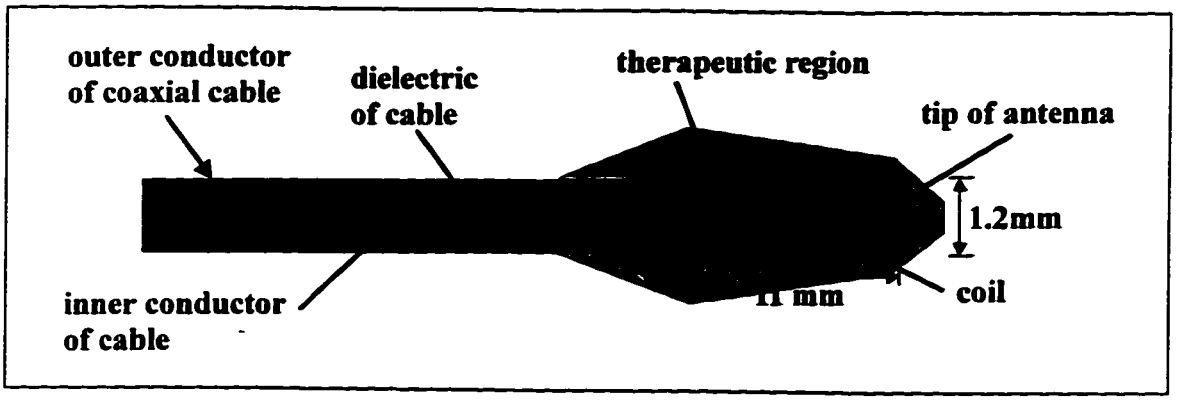

Figure 2.5: Geometry of the helical antenna and its region of heating.

The helical antenna design proved to have a good performance and was adopted for certain hyperthermia treatments [25]. Because of its popularity, it was also used (this time in its bare form) in the first preliminary reports on the feasibility of using MW energy at 915 and 2450 MHz in catheter ablation [26, 27, 28, 29, 30]. Wonnell *et al.* also used a helical antenna design in a comparative study of lesion size created *in vitro* with RF and MW energy. The results found from these studies indicate that the lesions created using MW energy can be several times larger than with RF ablation. However, there are no indications that the antenna geometry gives optimum results. Furthermore, the antenna used in [25] seems too

large for practical use (length 9.5 mm, diameter 10 F) and is relatively complex to fabricate.

Mirotznik *et al.* [31] reported a combined theoretical and experimental study of helical antennas in lossy dielectric. The experimentation was done at 915 MHz with antennas of 2 mm diameter and 30 to 150 mm length (which is too long for catheter ablation). Their study reveals that although such antennas can be designed to have great heating uniformity, their depth of heating is very limited and far less than that of a dipole or monopole of comparable dimensions.

Whip Antenna

Taylor [32] and Paglione [33] both studied a monopole-type configuration (also called whip antenna) for hyperthermia. Its configuration is shown in Figure 2.6. The antenna is constructed by removing a length of the outer conductor at the distal end of a coaxial cable. The length corresponds to a quarter-wavelength in the tissues at the desired frequency (approximately 15 mm at 2.45 GHz) for a good impedance match. The antenna-cable assembly is then inserted into a teflon catheter before usage. The temperature profile of this design as well as results of animal and clinical studies are given in [33]. The results showed that the heating region has a football shape and is mostly concentrated at the junction between the antenna and the feeding coaxial cable (along the length of the antenna). As shown in the figure, no heating occurs near and at the tip of the antenna. This design is of particular interest for ablation because of its simplicity. As discussed shortly, the whip antenna was used in some MW ablation studies but there have been no detailed studies for optimizing its performance.

Other Types of Antennas

Lin *et al.* [34] studied a balun-fed, folded dipole antenna whose configuration is shown in Figure 2.7. The two arms of the dipole are connected to the inner and outer conductor of the coaxial cable. A quarter wavelength conductor sleeve is attached to the outer conductor of the input coaxial cable to form a balun. The dipole and sleeve are completely encapsulated using a thin sheath of silicon rubber. The overall outer diameter and length are 2.4 mm and 24 mm respectively. Contrary to usual antenna design for hyperthermia where the heating

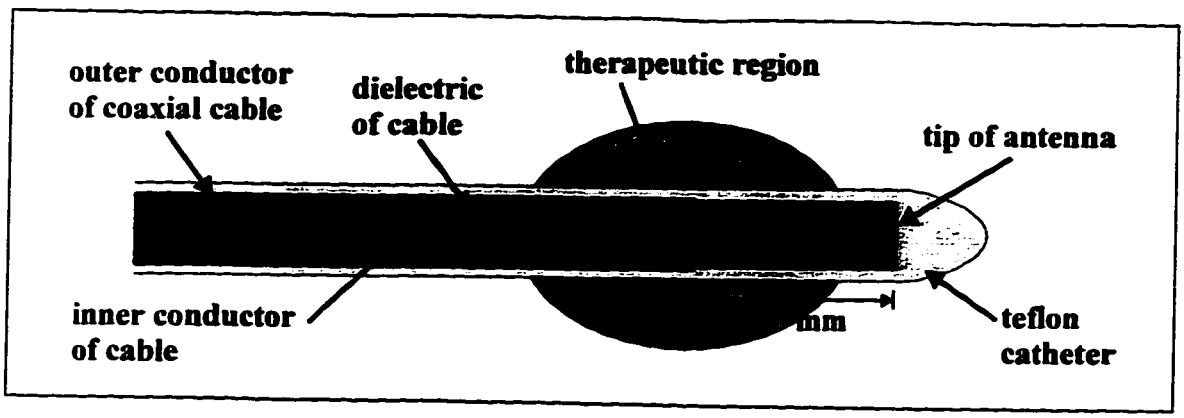

Figure 2.6: Geometry of the whip antenna inserted in a teflon catheter and its region of heating.

occurs along the length of the antenna, this antenna has a heating pattern concentrated at the tip.

Lin extended the use of a folded dipole from hyperthermia to catheter ablation [35, 36]. It was used in preliminary studies of MW ablation, as will be discussed shortly, but there was no mention of how well the antenna performed in terms of reflection coefficient and uniform heating pattern. In a recent study [38], Lin introduces a new design consisting of a cap-choke antenna. Its geometry is shown in Figure 2.8 and its construction is well described in [38]. This antenna has been solely investigated using experimental measurements in phantom tissue, revealing excellent results: -17 dB return loss and a heating pattern concentrated at the tip.

Preliminary Studies of Lesions Creation

The studies on MW ablation published to date are not conclusive on the possible lesion size. In comparative studies of RF and MW lesions, Wonnell *et al.* [25] reported that the MW lesions could be several times larger in volume and penetration depth twice as large. However, Rosenbaum *et al.* [39] found that the lesions created with MW were not larger than those created with RF. In their report, little detail is given of the MW applicators and no theoretical analysis is given to substantiate the experimental findings.

Some *in vitro* and *in vivo* studies of MW catheter ablation were made using both a helical

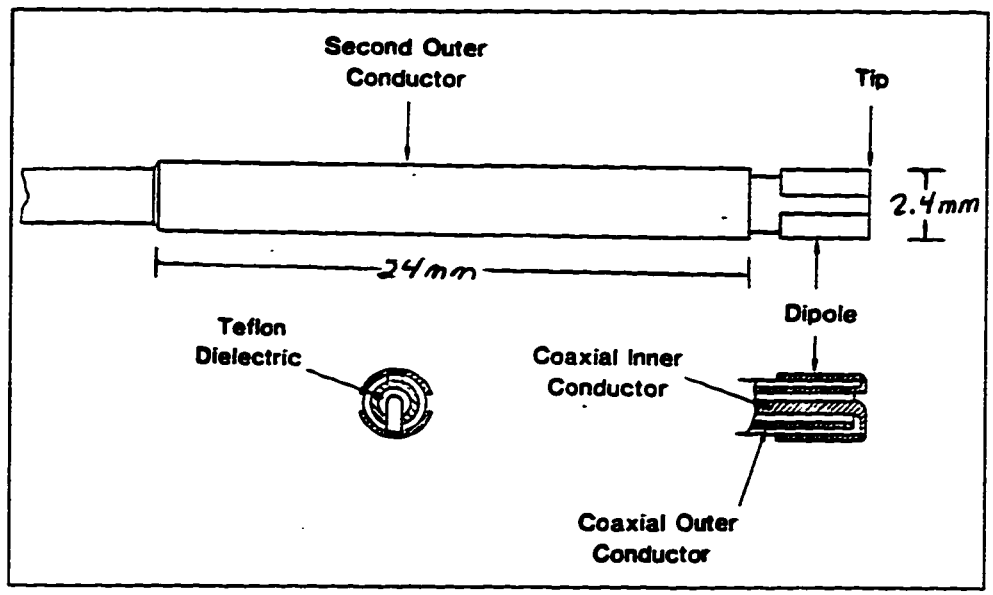

Figure 2.7: Geometry of the folded dipole antenna. Taken from [34].

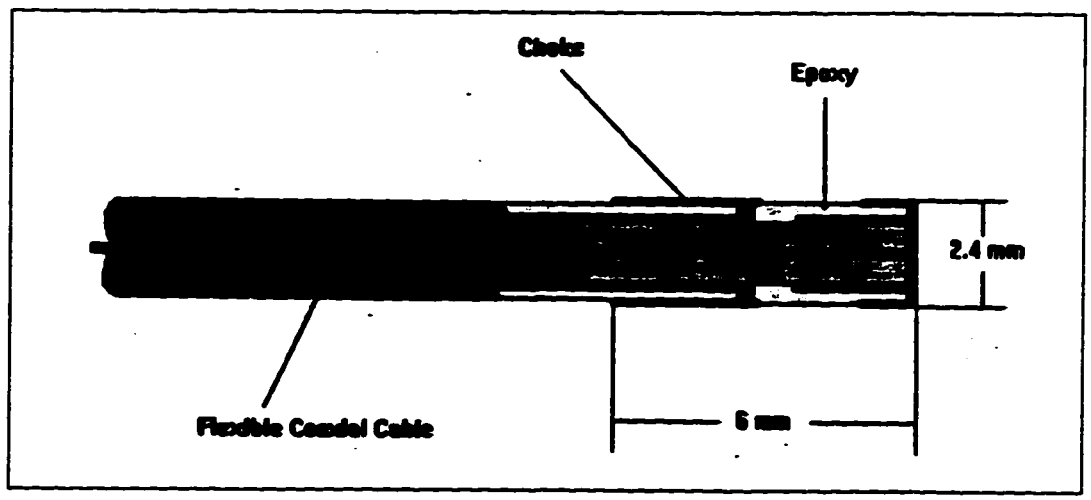

Figure 2.8: Geometry of the cap-choke antenna. From [38].

antenna and a whip antenna [39, 40, 41]. The authors offer no significant comparison of the performance of the antennas. In [40] it is said that both designs were found to have similar tissue temperature profiles and produced lesions of similar size.

In a study of lesions created *in vitro* on porcine ventricles [40], the critical temperature of irreversible damage was found to be approximately 54°C, and the half-time of MW lesion formation was found to be much longer than that of RF. In two other studies of lesion formation in the ventricles of dogs *in-vivo* [27, 26] it was reported that lesion volume varies directly with power and longer applications of MW energy results in larger lesion size.

A helical antenna, designed for 2.45 GHz, was used in [29] to produce AV block in six dogs. Complete AV block was successfully achieved in all six animals. Lin *et al.* also tested the feasibility of producing AV block in a canine model. The folded dipole antenna design was used for this experiment (at 2.45 GHz) and the results were also positive [36]. The feasibility of treating atrial tachycardia in dogs using both 7F helical and whip antennas at 915 MHz was investigated in [41]. All atrial tachycardias were treated successfully. However, there have not been studies on the treatment of VT.

Conclusion of the Literature Review

In MW ablation, the direct tissue contact is not critical which offers a great advantage over RF ablation. MW energy produces spherical, homogeneous and well-demarcated lesions. It also has the potential to create large lesions but only with efficient MW antennas.

In the available studies to date, four antenna designs have been suggested: the helical, whip, folded dipole, and cap-choke antenna. The first three designs are adaptations of those used for hyperthermia. The studies that make use of them are focused on the feasibility and characterization of MW ablation rather than on the performance of the antennas themselves. These same studies allude to the fact that the designs are not optimum and that more research should be made for a more efficient design.

For this reason, a study of three monopole antenna configurations is proposed in this thesis. The configurations are based on the whip antenna because of its simplicity and because its geometry is fairly easy to analyze. The intention of this study is to characterize and compare the monopoles in terms of their performance in a medium having losses similar

to that of the myocardium.

The study conducted by Lin on the cap-choke antenna was published after completion of the investigation reported in this document. The study is very similar to the one conducted here on monopole antennas. However, the performance of the antenna is demonstrated by experimental measurements alone, with no theoretical basis. The monopole antennas in this document are characterized using both experimental measurements and a theoretical analysis which allows a basic understanding of their fundamental characteristics and provides more insight into the problem.

2.4 Conclusion

This chapter describes the nature of cardiac arrhythmias and shows the evolution of catheter ablation techniques for their treatment. The use of RF energy has become very popular because it requires a relatively simple procedure using available equipment and yields good results. However, the lesions created during RF ablation are not sufficiently large to treat certain types of ventricular arrhythmias. The use of MW energy as an alternative seems very promising although much research must be conducted to assess its full potential. The biggest problem with MW ablation at the moment is the need for a good antenna design to achieve efficient energy transfer into the myocardium. In the remainder of this thesis, we address this problem with a study of three monopole antenna geometries in lossy media. The designs in question are introduced in the following chapter.

Chapter 3

Monopole Antennas

This chapter focuses on the theoretical aspects of the design and analysis of the antenna applicator. First, the geometries of the three monopole antennas under study are described. Then, a model of the antennas in lossy media is presented in terms of the physical situation and the governing differential equation. The mathematical details required to calculate the reflection coefficient (return loss) and the heating patterns are also included in this chapter. In addition, the theory on insulated monopoles in dissipative medium proposed by King [42] is introduced as a preliminary analysis of the monopole antennas. It is used to predict the currents on the antennas, which will be useful for the interpretation of the numerical results of the magnetic field distributions discussed in Chapter 7.

3.1 Monopole Geometries Studied in this Thesis

The three monopole geometries under study are shown in Figure 3.1. The first geometry is the dielectric-tip monopole (DTM). This antenna is equivalent to the whip antenna imbedded in a teflon catheter used for hyperthermia. It is constructed by removing a length of the outer conductor at the distal end of a coaxial cable. The dielectric of the cable extends past the inner conductor to act as an insulator. Consequently, the DTM has no metallic parts at the tip in direct contact with the ambient medium.

Figure 3.1 also shows the open-tip monopole (OTM) geometry. This antenna is the same as the whip antenna. As the DTM, it is constructed by removing a length of the outer

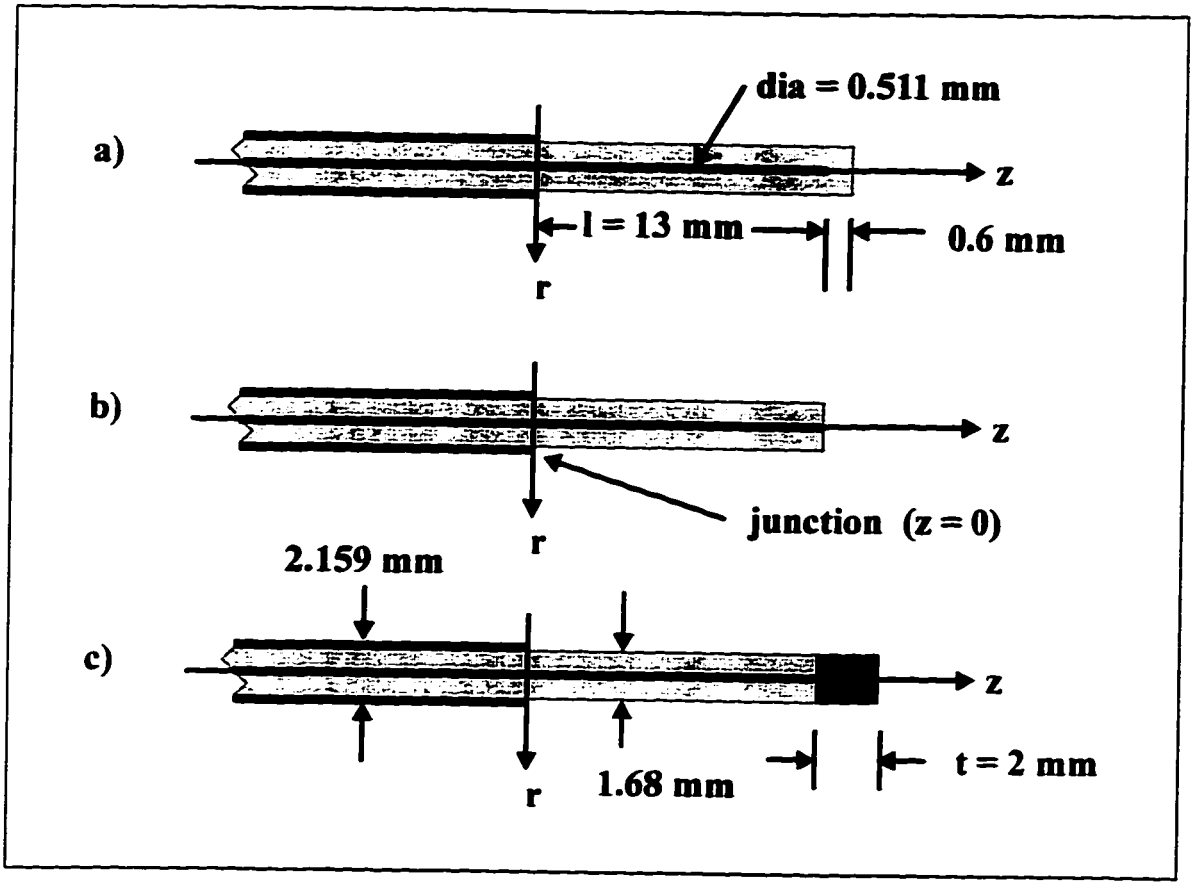

Figure 3.1: Monopole antennas: a) dielectric-tip monopole (DTM),b) open-tip monopole (OTM), and c) metal-tip monopole (MTM).

conductor of a coaxial cable. The inner conductor of the cable, covered by its dielectric is thus protruding with its tip in direct contact with the ambient medium.

The third illustration in Figure 3.1 is that of the metal-tip monopole (MTM). This one is constructed like the OTM but has a metal cap of diameter equal to the cable dielectric attached to the inner conductor. Similar antenna designs to the MTM were used in [49, 50] and it was found that the metal tip increases heating at the tip of the antenna. This geometry is also attractive because the metal tip can be used to record electrocardiograms.

The diameter of the monopoles was chosen to be the same as the diameter of a 50 Ω semi-rigid coaxial cable that was available for their construction. The length of the OTM was optimized in a previous study for minimum reflection coefficient at 2.45 GHz when the

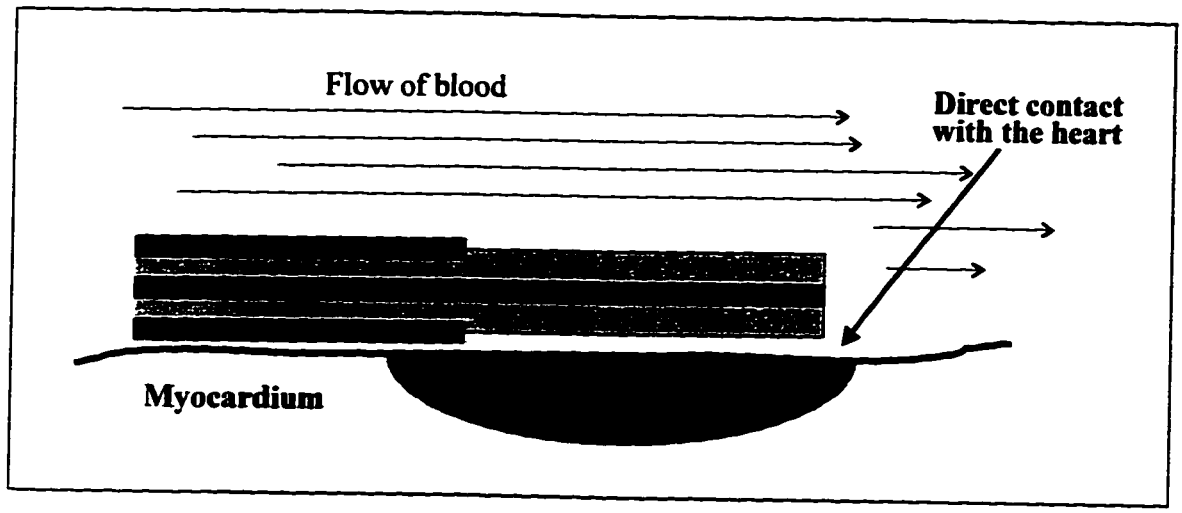

Figure 3.2: Illustration of the use of the monopole applicator.

antenna is in contact with myocardial tissue submerged in normal saline [51]. The antenna was found to be well matched at a length of 13 mm. This length provides a starting point for the length of the protruding inner conductor of the two other designs. The length of the protruding dielectric for the DTM and the metal tip for the MTM was chosen arbitrarily.

3.2 Physical Model

Monopole antennas radiate predominantly laterally. Accordingly, the catheter must be placed parallel to the endocardium in order to create a lesion (as illustrated in Figure 3.2). This contrasts with conventional RF ablation where the catheter touches the heart more or less at right angle to maximize the contact between the electrode surface and the region to ablate. However, a study demonstrates the feasibility and advantage of using catheters in lateral contact, especially for the treatment of ventricular tachycardias [43].

In reality, part of the antenna is in contact with the endocardium and part of the antenna is exposed to a blood flow. The size and shape of the actual lesion resulting in the endocardium are not only determined by the performance of the antenna from an electrical point of view, but also by heat loss due to thermal diffusion and thermoregulation (continual blood flow). The thermal aspects of the problem are very complex to model both numerically and experimentally. Futhermore. at this point in the research thermal aspect considerations

	Average Muscle [52]	Blood [52]	9 ppt Saline [53]
Temp [°C]	37	38	22
ϵ_r	47	55–56	74.7
σ [S/m]	2.14	2.5–3.1	2.75

Table 3.1: Dielectric constant and conductivity of average muscle, blood, and 9ppt saline at 2.45 GHz.

are not necessary to draw conclusions on the monopoles. For these reasons, the focus of this study is on the electrical aspect only and the reader should take note that the lesions presented in Chapter 7 do not accurately represent lesions created in a real life situation.

The electrical properties of the heart are not accurately known and vary considerably between individuals. In the range of uncertainty, they become similar to those of blood. For this reason, it is assumed that the antenna is entirely surrounded by a homogeneous material with properties comparable to those of blood. The material chosen is normal saline (a 9 ppt saline solution) at room temperature because of its properties and its availability for experimental measurements. The properties of average human muscle, blood, and 9 ppt saline are listed in Table 3.1.

The cooling effect that the flow of blood has on part of the monopole does not affect (from an electrical point of view) the electromagnetic radiation of the antenna on the side of interest. For this reason, the flow of blood is ignored and the ambient medium is assumed stable. Hence the problem reduces from a three-dimensional to a two-dimensional one. All of the assumptions discussed in this section are sufficient to characterize the behavior of the antennas in a medium similar to that of the heart.

3.3 Mathematical Model

An analysis of the electromagnetic fields generated by the antennas is required to determine their return loss and heating patterns. In this section, all the necessary theoretical formulations for the analysis are given. First, a description in mathematical terms of the electromagnetic (EM) fields propagating inside the feeding coaxial line and radiated by the

antenna is given. Then, the necessary mathematical equations for calculating the reflection coefficient and the heating patterns are derived in terms of the fields.

3.3.1 Field Equations

Since we will be working in the cylindrical coordinate system, the problem is illustrated with proper coordinate definitions in Figure 3.3.

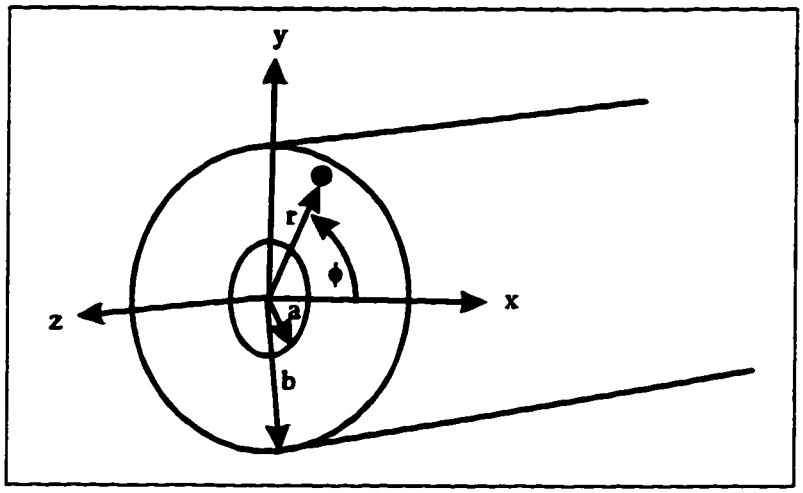

Figure 3.3: The feeding coaxial cable and monopole in cylindrical coordinates.

All EM fields are ruled by Maxwell's Equations [54]. For convenience, these equations are recalled below (in phasor form):

$$\nabla \times \vec{E} = -j\omega\vec{B} \tag{3.1}$$

$$\nabla \times \vec{H} = j\omega\vec{D} + \vec{J} \tag{3.2}$$

$$\nabla \cdot \vec{D} = \rho \tag{3.3}$$

$$\nabla \cdot \vec{B} = 0 \tag{3.4}$$

along with the constitutive relations for linear, isotropic materials: $\vec{D} = \epsilon\vec{E}$, $\vec{B} = \mu\vec{H}$, $\vec{J} = \sigma\vec{E}$.

The constitutive relations can be used to express (3.1) and (3.2) in terms of the electric (E) and magnetic (H) field only,

$$\nabla \times \vec{E} = -j\omega\mu\vec{H} \tag{3.5}$$

$$\nabla \times \vec{H} = j\omega\epsilon\vec{E} + \sigma\vec{E}. \tag{3.6}$$

If the curl is applied to the left and right side of (3.6), a lossy Helmholtz wave equation for the H field is obtained:

$$\begin{aligned} \nabla \times \nabla \times \vec{H} &= \nabla \times (j\omega\epsilon + \sigma)\vec{E} \\ &= (j\omega\epsilon + \sigma)\nabla \times \vec{E} \\ &= (j\omega\epsilon + \sigma)(-j\omega\mu\vec{H}) \\ \nabla^2\vec{H} + (j\omega\epsilon + \sigma)(j\omega\mu\vec{H}) &= 0. \end{aligned} \tag{3.7}$$

A coaxial cable can contain three types of propagation modes: transverse electromagnetic (TEM), transverse electric (TE), and transverse magnetic (TM). For a coaxial cable, the conditions $\beta b < 1$, and $\beta(b-a) < 1$, (where β is the propagation constant, a and b are the radius of the inner and outer conductor) will exclude the propagation of TE and TM modes respectively [55]. If the coaxial cable feeding a monopole is excited with a TEM mode and meets the above conditions, then only the TEM mode propagates inside the cable. Thus the only components of the fields inside the cable are H_ϕ and E_r. Moreover, if axial symmetry is maintained in the entire system (which is the case for the coaxial-fed monopoles), then TE modes are absent everywhere because they are nowhere generated. The TEM mode, which cannot propagate in lossy media, generates TM modes at the junction between the coaxial line and the antenna to maintain boundary conditions (the tangential E field and H field must be continuous across the boundary). The TM waves generated inside the cable decay vary rapidly since the TM modes are cut-off. And since only TM modes are propagated inside the media, the H field in the z direction is null everywhere. Furthermore, since the entire problem is axisymmetrical ($\frac{\partial}{\partial\phi} = 0$), the E_ϕ and H_r are null and the only field components remaining are H_ϕ, E_r, and E_z.

With these restrictions in mind, the first part of (3.7) can be expanded as:

$$\begin{aligned} \nabla \times \nabla \times \vec{H} &= \nabla \times \left[-\hat{r}\frac{\partial H_\phi}{\partial z} + \hat{z}\frac{1}{r}\frac{\partial(rH_\phi)}{\partial r}\right] \\ &= \hat{\phi}\frac{\partial}{\partial z}\left[-\frac{\partial H_\phi}{\partial z}\right] - \hat{\phi}\frac{\partial}{\partial r}\left[\frac{1}{r}\frac{\partial(rH_\phi)}{\partial r}\right] \end{aligned}$$

and (3.7) can be written as:

$$-\frac{\partial}{\partial z}\left[\frac{\partial H_\phi}{\partial z}\right]-\frac{\partial}{\partial r}\left[\frac{1}{r}\frac{\partial(rH_\phi)}{\partial r}\right]+(j\omega\epsilon+\sigma)(j\omega\mu H_\phi)=0. \tag{3.8}$$

This differential equation governs the model of the monopole antennas. Solving for the H field analytically would be quite tedious so the solution is found using numerical techniques. A numerical analysis will be the topic of the next chapter.

Once the H field is known, the components of the E field can be solved as follows. For

$$\begin{aligned}\vec{E} &= \frac{\nabla\times\vec{H}}{j\omega\epsilon+\sigma}\\ &= \frac{1}{j\omega\epsilon+\sigma}\left[-\hat{r}\frac{\partial H_\phi}{\partial z}+\hat{z}\frac{1}{r}\frac{\partial(rH_\phi)}{\partial r}\right]\end{aligned}$$

one sees that

$$\vec{E_r} = \frac{-1}{j\omega\epsilon+\sigma}\frac{\partial H_\phi}{\partial z} \tag{3.9}$$

$$\vec{E_z} = \frac{1}{r(j\omega\epsilon+\sigma)}\frac{\partial(rH_\phi)}{\partial r} \tag{3.10}$$

$$\vec{E_\phi} = 0. \tag{3.11}$$

3.3.2 Reflection Coefficient

If we consider the reflection coefficient at a reference plane in the cable far enough from its junction with the antenna, the TM waves generated by the junction have been attenuated and we can assume that only a TEM wave is propagating at this reference plane. Then, the reflection coefficient can be easily calculated from the known H field.

In general, the total H field anywhere inside the guide is a sum of the incident wave and the reflected wave with reference to the feed plane ($z=-l$) because that is where the incident wave is initiated:

$$H_\phi(z)=H_\phi^+e^{j\beta(z+l)}-H_\phi^-e^{-j\beta(z-l)}. \tag{3.12}$$

For a coaxial guide in the TEM mode (as is the case at the feed plane), the incident and reflected H fields are expressed in terms of the incident and reflected voltage.

$$H_\phi^+e^{j\beta(z+l)} = \frac{V_o^+e^{-j\beta(z+l)}}{r\eta\ln b/a} \tag{3.13}$$

$$H_\phi^-e^{-j\beta(z-l)} = \frac{V_o^-e^{+j\beta(z-l)}}{r\eta\ln b/a} \tag{3.14}$$

where η is the intrinsic impedance of the guide ($\eta = \sqrt{\frac{\mu}{\epsilon}}$), r is the radial distance, a and b are the radii of the inner and outer conductors respectively.

Using (3.13) and (3.14) in (3.12) we get:

$$H_\phi(z) r\eta \ln b/a = V_o^+ e^{-j\beta(z+l)} - V_0^- e^{j\beta(z-l)}. \tag{3.15}$$

The reflection coefficient, Γ, (or return loss) is defined as the ratio of the reflected voltage over the incident voltage ($\Gamma = \frac{V_o^-}{V_o^+}$). Thus (3.15) can be rewritten as:

$$\frac{H_\phi(z) r\eta \ln b/a}{V_o^+ e^{-j\beta(z+l)}} = 1 - \Gamma e^{j2\beta z}$$

or at the feed plane ($z = -l$),

$$\frac{H_\phi(-l) r\eta \ln b/a}{V_o^+} = 1 - \Gamma e^{-j2\beta l}$$

which can be rewritten as:

$$\Gamma = \left(1 - \frac{H_\phi(-l) r\eta \ln b/a}{V_o^+}\right) e^{j2\beta l}.$$

Finally, if we assume that the incident voltage at the feed plane has a magnitude of 1 V, then the reflection coefficient is expressed as:

$$\Gamma = (1 - H_\phi(-l) r\eta \ln b/a)\, e^{j2\beta l}. \tag{3.16}$$

3.3.3 SAR Patterns

The heating pattern of the monopoles is defined in terms of the Specific Absorption Rate (SAR). The SAR is a measure of the energy absorption per unit mass, in other words the amount of heat inside the tissue. It is calculated from the time-average dissipated power as follows,

$$SAR = \frac{1}{2}\sigma |\vec{E}|^2$$

For the monopoles,

$$SAR = \frac{1}{2}\sigma (|E_r|^2 + |E_z|^2) \quad [\mathrm{W/m^3}] \tag{3.17}$$

Before proceeding to the numerical analysis, it is good practice to have an idea of the outcome. In this manner, the programmer can effectively use the resources without over-modeling unimportant aspects of the problem or under-modeling the crucial aspects. For

this reason, King's theory on antennas in matter is introduced in the following section. It is used to obtain a crude approximation of the current distribution on the three monopoles.

3.4 King's Theory on Antennas in Matter

King [42] uses an analogy between transmission lines and insulated antennas in lossy media to derive the current distribution along the antenna. The analogy is that such antennas can be treated as a section of lossy transmission line with a generalized propagation constant that accounts for the ohmic losses in the conductors and the losses due to radiation from the antenna to the ambient medium. The analogy holds only under the following condition: $|k_3|^2 = |\omega^2\mu\,(\epsilon_3 - j\frac{\sigma_3}{\omega})| \gg |k_2|^2 = |\omega^2\mu\,(\epsilon_2 - j\frac{\sigma_2}{\omega})|$, where k_2 and k_3 are the propagation constant of the dielectric and the lossy ambient medium respectively.

For the monopoles under study in 9 ppt saline at 2.45 GHz, $|k_3|^2 \approx 4 \times 10^{10}$ rad/m which is much greater than $|k_2|^2 \approx 3 \times 10^7$ rad/m. Hence the analogy holds and the current in the conductor of the monopoles satisfies the wave equation for transmission lines;

$$\frac{d^2I(z)}{dz^2} + k_L^2 I(z) = 0$$

where k_L is the equivalent propagation constant that accounts for losses.

Equations for the solution of the current and the propagation constant are derived and given in [42]. What is most relevant here is that the current on the antenna is a standing wave which becomes the source for radiation and heating. The highest intensity of the current on the antenna will determine where the fields are the strongest and by extension, where heating inside the medium is most likely to occur.

From the transmission line analogy, the DTM may be regarded as a quarter-wavelength section of coaxial line terminated in an open-circuit. The standing wave of a transmission line terminated in an open-circuit has a current null at the open-circuit termination. Therefore, one can expect a current null at the end of the inner conductor of the antenna and a peak at the junction of the antenna and the cable (a quarter wavelength away). The OTM and MTM should behave more like loaded or short-circuited transmission lines because their center conductor is in contact with the lossy medium. The current on these antennas is expected

not to be null at the tip. Because of its larger metal surface, the MTM is expected to have maximum heating occurring at the tip. The magnitudes of the currents along open and short-circuited transmission lines are shown in Figure 3.4.

3.5 Conclusion

In this chapter, the antenna designs used in this research are presented. A model of the antennas immersed in matter is given and justified. Its material properties and governing differential equations are outlined. Finally, a crude theoretical treatment of the monopoles is presented in terms of the antenna currents. A numerical treatment of the model is the object of the following chapter.

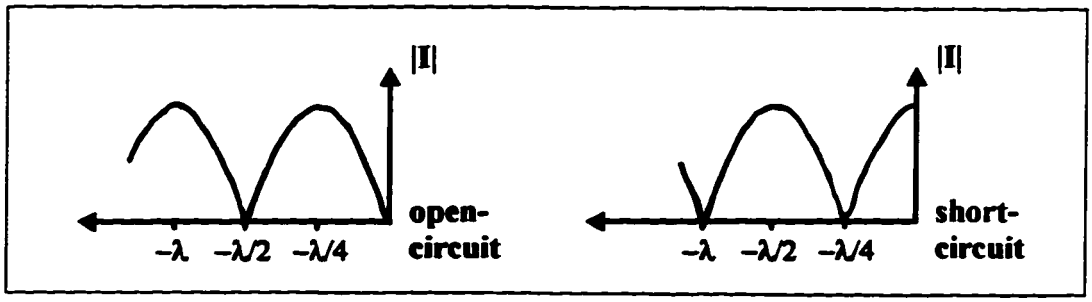

Figure 3.4: The magnitude of current along a) an open-circuited and b) a short-circuited transmission line [54].

Chapter 4

Numerical Treatment

Over the years, numerous numerical techniques have been developed to obtain approximate solutions to boundary-value problems. Three fundamental methods serve as the basis for all others. They are the Finite Differences Method, the Finite Element Method and the Method of Moments. Of the multitude of methods that have been derived therefrom, some are more adapted to certain types of problems. The method chosen for a specific task is determined by the complexity of the program, the amount of memory, and the running time required to get sufficiently precise results. The Finite Element Method is chosen for the analysis of the monopole applicator because of its ability to handle complex geometries as well as material inhomogeneities. The formulation used in this analysis is based on [56] which includes higher-order modes both in the coaxial line feeding the monopole and in the surrounding medium where radiation occurs. This approach is more versatile than the one adopted in [49] which is limited to short antennas.

In this chapter, a brief review of the Finite Element Method is given followed by its application to the monopole antenna model. A description of the computer programs used for the numerical analysis is given in Section 4.3, followed by a validation of these programs in Section 4.4.

4.1 Finite Element Method (FEM)

The Finite Element Method consists of fragmenting a complex problem into elementary problems by dividing the domain under study into subdomains called *finite elements*. The unknown function that describes the original domain is approximated by a combination of independent linear (interpolation) functions that describe each element in such a way that the unknown quantity is continuous across the boundaries of adjacent elements. The nature of the solution and the degree of approximation depend on the size and number of subdomains as well as the chosen interpolation functions. Good references on FEM applied to electromagnetic problems can be found in: [57, 58, 59, 60, 61].

The main advantages of the FEM are reviewed below.

- There are many degrees of freedom while dividing the domain of the problem in subdomains: the position and number of nodes, and therefore the number, shape, and layout of the elements.
- Problems containing different materials can be easily modeled by specifying the material properties for each element.
- A domain of any shape and size, simple or complex, can be discretized into elements.
- A nonuniform mesh of various element size (See Figure 4.1.) does not pose a problem when using the Finite Element Method. This is especially convenient when a structure requires finer meshing in certain areas where the functions varies rapidly, while a more crude mesh is sufficient in others where there is little variation in the function.
- Nodes can be chosen in specific points where knowledge of the function is required.
- Boundary conditions that are expressed in terms of the gradient of the function (Neumann or Cauchy boundary conditions) are easily taken into account.

The main disadvantage of the FEM is that the programming involved is longer and more complex than for other numerical methods. FEM programs are usually written only to solve a group of problems of similar type but with conditions that may vary substantially.

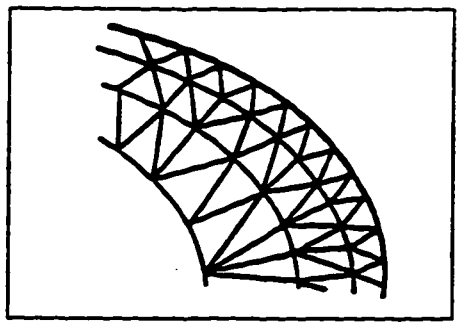

Figure 4.1: Example of a nonuniform mesh.

Before applying the FEM to the monopole-myocardium problem, a brief review of the method is presented. The formulation of the FEM used in the following analysis utilizes the Galerkin Method. This method is used to approximate the solution of a boundary-value problem. For this reason, the definition of boundary-value problems is recalled next.

4.1.1 Boundary-value problems

Boundary-value problems arise in the mathematical modeling of physical systems. A typical boundary-value problem can be defined by a governing differential equation in a domain, Ω.

$$L\chi = f \tag{4.1}$$

together with the boundary conditions on the boundary, Γ, that encloses the domain. In (4.1) L is a differential operator; f, the excitation or forcing function; and χ, the unknown quantity. It is desirable to solve these problems analytically. Unfortunately, analytical solutions are only possible in few cases. Generally, approximation methods must be used. The most widely used ones are the Ritz Method and the Galerkin Method. The latter is the one of interest in this work and will consequently be summarized below.

4.1.2 Galerkin Method

The Galerkin Method is part of the family of weighted residual methods. The solution is sought by weighting the residual of the differential equation. For example, let $\tilde{\chi}$ be the approximate solution of (4.1). The substitution of this approximation in the original equation

yields a residual,

$$r = L\tilde{\chi} - f \neq 0. \tag{4.2}$$

The best approximation of χ is the one that reduces the residual, r, to the least value at all points in Ω. The weighted residual methods enforce the condition:

$$R_i = \int_\Omega w_i r \, d\Omega = 0 \tag{4.3}$$

where R_i is the weighted residual integral and w_i is the chosen weighting function. In the Galerkin method, w_i is usually chosen to be the same as the trial function that approximates χ. This usually leads to the most accurate solution.

4.1.3 FEM Using the Galerkin Method

In many boundary-value problems, it can be very difficult if not impossible to find a trial function defined over the entire solution domain which is capable of representing the true solution of the problem. To alleviate this difficulty, the solution domain is divided into many small subdomains. Each subdomain represents a small portion of the entire solution domain which can be more easily approximated by a simple trial function. Thus the entire solution domain is represented by a combination of trial functions. These trial functions are chosen as simple interpolation functions (N_j), having unknown coefficients (u_j).

The FEM analysis of a boundary-value problem comprises four steps. In the first step, the domain is discretized in small elements which are usually chosen as triangles or squares. The second step is to select an interpolation function that provides an approximation of the unknown solution within an element. Normally, first, second, or higher order polynomials are chosen. Higher order polynomials will yield a better approximation but the higher the order, the more complex the formulation will be. The approximate solution in an element, e, can be expressed in terms of the real solution as:

$$\tilde{\chi^e} = \sum_{j=1}^{n} N_j^e \chi_j^e = \{N^e\}^T \{\chi^e\} \tag{4.4}$$

where the superscript, e, indicates an element ID, and n is the number of nodes within the element.

In the third step, the formulation of the system of equation is established using the Galerkin and the weighted residual as follows (the weighting functions used are the same as the interpolation functions):

$$R_i^e = \int_{\Omega^e} N_i^e (L\tilde{\chi^e} - f)\, d\Omega \qquad i = 1, 2, 3, ...n. \tag{4.5}$$

Substituting (4.4) in (4.5) yields:

$$R_i^e = \int_{\Omega^e} N_i^e L\{N^e\}^T\{\chi^e\}\, d\Omega - \int_{\Omega^e} f N_i^e\, d\Omega \qquad i = 1, 2, 3, ...n \tag{4.6}$$

or in matrix form:

$$\{R^e\} = [K^e]\{\chi^e\} - \{b^e\} \tag{4.7}$$

where

$$K_{ij}^e = \int_{\Omega^e} N_i^e L N_j^e\, d\Omega$$

$$b_i^e = \int_{\Omega^e} f N_i^e\, \Omega.$$

The final step is to apply the boundary conditions and to solve the final system of equations which has the following form:

$$[K]\{\chi\} = \{b\}. \tag{4.8}$$

Once the system is solved for $\{\chi\}$, post-processing can be done to calculate the parameters of interest.

4.2 Formulation of the Monopole-Myocardium Problem Domain

We saw in chapter 3 that for an axisymmetrical problem with propagation in the TEM mode only, Maxwell's Equations can be manipulated to obtain:

$$-\frac{\partial}{\partial z}\left[\frac{\partial H_\phi}{\partial z}\right] - \frac{\partial}{\partial r}\left[\frac{1}{r}\frac{\partial (rH_\phi)}{\partial r}\right] + (j\omega\mu H_\phi)(\sigma + j\omega\epsilon) = 0. \tag{4.9}$$

Equation (4.9) represents the governing differential equation, (4.1), that will be solved over the domain of interest using the FEM. The unknown quantity is the magnetic field ($\chi = H_\phi$) and in this case, the forcing function is null ($f = 0$).

The domain of interest is illustrated in Figure 4.2. Because of axisymmetry, only half the problem is considered which greatly reduces the size of the problem. In free space the radiation of an antenna is not bounded, but to apply the FEM, a spherical radiation boundary must be enforced. The location of the boundary is not critical because the radiated fields for an insulated monopole antenna surrounded by a lossy medium dissipate rapidly. Experiments in saline show that below 5 GHz, the results do not depend on the boundary location when it is at $r \geq 40$ mm. As for the feed boundary of the coaxial cable, it is chosen at $z = -29$ mm to ensure that higher-order modes reflected by the antenna junction have decayed to insignificant magnitudes [62]. The surrounding medium is assumed to be normal saline at room temperature ($\epsilon_r = 75$ $\sigma = 2.80$ S/m), as explained in Chapter 3. The dielectric of the coaxial cable is chosen in accordance with the coaxial cable that will be used later in the experimentation ($\epsilon_r = 2.038$).

Now that the boundary-value problem has been defined in terms of the governing differential equation and the domain, the Galerkin FEM is applied step by step.

4.2.1 First Step: Discretization of the Domain

The domain is discretized using first order triangular elements. Each element is chosen so as to contain homogeneous material. The conductors are assumed to be perfectly conducting and hence, are subtracted from the geometry by replacing them with electric walls. A very dense mesh is used at the interface between the antenna and its surrounding medium where the field varies rapidly. The size of the elements gradually increases with the distance from the surface of the antenna. An example of a mesh is shown in Figure 4.3. It was created using ARIES[1], a commercial automatic mesh generating program. Convergence tests have revealed that roughly 10 000 triangular elements are needed to provide an acceptable solution.

4.2.2 Second Step: Selection of interpolation functions

Over each finite element, e, H_ϕ is approximated by:

$$H_\phi^e \approx \sum_{j=1}^{n} u_j N_j^e = \tilde{H}_\phi^e \tag{4.10}$$

[1]MSC/ARIES is a trademark of The MacNeal-Schwendler Corporation, Milwaukee, Wisconsin, USA.

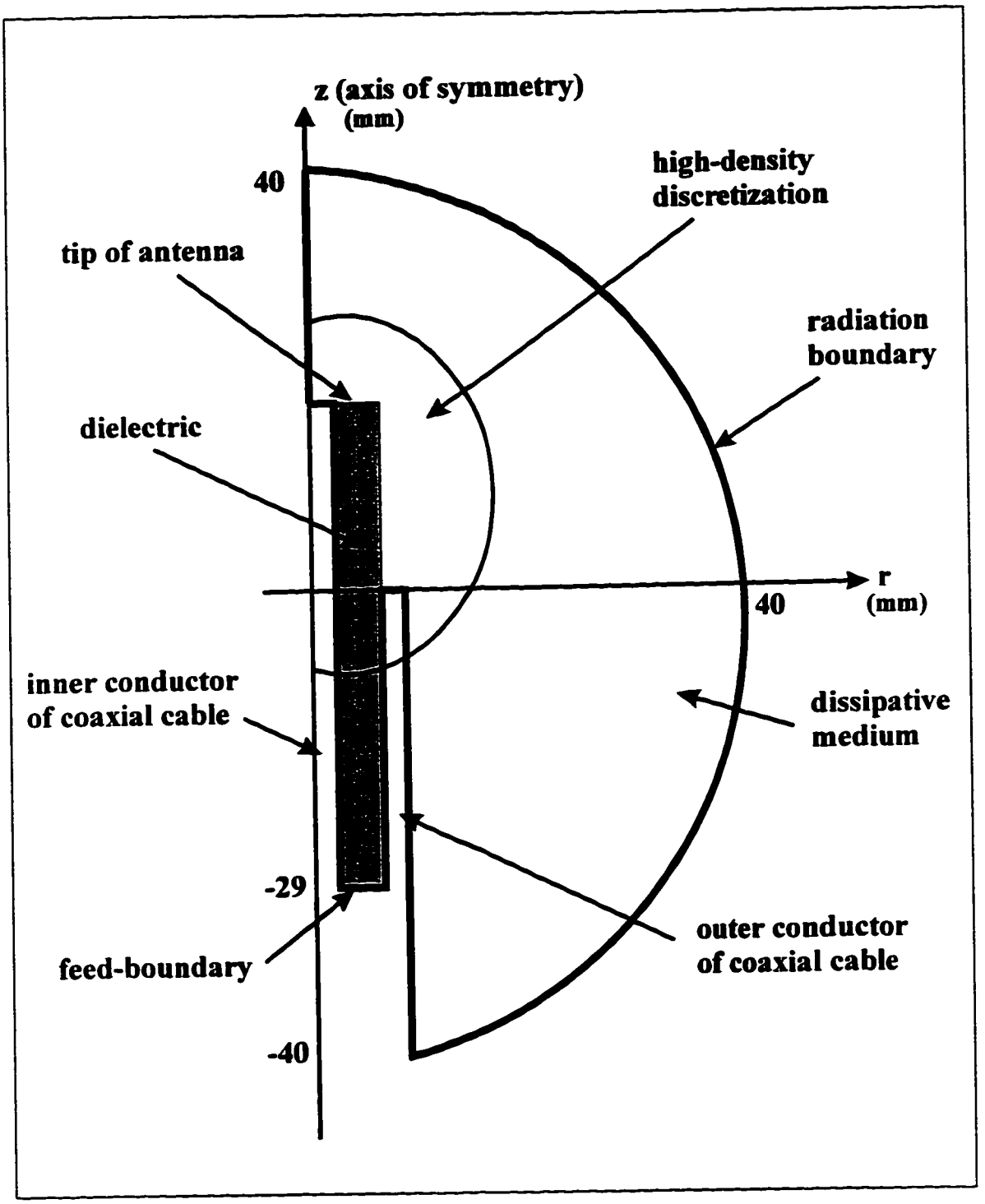

Figure 4.2: FEM Solution Domain for the OTM configuration.

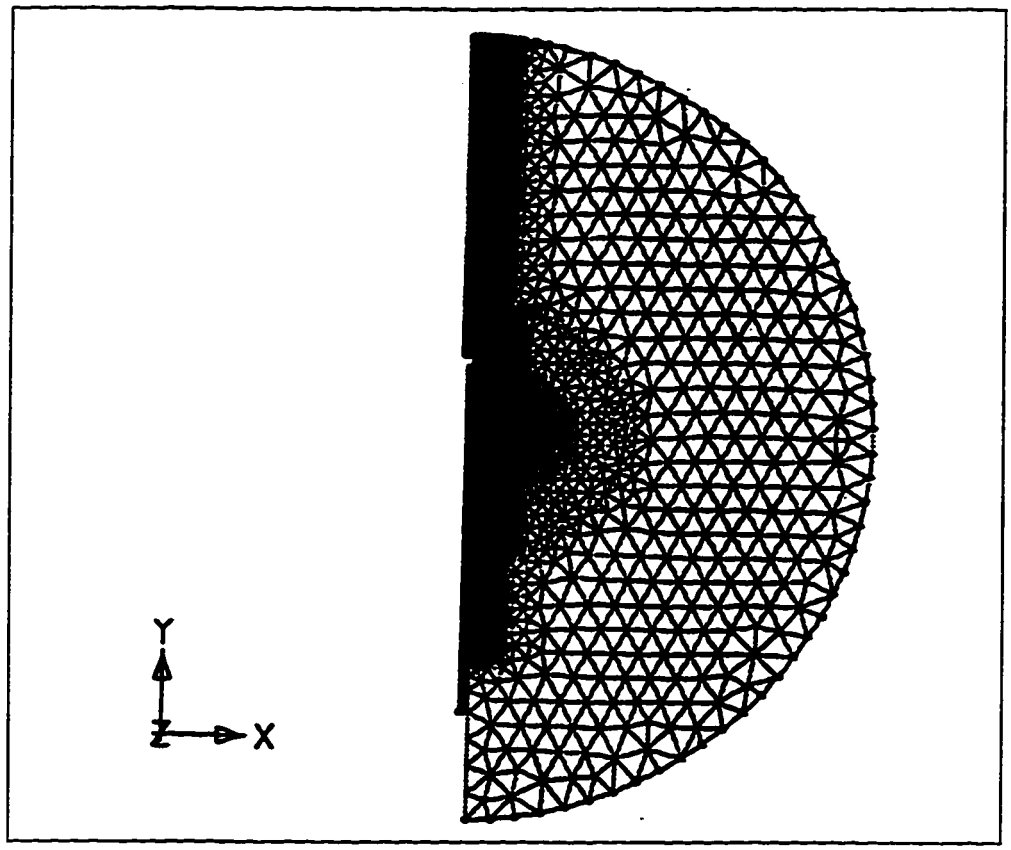

Figure 4.3: Mesh of the domain for a MTM configuration.

where the u_j's are unknown complex constants, N_j's are real-valued FEM interpolation functions, and n is the number of nodes defining the e^{th} element (which is 3 for first order triangles). The interpolation functions (functions of the space coordinates, r and z) for linear, first order approximation can be written as:

$$\begin{bmatrix} N_1 \\ N_2 \\ N_3 \end{bmatrix} = \frac{1}{2A} \begin{bmatrix} r_2 z_3 - r_3 z_2 & z_2 - z_3 & r_3 - r_2 \\ r_3 z_1 - r_1 z_3 & z_3 - z_1 & r_1 - r_3 \\ r_1 z_2 - r_2 z_1 & z_1 - z_2 & r_2 - r_1 \end{bmatrix} \begin{bmatrix} 1 \\ r \\ z \end{bmatrix} \tag{4.11}$$

where A is the area of the element.

4.2.3 Third Step: Application of the Galerkin Method

The development in this section follows the one given in [63].

First, a simplification of the number of variables in (4.9) is made. Let $Y = (\sigma + j\omega\epsilon)^{-1}$

and $Z = j\omega\mu$. Then the equation becomes,

$$-Y\frac{\partial}{\partial z}\left[\frac{\partial H_\phi}{\partial z}\right] - Y\frac{\partial}{\partial r}\left[\frac{1}{r}\frac{\partial (rH_\phi)}{\partial r}\right] + ZH_\phi = 0. \tag{4.12}$$

The application of the Galerkin method, using $\tilde{\chi}^e = \tilde{H}^e_\phi$ and $f = 0$ in (4.5), yields the following weighted residual integral:

$$R_i = \int\int_e N^e_i \left\{-Y\frac{\partial}{\partial r}\left(\frac{1}{r}\frac{\partial (r\tilde{H}^e_\phi)}{\partial r}\right) - Y\frac{\partial}{\partial z}\left(\frac{\partial \tilde{H}^e_\phi}{\partial z}\right) + Z\tilde{H}^e_\phi\right\} dr dz = 0$$
$$i = 1, 2, 3, \ldots n. \tag{4.13}$$

Applying the product rule,

$$u\frac{dv}{dx} = \frac{d(uv)}{dx} - v\frac{du}{dx},$$

to the first term of the integral:

$$u = YN^e_i; \qquad \frac{dv}{dx} = \frac{\partial}{\partial r}\left(\frac{1}{r}\frac{\partial (r\tilde{H}^e_\phi)}{\partial r}\right),$$

and to the second term:

$$u = YN^e_i; \qquad \frac{dv}{dx} = \frac{\partial}{\partial z}\left(\frac{\partial \tilde{H}^e_\phi}{\partial z}\right),$$

equation (4.13) can be written as:

$$-\int\int_e \left[\frac{\partial}{\partial r}\left(\frac{YN^e_i}{r}\frac{\partial (r\tilde{H}^e_\phi)}{\partial r}\right) + Y\frac{\partial}{\partial z}\left(N^e_i\frac{\partial H^e_\phi}{\partial z}\right)\right] dr dz$$
$$+\int\int_e \left[\frac{Y}{r}\frac{\partial (rH^e_\phi)}{\partial r}\frac{\partial N^e_i}{\partial r} + Y\frac{\partial H^e_\phi}{\partial z}\frac{\partial N^e_i}{\partial z} + ZH^e_\phi N^e_i\right] dr dz = 0. \tag{4.14}$$

The first double integral of the equation can be simplified to a contour integral by considering the divergence theorem in two dimensions,

$$\int\int_S \nabla \cdot \vec{F}\, ds = \oint_C \vec{F} \cdot \hat{n}\, dl \tag{4.15}$$

where $\vec{F}$ is a vector defined over the surface S, $\hat{n}$ is an outward unit vector normal to the boundary, C, enclosing S as shown in Figure 4.4. If $\vec{F} = P\hat{a_x} + Q\hat{a_y}$ (4.15) becomes

$$\int\int_S \left(\frac{\partial P}{\partial x} + \frac{\partial Q}{\partial y}\right) dx\, dy = \oint_C (P\hat{a_x} \cdot \hat{n} + Q\hat{a_y} \cdot \hat{n})\, dl. \tag{4.16}$$

With $\hat{a_x} \cdot \hat{n} = \cos\alpha$ and $\hat{a_y} \cdot \hat{n} = \cos\beta$, the direction cosines of the outward vector normal to

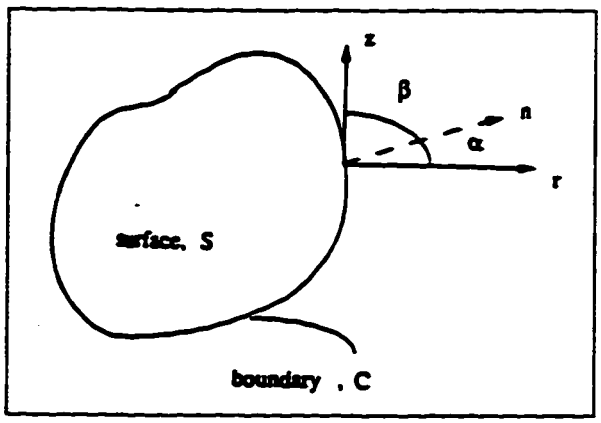

Figure 4.4: Illustration of the outward unit vector and its direction cosines for the divergence theorem.

the boundary, (4.16) can be written as:

$$\int\int_S \left(\frac{\partial P}{\partial x} + \frac{\partial Q}{\partial y}\right) dx\, dy = \oint_C (P\cos\alpha + Q\cos\beta)\, dl \tag{4.17}$$

The application of (4.17) to the first double integral of (4.14), transforms it into a contour integral along the boudary in a counter clockwise direction:

$$-Y \oint_e \left[\frac{1}{r}\frac{\partial(rH_\phi^e)}{\partial r} N_i^e \cos\alpha^e + \frac{\partial H_\phi^e}{\partial z} N_i^e \cos\beta^e\right] dl. \tag{4.18}$$

This last expression can be expressed in terms of the tangential electric field simply by considering Maxwell's equation for the curl of $\vec{H}$.

$$\nabla \times \vec{H} = (\sigma + j\omega\epsilon)\vec{E}$$

Knowing that $\vec{H} = H_\phi \hat{a_\phi}$ and $\vec{E} = E_r \hat{a_r} + E_z \hat{a_z}$, the equation can be rewritten as

$$-\frac{\partial H_\phi}{\partial z}\hat{a_r} + \frac{1}{r}\frac{\partial(rH_\phi)}{\partial r}\hat{a_z} = Y^{-1}(E_r\hat{a_r} + E_z\hat{a_z}) \tag{4.19}$$

and the following identities can be easily derived:

$$\begin{aligned} E_r \approx -Y\frac{\partial \tilde{H}_\phi}{\partial z} &= \tilde{E}_r \\ E_z \approx \frac{Y}{r}\frac{\partial(r\tilde{H}_\phi)}{\partial r} &= \tilde{E}_z \end{aligned} \tag{4.20}$$

Substituting (4.20) in (4.18) gives

$$-\oint \left[\tilde{E}_z^e N_i^e \cos\alpha^e - \tilde{E}_r^e N_i^e \cos\beta^e\right] dl = -\oint \tilde{E}_{tan} N_i^e \, dl \tag{4.21}$$

and equation (4.14) can be expressed as

$$\int\int_e \left[\frac{Y}{r}\frac{\partial(r\tilde{H}_\phi^e)}{\partial r}\frac{\partial N_i^e}{\partial r} + Y\frac{\partial \tilde{H}_\phi^e}{\partial z}\frac{\partial N_i^e}{\partial z} + Z\tilde{H}_\phi^e N_i^e\right] dr\,dz = \oint \tilde{E}_{tan} N_i^e \, dl$$
$$i = 1, 2, 3, ...n. \tag{4.22}$$

Substituting (4.10) in (4.22) yields,

$$\sum_{j=1}^{n} u_j \int\int_e \left[Y\frac{\partial N_i}{\partial r}\frac{\partial N_j}{\partial r} + Y\frac{\partial N_i}{\partial z}\frac{\partial N_j}{\partial z} + \frac{Y}{r}\frac{\partial N_i}{\partial r}N_j + ZN_iN_j\right] dr\,dz$$
$$= \oint \tilde{E}_{tan} N_i \, dl \quad i = 1, 2, 3, ...n \tag{4.23}$$

Equation (4.23) constitutes the discretization of (4.12) for one element within the problem domain. When evaluated, the result is a subsystem of n linear algebraic equations. This system is to be solved for the unknown coefficients u_j's which reflect the values of $\tilde{H}_\phi$ at the n nodes of the element. All individual element subsystems forming the problem domain are assembled into a final system of linear algebraic equations to be solved subject to the boundary conditions.

4.2.4 Fourth Step: Boundary Conditions

The boundary conditions of the problem are imposed on the final system of equations as follows:

- Along the z-axis (Fig. 4.2), $H_\phi = 0$ because of symmetry. This permits complete elimination of the unknowns associated with nodes falling on the axis of symmetry, thereby reducing the order of the matrix equation.
- On the innner and outer conductors of the coaxial cable which are assumed perfectly conducting, the tangential E field is zero. Accordingly, nodes on those boundaries have no contribution on the right-hand side vector of (4.23).

- A TEM radiation condition is enforced on the outer spherical boundary [64]. EM fields can be assumed to be plane waves at far field thus at all nodes on the radiation boundary, $E_{tan} = \eta H_\phi$ with $\eta = \sqrt{\frac{j\omega\mu}{\sigma+j\omega\epsilon}}$.

- A pure TEM mode is assumed in the coaxial cable at a point sufficiently far from the cable-antenna junction. Generally, the total magnetic field (H_ϕ) is the difference between the incident wave (H_ϕ^+) and the reflected wave (H_ϕ^-). At the feed plane ($z = -29$), the FEM formulation must allow for the application of a known incident wave, and simultaneously present a reflectionless termination for the unknown reflected wave. This is made possible by expressing H_ϕ^- as $(H_\phi^+ - H_\phi)$ and by writing a Neumann boundary condition for H_ϕ as follows:

$$\begin{aligned} H_\phi &= |H_\phi^+|e^{-jkz} - |H_\phi^-|e^{jkz} \\ \frac{\partial H_\phi}{\partial z} &= -jk|H_\phi^+|e^{-jkz} - jk|H_\phi^-|e^{jkz} \\ \frac{\partial H_\phi}{\partial z} &= -jk(H_\phi^+ + H_\phi^-) \\ \frac{\partial H_\phi}{\partial z} &= -jk(H_\phi^+ + H_\phi^+ - H_\phi) \\ \frac{\partial H_\phi}{\partial z} &= -jk(2H_\phi^+ - H_\phi). \end{aligned} \tag{4.24}$$

  where k is the propagation constant in the coaxial cable. Equation (4.24) is used in (4.18) to specify the excitation at the feed plane.

More details about the boundary conditions for the FEM formulation can be found in [56, 63].

The solution of the final system of equations as well as the post-processing is automated. A description of the programs used is given in the following section.

4.3 Description of the Programs

The sequential use of the computer programs is the following:

1. CONVERSION: This program converts the mesh created by ARIES[2] to three input files needed for the FEM program.

[2]MSC/ARIES is a trademark of The MacNeal-Schwendler Corporation. Milwaukee. Wisconsin, USA.

2. FDFEM: This is the FEM program. It generates the value of H_ϕ at every node of the mesh. It can also compute the reflection coefficient.

3. FEMGRID: This program is used for post-processing of the FEM program. It creates a uniform rectangular grid from the irregular triangular mesh used in FDFEM. It also determines H_ϕ at all points of the grid from the known H_ϕ at all nodes of the mesh.

4. FDGRID: This program applies the Finite Differences Method to the data obtained by FEMGRID to calculate the E field. Once the E field is known, the program easily computes the SAR at all points of the grid.

These programs are briefly described in the following sections to highlight their basic concepts. They were written in FORTRAN language.

4.3.1 FDFEM

FDFEM is a program that evaluates the system of equations developed in the previous section. It solves for the H_ϕ field, from which all other parameters of interest can be calculated. FDFEM is a modification of SUMBAR, a program for axisymmetrical radiation problems implemented by H.O. Ali, which is readily available at the University of Ottawa [63]. The modifications include sparse matrix algorithms, user defined filenames and a more flexible input boundary condition file format.

The sparse matrix algorithms are implemented to reduce computation time and memory usage. They are taken from [65, 66]. Although the routines are given in C code, they are easily interfaced to a FORTRAN program through routines given by the author.

The mesh of the problem is obtained as described in Section 4.2.1. The relative data of the mesh is exported and converted into a format that can be read by the FDFEM program. Three input files are used to describe the FEM mesh: a node file, a triangle file and a boundary condition file. The node file simply gives the (r,z) position of each node. The triangle file gives the identification number of the three nodes associated to each element (first order triangular elements). The boundary condition file provides the node IDs, triangle IDs and material IDs. These in turn specify the boundary or intersection on which a specific node or triangle lies, and the material properties of the given element. An option exists for

the boundary condition files to specify that ϵ and σ of equation (4.9) should be calculated at each frequency. In such a case, the user must specify the salinity and temperature. The program will then use the Cole-Cole equations [67, 53] to calculate the frequency dependent parameters.

The node IDs for possible node types are listed below:

1 nodes on the radiation boundary
2 homogeneous Dirichlet nodes (on axis of symmetry)
3 inhomogeneous Neumann nodes (on feed plane)
4 nodes at the intersection of the feed plane and a conductor
5 nodes at the intersection of the radiation boundary and the axis of symmetry
6 nodes at the intersection of a conductor and the axis of symmetry
7 nodes at the intersection of the radiation boundary and a conductor
0 all other nodes.

The triangle IDs for the possible element types are listed below:

1 elements with an edge on the radiation boundary
2 elements with an edge on the feed plane
0 all other elements.

The user may choose between the following output file formats: reflection coefficient versus frequency or H field node values in polar or rectangular form. The reflection coefficient is calculated using the expression developed in Chapter 3 with the following assumptions: the feed plane is located at $z = -l$ and the incident voltage at that point is 1 V.

4.3.2 FEMGRID

FEMGRID is used for the post processing of the results obtained from the FEM program. It generates a uniform rectangular grid over a given region of the mesh used in FDFEM. Three input files are required to run the program: a node file, an element file and a H-field file. The node and element file contain the same information as those used with the FDFEM program. The H-field file must contain the H_ϕ value in rectangular form at each node (this file can be obtained from FDFEM). For a user defined grid size, the program builds a new grid and calculates the value of the field at each new grid point. The triangle that contains a new grid point is located and the same previous interpolation functions, (4.11), are used to

extrapolate the corresponding H_ϕ value.

4.3.3 FDGRID

This program uses the output generated by FEMGRID in order to compute the E field on the uniform grid using the Finite Differences Method. In essence, the derivative of H_ϕ with respect to r and z are approximated to evaluate the E field. From the curl of H, the following expressions are found:

$$\begin{aligned} E_r &= -\frac{1}{\sigma + j\omega\epsilon}\frac{\partial H_\phi}{\partial z} \\ E_z &= \frac{1}{\sigma + j\omega\epsilon}\frac{1}{r}\frac{\partial (rH_\phi)}{\partial r}. \end{aligned}$$

E_z has a singularity at $r = 0$. This is easily rectified by applying l'Hospital's rule:

$$\begin{aligned} \lim_{r\to 0}\frac{1}{r}\frac{\partial (rH_\phi)}{\partial r} &= \lim_{r\to 0}\left(\frac{H_\phi}{r} + \frac{\partial H_\phi}{\partial r}\right) \\ &= \lim_{r\to 0}\left(\frac{\partial H_\phi}{\partial r} + \frac{\partial H_\phi}{\partial r}\right) \\ &= 2\lim_{r\to 0}\frac{\partial H_\phi}{\partial r}. \end{aligned}$$

The heat density (SAR) is of interest solely in lossy medium surrounding antenna. Consequently, the E field is only calculated outside the antenna, thus simplifying the program. Central differences are used to calculate the derivatives everywhere except at the border of the grid. In those instances, forward and backward differences are used. The approximate formulas were taken from Kreyszig [68] and use three points:

$$\begin{aligned} \text{Forward differences:} \quad & f'_{(j,i)} \approx \frac{1}{2h}(-3f_{(j,i)} + 4f_{(j+1,i)} - f_{(j+2,i)}) \\ \text{Central differences:} \quad & f'_{(j,i)} \approx \frac{1}{2h}(-f_{(j-1,i)} + f_{(j+1,i)}) \\ \text{Backward differences:} \quad & f'_{(j,i)} \approx \frac{1}{2h}(f_{(j-2,i)} - 4f_{(j-1,i)} + 3f_{(j,i)}) \end{aligned}$$

A derivation of these equations is given in [68].

4.4 Validation

A preliminary verification of the computer programs is made using simple problems having analytical solutions. Two such problems are the short-circuited and impedance matched

transmission line. The reflection coefficient and magnetic field values obtained from the numerical model for these two problems are compared to their analytical solutions.

The transmission line is chosen as a section of coaxial cable 29 mm long having an inner conductor of 0.255 mm radius, an outer conductor of 0.838 mm inner radius, and a dielectric of 2.038 relative permittivity. The cable is assumed to be lossless.

A short-circuited transmission line has, in theory, a reflection coefficient of unit magnitude. Simulations over a frequency range of 1–4 GHz, give a magnitude of 1–0.993 which is within 1% of the analytical value. As shown in Section 3.4, Figure 3.4, the short-circuited transmission line exhibits a standing wave caused by the reflection. The current wave along the inner conductor has a maximum at the load and a minimum occuring a quarter-wavelength away. The magnetic field obtained from a simulation at 2.45 GHz (see Figure 4.5) clearly demonstrates this standing wave with a maximum at the load ($z = 0$ mm) and a minimum approximately a quarter-wavelength away ($z = 21.4$ mm).

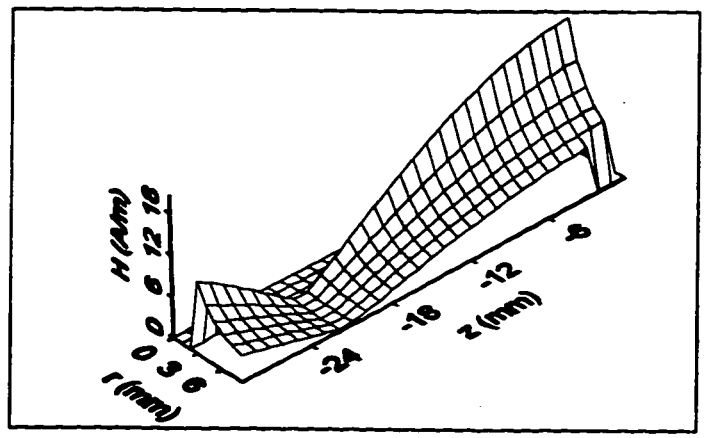

Figure 4.5: Magnitude of the magnetic field along a section of a short-circuited coaxial line.

The reflection coefficient for a transmission line terminated in a matched load is theoretically zero since all power is transmitted to the load. From simulations over 1–4 GHz, the numerically calculated reflection coefficient ranges from 0.00360–0.00369 which is very close to zero. The magnitude of the magnetic field obtained from a simulation at 2.45 GHz is compared to the analytical values in Table 4.1. The numerical calculations are well within 1% of the analytical values.

Although the results given in this section are very close to the analytical solutions, the monopole problem is much more complex then the examples presented here. For this reason, it is important to confirm the numerical results of the monopole simulations with experimental measurements. Experimental measurements can truly validate the numerical treatment of the model.

4.5 Conclusion

In this chapter we focused on the numerical treatment of the model required to calculate the field intensity in and around the antenna. Let us remember that the goal is to compare the antennas in terms of their reflection coefficient and SAR patterns. Knowledge of the fields enables us to compute these quantities.

The numerical analysis begins with a review and application of the Galerkin Finite Element Method to the monopole model. A system of equations is created. It describes the behavior of the magnetic field in the problem domain. The computer programs used to solve the FEM system and for post-processing of the results are described and validated. A validation establishes confidence in the results. Nevertheless, the programs are restricted by unavoidable approximations. Therefore, the results obtained from the numerical model for the monopole antennas are confirmed with experimental measurements performed on several prototypes of the antennas. These measurements are the object of the next chapter.

Radial Distance, r (mm)	Analytical Value (A/m)	Numerical Calculation (A/m)	Error (%)
0.314	10.14	10.2	0.6
0.419	7.60	7.64	0.5
0.525	6.07	6.09	0.3
0.629	5.06	5.06	0.0
0.733	4.35	4.33	0.5
0.838	3.80	3.80	0.0

Table 4.1: Comparison of the magnitude of the magnetic field at various radial distances.

Chapter 5

Experimental Measurements

To establish good confidence in the numerical model, it is necessary to conduct experimental measurements. These measurements allow a confirmation of the numerical results. However, they must also be reliable. The experiments performed must be well established so that they can be reproduced. Every component used must be accurately characterized and the measurements must be made several times to ensure repeatability.

The details of the experiments and methodology used to measure the reflection coefficient and the temperature profiles of the antennas are discussed in the first and second parts of this chapter respectively.

5.1 Return Loss Measurements

This section describes the procedure for building the various monopole configurations, preparing the saline solution, and measuring the reflection coefficient.

5.1.1 Equipment

The list of equipment used to construct the monopoles and for the reflection coefficient measurements are listed below:

- 50 Ω Semi-rigid Coaxial Cable (OD: 2.519 mm, Teflon Dielectric: $\epsilon_r = 2.038$)
- Copper Tube (Diameter: 0.0625 mm)

- 900 ml Distilled Water
- 8 gr NaCl
- Autobalance Universal Bridge, Wayne Kerr model B642
- Conductivity Probe, Yellow Springs Instruments model 3403 s/n 3405
- Mercury Thermometer
- Network Analyzer, Hewlett Packard model HP 8510B
- SMA Calibration Kit, Hewlett Packard

5.1.2 Prototype Construction

To build the prototypes, a section of coaxial cable about 20 cm long is taken. An SMA connector is attached to one end of the cable. At the other end, the outer conductor is stripped by an appropriate length, l. The OTM does not require any additional handling. The DTM is fabricated by retracting the inner conductor by a few millimeters. This leaves the dielectric insulator protruding at the tip with a small hole left by the absence of the inner conductor. The hole is filled with Vaseline which has the same properties as teflon ($\epsilon_r \approx 2.1$) at 2.45 GHz [71].

For the MTM, the dielectric is stripped from the tip of the inner conductor for a length, t. The same length is taken from copper tubing and the piece is soldered on the extending inner conductor thus creating a metal tip.

All three monopoles of Figure 3.1 were constructed but it was deemed unnecessary to build all the configurations of the MTM simulated for its optimization. Based on the simulation results, the $l = 6.5$, $t = 4$ mm and $l = 13$, $t = 2$ mm were chosen because they have the best match and the most uniform SAR pattern respectively. To compare various lengths, l, for the same length $t = 4$ mm, the values of $l = 10$ and $l = 13$ mm were chosen. Finally, to compare tip lengths for the same dielectric length, the $l = 13$, $t = 1$ mm configuration was also chosen. None of the $l = 16$ mm designs was built because they do not offer any advantage over the shorter lengths. Table 5.1 summarizes the MTM configurations chosen for the measurements.

Dielectric Length, l (mm)	Metal Tip Length, t (mm)
6.5	4
10	4
13	1
13	2
13	4

Table 5.1: MTM configurations chosen to build prototype antennas.

Several prototypes were built for each configuration to ensure that the results are reproducible.

5.1.3 Saline Solution

A 9 ppt saline solution is made by adding 8 grams of NaCl to 900 ml of distilled water. To confirm that the solution has a salinity of 9 ppt, its DC conductivity is measured and compared to the theoretical value. The conductivity of saline is calculated from the equations given in [72];

$$\sigma_{saline}(T,S) = \sigma_{saline}(25,S)e^{-\Delta\alpha}$$

where

$$\begin{aligned}
\sigma_{saline}(25,S) &= S[0.182521 - 1.46192\times10^{-3}S + 2.09324\times10^{-5}S^2 - 1.28205\times10^{-7}S^3], \\
\alpha &= 2.033\times10^{-2} + 1.266\times10^{-4}\Delta + 2.464\times10^{-6}\Delta^2 \\
&\quad -S[1.849\times10^{-5} - 2.551\times -7\Delta + 2.551\times10^{-8}\Delta^2], \\
\Delta &= 25 - T.
\end{aligned}$$

S is the salinity in parts per thousand and T is the temperature in degrees Celsius measured with the mercury thermometer.

The conductivity of the solution is measured using the conductivity probe and the universal bridge. From the bridge a reading of the conductance is taken and multiplied by the K=100/m factor of the probe to obtain the value of the conductivity.

5.1.4 Reflection Coefficient Measurements

The theoretical values of the reflection coefficient are for a lossless cable but in reality the cable used for experimentation does have losses which must be accounted for in order to compare measurement and simulation. The losses of the cable are measured by calibrating the network analyzer at both ports and then measuring the S_{21} parameter with a length of the cable between port 1 and 2.

To eliminate the influence of the air/saline interface, the antennas are immersed in more than 3.5 cm of saline. This depth is determined by a series of measurements made at several depths. At a depth of or greater than 3.5 cm from the surface of the solution and from the sides and bottom of the beaker, there is no change in the results and we can safely say that the interface has no influence.

The antennas are then connected to the calibrated network analyzer and a reading of the S_{11} parameter over the frequency range of interest is taken. A PC is programmed to record the readings. The setup is illustrated in Figure 5.1. As a final step, the results are adjusted to compensate for the losses in the cable. The losses due to the connectors are not accounted for since they were found to be negligible.

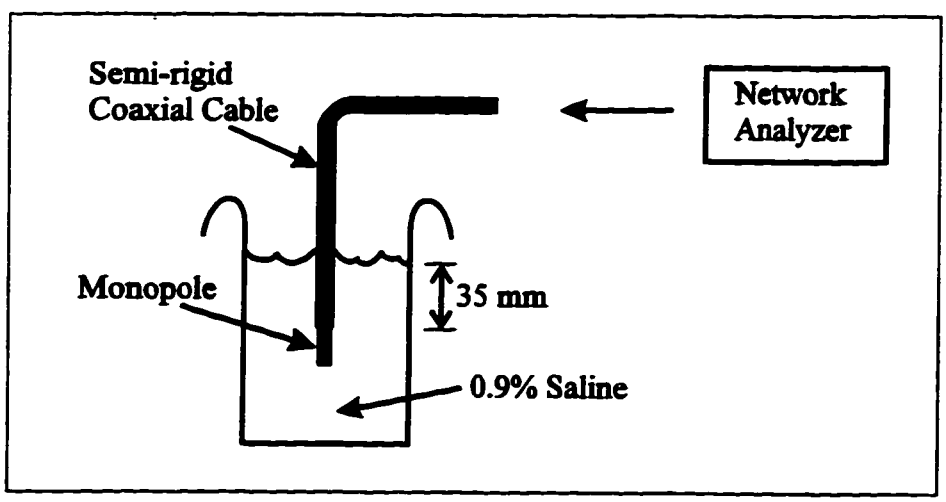

Figure 5.1: Experimental set-up for the measurement of the reflection coefficient.

5.2 Temperature Distribution Measurements

As a final step in the monopole study, the temperature distribution patterns of the prototypes are measured in phantom tissue. A procedure is used for the measurements which is readily available at a fairly low cost. It is similar to the one used in [73] where the temperature distribution is measured by placing the antenna between two saline-soaked sponges. A liquid crystal sheet (LCS) is placed on the heated face of each sponge. The sheet provides a visual display of the isotherms for a given temperature range.

Liquid crystal sheets are inexpensive and easy to handle. They offer a high spatial resolution at the expense of a relatively low absolute thermal accuracy. In this work, the use of LCS is adequate because we are interested in the comparison of various antennas and absolute accuracy is not essential.

The following sections provide the details of the equipment used and the procedure for obtaining the temperature distribution of the monopole prototypes. The details of the phantom tissue are given in the following chapter.

5.2.1 Equipment

Below is a list of the equipment that was used for the temperature distribution measurements. The set-up of the equipement is illustrated in Figure 5.2.

- Synthesized Sweeper, HEWLETT PACKARD model HP8340B
- Power Meter, HEWLETT PACKARD model 436A
- Power Meter, HEWLETT PACKARD model 432A
- Dual Directional Coupler, HEWLETT PACKARD model 77D
- 10 dB Attenuator, NARDA Microline model 774-10
- 20 dB Attenuator, NARDA Microline model 774-20
- Digital Thermometer, FLUKE model 2176A
- Precision Fine Wire Thermocouples, OMEGA model 5SC-TT-T-36-36

- 2 Cables, HEWLETT PACKARD model 5061-5458
- 386 PC
- Electronic Flash, SUNTAX model 16M+
- 35mm Manual Camera, PENTAX
- Liquid Crystal Inks on Plastic Film, EDMUND SCIENTIFIC model 72,374

To minimize the experimental errors, the attenuators, directional coupler, power amplifier, and the liquid crystal sheet were characterized with respect to their performance. The characterization of the first three items is important to accurately calculate the power flowing in the experimental setup during the measurements. The losses in the adapters and cables were measured as described in Section 5.1.4, and deemed negligible.

Attenuators

The attenuators were characterized at 2.45 GHz using a calibrated network analyzer. The 10 dB attenuator has a return loss smaller than -30 dB and an attenuation of -9.87 dB. The 20 dB attenuator has a return loss of -29.7 dB and an attenuation of -19.7 dB.

Directional Coupler

The characterization of the directional coupler was also done using a calibrated network analyzer. Its performance at 2.45 GHz is the following: directivity of -0.19 dB, coupling of -19.7 dB, isolation of -53 dB, and reflection of -26 dB.

Power Amplifier

The power amplifier was characterized by feeding it with a small power source; attenuating the output power by 30 dB; measuring this amount of power with a calibrated power meter: and comparing this measurement with the amount of power coming out of the source. It was found that for an input power of 8.55 to 9.5 dBm, the power amplifier's gain is in the range of 46.0 to 45.8 dB.

Liquid Crystal Sheets

The liquid crystal sheets are 0.14 mm thick. According to the manufacturer, the crystals can preserve their properties up to a temperature exposure of 125°C. The LCS that was used in these experiments has a temperature range of 25 to 30°C. The corresponding colours change from black (below 25°C), to red, yellow, green, and blue (29°C and above). To ensure that the LCS do have good preservation and that they correspond to the appropriate temperatures, the following experiments were done.

A piece of the LCS is placed in a water bath and the temperature of the water is varied within the proper range. At equilibrium for a given temperature, the colour is found to be uniform over the whole piece, which indicates the uniformity of the LCS. The colour observed at various temperatures are listed in Table 5.2. Several measurements were made for the same temperature and the entire experiment was repeated with the same piece and a different piece of LCS. The results were the same every time. Hence the LCS will reliably show the same colour for a given temperature.

temperature (°C)	colour shown on the LCS
$\leq$24.5	black
25.0	dark red
25.5	yellowish red
26.0	yellowish green
26.5	green
27.0	green
27.5	green
28.0	blueish green
28.5	blueish green
29.0	blue
$\geq$29.5	dark blue

Table 5.2: Colour viewed on the LCS for a given temperature.

In a different experiment, a piece of LCS is laid on a copper strip. The strip is heated by a 25 Ω, 10 W resistance. A potential difference of 7.5 V is forced onto the resistance with a power supply. The power dissipated by the resistance heats the copper strip at one end while the other end is left at room temperature ($\approx$22°C) which creates gradual cooling along the

strip. A photograph is taken of the colour gradation. The whole experiment was repeated several times, and it was found that the colour gradation was the same on all photographs. Again, these results indicate that LCS can be reliably used to view the isotherms formed around the monopoles.

As a last test, the reflection coefficient was measured for the antennas surrounded by the phantom tissue and the LCS (see Figure 5.2 b). The results match those obtained without the LCS to $\pm.1$ dB. Since there are no noticeable effects on the reflection coefficient of the antennas, we can assume that the LCS has no effect on the fields radiated by the antennas, and hence on the temperature distribution pattern.

5.2.2 Procedure

The general setup consists of a low power source (the synthesized sweeper) and a power amplifier to supply microwave energy to the antennas. The input power and reflected power are each monitored by a power meter to ensure constant power flow. The setup is illustrated in Figure 5.2 a).

The temperature distribution pattern is obtained by using two blocks of phantom tissue and a piece of LCS. The blocks measure approx. 10 by 11 cm and 4.5 cm deep. They are large enough to ensure that the tissue/air interface is far enough from the monopole not to have an effect on the measurements. The LCS has a similar area and is cut to surround the monopole applicator in a cross-section. Together the LCS and the monopole are sandwiched between the two blocks of phantom tissue (see Figure 5.2 b).

To ensure meaningful comparisons of the temperature distribution, the same piece of LCS is used to characterize all the monopoles.

The antenna dissipates a predetermined amount of power for a fixed amount of time. When the time is up, the power is shut off; the top block of phantom tissue is quickly removed and a photograph is taken of the LCS showing the isotherms.

The optimum level of power and duration of heating was determined empirically in order to achieve clear colour patterns without the effect of heat dissipation in the material which occurs with time. It was found that an application of approximately 13 W (the maximum available power) for 12 sec allowed a clearly defined temperature pattern. The pattern starts

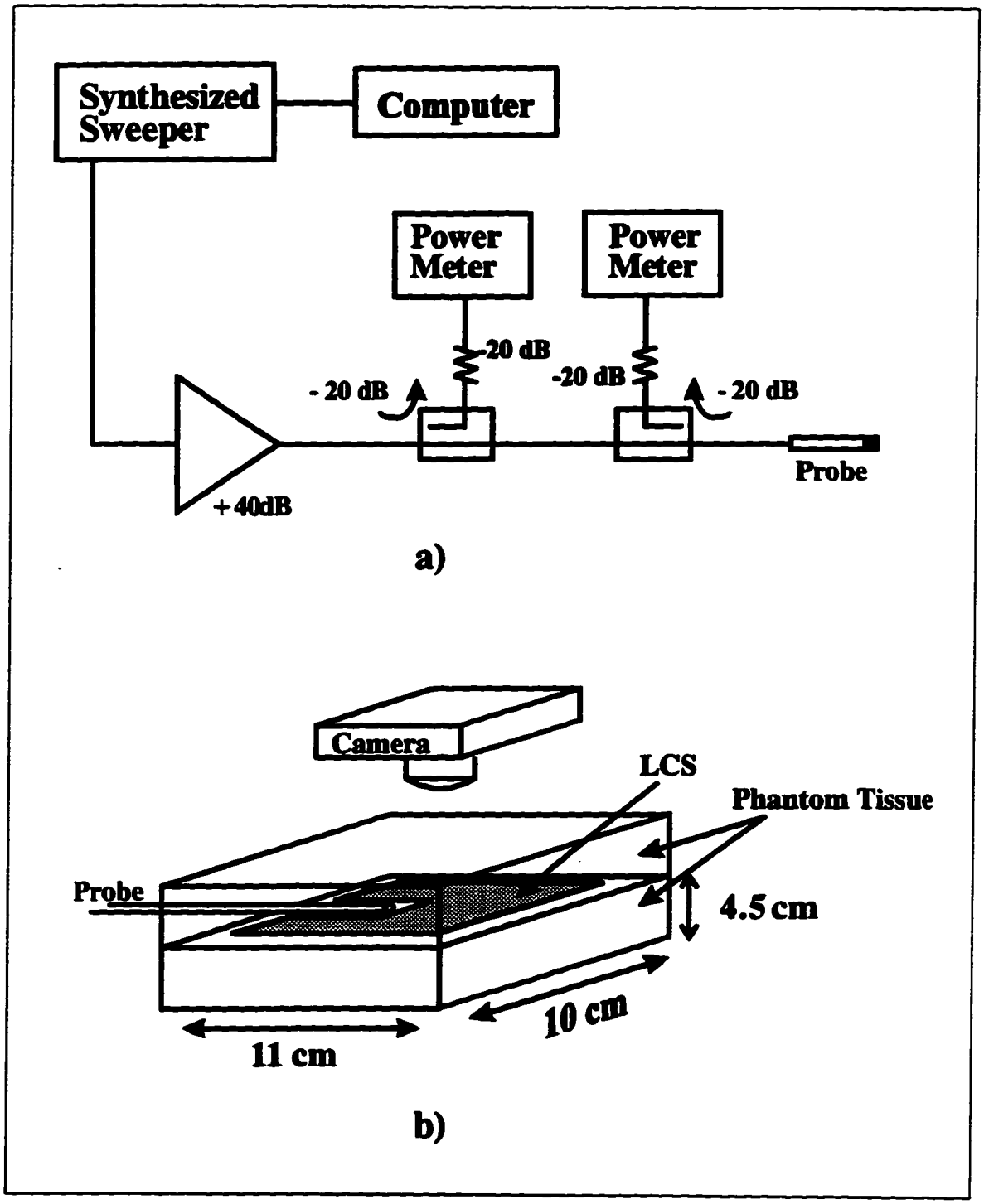

Figure 5.2: Experimental set-up and details of the split-block experiment.

monopole	S_{11}	$1-(S_{11})^2$	$1-(S_{11})^2$[dB]	norm [dB]
l=6mm,t=4mm	0.38	0.8556	−0.677	−0.9
l=10mm,t=4mm	0.49	0.7599	−1.192	−0.4
l=13mm,t=1mm	0.51	0.7399	−1.308	−0.25
l=13mm,t=2mm	0.54	0.7084	−1.497	−0.1
l=13mm,t=4mm	0.55	0.6975	−1.565	−0
open tip	0.44	0.8064	−0.934	−0.6
dielectric tip	0.41	0.8319	−0.799	−0.75

Table 5.3: Regulation of the power delivered in TEM 1 based on reflection coefficients.

monopole	S_{11}	$1-(S_{11})^2$	$1-(S_{11})^2$[dB]	norm [dB]
l=6mm,t=4mm	0.30	0.8556	−0.677	−0.95
l=10mm,t=4mm	0.51	0.7399	−1.308	−0.3
l=13mm,t=1mm	0.52	0.7296	−1.369	−0.25
l=13mm,t=2mm	0.55	0.6975	−1.564	−0.1
l=13mm,t=4mm	0.56	0.6864	−1.634	−0
open tip	0.39	0.8479	−0.717	−0.9
dielectric tip	0.42	0.8236	−0.843	−0.8

Table 5.4: Regulation of the power delivered in TEM 2 based on reflection coefficients.

to fade away only after 5 sec which allows plenty of time to remove the top block and take a picture (these last two actions take approx. 2 sec to execute). A waiting period of 10 min allows the phantom tissue to return to room temperature before the next measurement.

In order to compare the size and intensity of the isotherms viewed on the liquid crystal sheet, the same amount of power must be dissipated into the phantom. Thus the input power must be set according to the return loss of each monopole configuration. The power was regulated according to tables 5.3 and 5.4. A value of the input power was chosen for the l=13 mm, t=4 mm configuration to obtain approximately 13 W and the input power for all other configurations was adjusted with the proper normalized difference.

By empirical optimization, it was found that the liquid crystal sheet should be exposed using a flash about one meter away. The light is diffused through a thin white tissue in front of the flash in order to minimize the reflections from the liquid crystal sheet. The camera

should be set on an exposure time of 60 sec. and a 5.6 shutter speed. It is remotely operated using an air release.

In order to get some quantitative measurement of the temperature, two thermocouples were glued to the antenna: one on the tip and the other at the junction of the cable and the monopole, on the outer conductor. The thermocouple at the junction was found to interfere with the radiation pattern of the antenna and was therefore removed. The one on the outer conductor was deemed non-interfering. Since thermocouples are affected by microwave energy, the power must be shut off before taking a measurement. It was found that the temperature fell very quickly after power shut off, which made it difficult to take an accurate reading. Thus the readings from the thermocouples are omitted from the results for the simple fact that they were not precise enough to offer more insight into the characteristics of the antennas.

All measurements were made at room temperature ($\approx 22°C$). To confirm the adequacy of the experimental procedure, each prototype was tested many times in different phantom tissue blocks. The results obtained exhibited excellent conformity.

5.3 Conclusion

In this chapter, we explain the experiments used to measure the reflection coefficient and temperature distribution of several prototypes of the OTM, DTM and MTM configurations. Details are given on how the prototypes are built and preparation of 9 ppt saline solution used in the reflection coefficient measurements. The procedure for the measurement of the temperature distribution in phantom tissue is explained. The technique using split-blocks and liquid crystal sheets is both inexpensive and easily accessible. It proves to be an adequate way of displaying the temperature profiles.

In the following chapter, the details of the phantom tissue used for the temperature distribution measurements are given as well as a description of the procedure involved for its fabrication.

Chapter 6

Phantom Tissue

For meaningful results, the temperature profiles of the monopole antennas, should be measured in a medium having the same electrical properties as those utilized for the simulation. In this case the medium used in the simulations is 9 ppt saline. Unfortunately, the experimental technique used in Chapter 5 requires a medium of firm consistency that can be easily handled. For this reason, a gelatinous solution (referred to as phantom tissue) having similar properties to 9 ppt saline must be created.

Phantom tissue is quite common in biomedical experimentation. It is used to simulate bodily tissues in terms of their electrical properties (complex permittivity). The ingredients to make phantom tissue usually consist of water, sugar, salt, and a gelling agent. The proper amounts are determined empirically for the desired electrical properties. In order to determine the validity of a phantom tissue, its dielectric properties must be measured.

Complex permittivity measurements of the phantom tissue were made using an experimental set-up that was available at Health Canada. The details regarding such measurements are given in the first section of this chapter. The second section deals with the creation of the phantom tissue.

6.1 Complex Permittivity Measurements

The permittivity of a material describes its interaction with an electric field. It is defined by the following equation: $\bar{\epsilon} = \epsilon_0(\epsilon' - j\epsilon'')$, where ϵ_0 is the permittivity of vacuum (8.854×10^{-12}

F/m); ϵ' (or ϵ_r) is the relative dielectric constant; and ϵ'' is the relative loss factor. The dielectric constant describes the ability of the medium to store energy in the presence of an electric field, whereas the loss factor describes the power losses in the material. The loss factor and the dynamic conductivity are interrelated by the following relation: $\sigma = 2\pi f \epsilon_0 \epsilon''$, where f is the frequency.

The permittivity of a material sample can be measured by numerous methods either in the frequency domain or time domain. The method used in this case consists of measuring the reflection coefficient of an open-ended coaxial line immersed in the material. The permittivity can then be calculated from the measured reflection coefficient. The advantages of this method are as follows: the results have good accuracy, the calibration is simple, and a relatively small sample size can be used [74].

The theory involved in the calculation of the permittivity is presented in the following section. The materials and method for the actual measurements are given in Section 6.1.2.

6.1.1 Theory

The probe used to measure the reflection coefficient is simply an open-ended coaxial line. When this probe is immersed in a homogeneous material with a volume large enough to simulate a slab infinite in size, it can be modeled with a lumped circuit as shown in Figure 6.1 [76]. The equivalent circuit consists of two capacitive elements. A lossy capacitor, $\bar{\epsilon}C_0$, accounts for the fringing fields in the material. C_0 is the fringe capacitance when the line is surrounded by air. C_f is a capacitance which accounts for the fringing fields inside the teflon-filled coaxial line. The value of the capacitors, C_0 and C_f can be determined experimentally as discussed in [75].

This model is only valid at frequencies where the dimensions of the line are small compared with wavelength so that the open end of the line is not radiating and all energy is stored in fringe or reactive near-field of the line. Although more accurate models of the probe have been proposed in the literature [77, 74], Misra *et al.* [78] concluded that this model is adequate for frequencies lower than a few GHz.

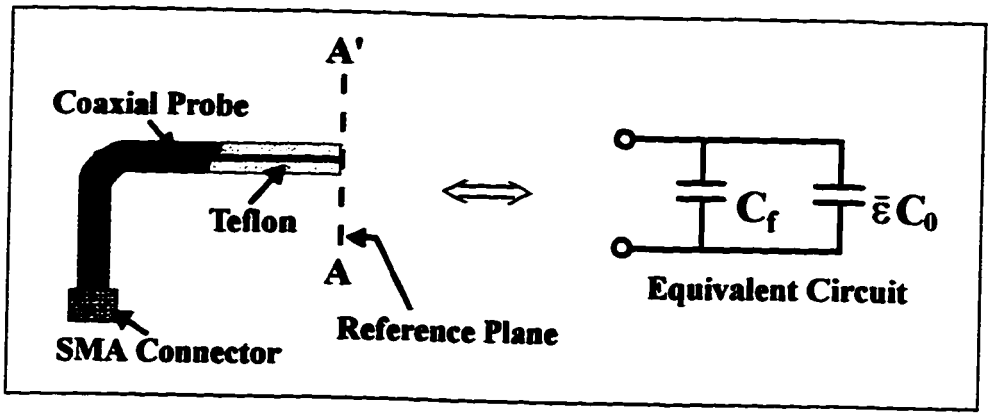

Figure 6.1: The open-ended probe and its equivalent circuit.

The admittance of the circuit can be written as:

$$Y = j\omega C_f + j\omega\bar{\epsilon}C_0 \tag{6.1}$$

where ω is the frequency in rad/sec, Z_0 is the characteristic impedance of the coaxial line. It can also be written in terms of the reflection coefficient:

$$Y = \frac{1-\Gamma}{(1+\Gamma)Z_0} \tag{6.2}$$

where Γ is the input reflection coefficient. By equating (6.1) and (6.2), the following relations are found for the permittivity:

$$\epsilon' = \frac{-2|\Gamma|\sin\phi}{\omega C_0 Z_0(1+2|\Gamma|\cos\phi+|\Gamma|^2)} - \frac{C_f}{C_0} \tag{6.3}$$

$$\epsilon'' = \frac{1-|\Gamma|^2}{\omega C_0 Z_0(1+2|\Gamma|\cos\phi+|\Gamma|^2)} \tag{6.4}$$

where $|\Gamma|$ and ϕ are the magnitude and phase angle of the reflection coefficient respectively.

An important consideration in the calculations is that the measured value of the reflection coefficient is not exact due to the imperfections of the instruments. A calibration of the instruments must be made at the reference plane where the measurements take place (at the end of the probe) in order to correct the measured value. The calibration is made using three known standards: an open-circuit termination, a short-circuit termination, and a measurement in water. These three standards have well-known reflection coefficients, Γ_1,

Γ_2, and Γ_3, that are given by [79]:

$$\begin{aligned}
\Gamma_1 &= -1 \quad \text{(short-circuit)} \\
\Gamma_2 &= \exp[-j2\arctan(\omega(C_0 + C_f)Z_0)] \quad \text{(open circuit with fringe capacitance)} \\
\Gamma_3 &= \frac{1 - j\omega C_0 Z_0 \bar{\epsilon} - j\omega C_f Z_0}{1 + j\omega C_0 Z_0 \bar{\epsilon} + j\omega C_f Z_0} \quad \text{(standard liquid)}
\end{aligned}$$

where the complex permittivity of water is calculated from the Cole-Cole equation [79]:

$$\bar{\epsilon} = \epsilon_\infty + \frac{\epsilon_s - \epsilon_\infty}{1 + (j\omega\tau)^{1-\alpha}} - j\frac{\sigma}{\omega\epsilon_0} \tag{6.5}$$

ϵ_∞ is the optical permittivity, ϵ_s is the static permittivity, τ is the relaxation time, α is the distribution parameter and σ is the ionic conductivity of the liquids. These parameters are a function of temperature (T) and are given as [53]:

$$\begin{aligned}
\epsilon_s &= 88.13769 - 3.35924 \cdot 10^{-1}T - 0.7962 \cdot 10^{-}2T^2 + \\
&\quad 0.288 \cdot 10^{-}3T^3 && (6.6) \\
\epsilon_\infty &= 4.991979 + 0.0801 \cdot 10^{-}1T - 0.0609 \cdot 10^{-}2T^2 \\
&\quad +0.0326 \cdot 10^{-3}T^3 + 0.00341 \cdot 10^{-4}T^4 \pm 0.088 && (6.7) \\
L_s &= 0.489491 + 2.8616111 \exp(-0.0399892T \pm 0.033) \\
&\quad \text{cm (wavelength)} && (6.8) \\
\tau &= \frac{L_s}{2\pi c} \text{ (c is speed of light in cm/s) s} && (6.9) \\
\alpha &= 0 && (6.10)
\end{aligned}$$

The measured reflection coefficient for the three standards are expressed as Δ_1, Δ_2, and Δ_3. From these values and the calculated ones, the error coefficients of the instrumentation, S_{11}, S_{12}, S_{21}, and S_{22}, can be calculated using the following relations [79]:

$$\begin{aligned}
S_{11} &= \frac{\Gamma_1\Gamma_2\Delta_3(\Delta_1 - \Delta_2) + \Gamma_1\Gamma_3\Delta_2(\Delta_3 - \Delta_1) + \Gamma_2\Gamma_3(\Delta_2 - \Delta_3)}{\Gamma_1\Gamma_2(\Delta_1 - \Delta_2) + \Gamma_1\Gamma_3(\Delta_3 - \Delta_1) + \Gamma_2\Gamma_3(\Delta_2 - \Delta_3)} && (6.11) \\
S_{22} &= \frac{\Gamma_1(\Delta_2 - S_{11}) + \Gamma_2(S_{11} - \Delta_1)}{\Gamma_1\Gamma_2(\Delta_2 - \Delta_1)} && (6.12) \\
S_{12}S_{21} &= \frac{(\Delta_1 - S_{11})(1 - S_{22}\Gamma_1)}{\Gamma_1} && (6.13)
\end{aligned}$$

Once we know the error coefficients, the true value of the reflection coefficient in a material, Γ, can be calculated from the measured value, Δ_m, with the following relation [79]:

$$\Gamma = \frac{\Delta_m - S_{11}}{S_{22}\Delta_m + S_{12}S_{21} - S_{11}S_{22}} \tag{6.14}$$

$$\tag{6.15}$$

and this value of Γ can be used in (6.3) and (6.4) to calculate the permittivity.

6.1.2 Materials and Methods

The equipment needed for the complex permittivity measurements consists of the following:

- Standard 50 Ω Teflon-filled 3.6 mm (OD) Semi-rigid Coaxial Probe
- SMA Connector
- Network Analyzer, HEWLETT PACKARD model HP8720C
- Microscope
- Digital Thermometer
- Personal Computer
- Sand Paper
- Aluminum Coated Paper

Before making a measurement of the complex permittivity, the probe must first be readied. Its open-end tip must be very flat with sharp edges. To ensure this, the probe is placed in a specially designed steel block, and is sanded with sand paper. The tip is then cleaned and viewed under the microscope. If there are nicks or bumps, the tip must be sanded down again.

Once the probe is ready, it is connected to the network analyzer. The next step is to calibrate the tip of the probe. The computer controls the network analyzer and records the data during the calibration. The calibration requires the tip to be in turn, open-circuit, short-circuit, and dipped in de-ionized water which is a solution of known complex permittivity.

The open-circuit is achieved by leaving the tip exposed to air. The program accounts for the fringe capacitance. To short-circuit the tip, aluminum paper is pressed flatly against it. This is a bit tricky to do but the reflection coefficient viewed on the network analyzer should indicate a magnitude of unity and a 180 degree phase difference from that of the open-circuit. The final step of the calibration is to make a measurement in water. The complex permittivity varies greatly with temperature so the temperature of the water must be measured and taken into account in the measurement. The computer adjusts all the following measurements of the reflection coefficient according to this calibration, using (6.15). It then computes the complex permittivity according to (6.3) and (6.4).

All of the above steps are critical. Therefore a verification of the calibration must be made. This is done by measuring the permittivity for two known solutions, methanol and 9 ppt saline, and comparing the results to the theoretical values at corresponding temperatures. If the values do not concur, the calibration must be redone.

The theoretical values of complex permittivity for water, methanol, and saline of a known temperature can be found by computing their Cole-Cole parameters together with the equations given in [53]. Two programs were written in C language to perform these calculations.

Finally, when a good calibration is assured, the probe is immersed in the unknown material, making sure of good contact, and the complex permittivity is determined.

6.2 Fabrication of the Phantom Tissue

For reasons given at the beginning of this chapter, phantom tissue must be developed to have similar properties to 9 ppt saline at room temperature ($\epsilon_r = 75$ and $\sigma = 2.75$). This phantom tissue will be called Phantom 1.

To ensure that the results are consistent in a medium that has slightly different electrical properties, a second phantom tissue (Phantom 2) is developed to have properties closer to that of average human muscle ($\epsilon_r = 47$ and $\sigma = 2.17$ S/m at 2.45 GHz at 37°C).

The materials and method used for fabricating phantom tissue is described next.

6.2.1 Materials and Method

A list of the equipment and the ingredients used to prepare phantom tissue is given below:

- Magnetic Hot Plate
- Magnetic Stirrer
- 500 ml Beaker
- Digital Scale, Mettler model PE 1600
- 1 l De-ionized Water
- 150 g Granular Sugar
- 8 g NaCl
- 100 g Hydroxy Ethyl Cellulose (HEC)
- 1 g Bactericide

The recipes for a specific phantom are determined empirically. Each solution is prepared using the following steps.

1. Measure the appropriate amount of water. Add in salt, bactericide and sugar if required.
2. Mix with magnetic stirrer at medium speed on the hot plate at low heat until completely dissolved.
3. Add in small amounts of HEC at a time.
4. Mix slowly until very thick and close to solidification. Pour in mold and cover.

The hot plate was kept warmer when sugar was used to help it dissolve faster.

After each solution, a sample of the phantom is used to measure its dielectric properties. If they are not adequate, the whole procedure is repeated varying the proportions of the ingredients. The quantities given in the list of materials are plenty to make one recipe of each phantom given in the next section, using 400 ml of water.

	9ppt saline [53]	Phantom 1	average muscle [52]	Phantom 2
Temp [°C]	21.3	21.3	37	21.3
ϵ_r	75	69 ± 5%	47	48 ± 5%
σ [S/m]	2.82	2.86 ± 5%	2.17	2.33 ± 5%

Table 6.1: Comparison of dielectric constants and conductivities at 2.45 GHz.

6.2.2 Final Recipes and Their Electrical Properties

The final recipe for Phantom 1 was: 90.14% water, 9.01% HEC, 0.76% salt, and 0.09% bactericide. The final recipe for Phantom 2 was: 62.28% water, 27.40% sugar, 9.97% HEC, 0.25% salt, and 0.10% bactericide. The bactericide is added to preserve the phantom.

Each recipe was made several times and each time, a sample was kept aside for measuring the complex permittivity. Several measurements of the complex permittivity were made on various places of the samples, and with different calibrations. This was to determine conformity and uniformity. The average properties of the phantom tissue are listed in Table 6.1 and compared to 9 ppt saline and average muscle.

Several observations can be made about the phantom tissue.

- NaCl increases conductivity; sugar and HEC lower permittivity; and water increases permittivity.
- The phantom tissue is firm, yellowish and translucid. This last property helps in verifying the position of the probe while making measurements.
- Phantom 1 has a homogeneity that fluctuates by less than 1.5%. The homogeneity of Phantom 2 fluctuates by 2.5%, a bit more than Phantom 1.
- Care and precision must be exercised in making the recipes since the complex permittivity can vary with the properties and quantities of the ingredients, the homogeneity of the solution, and the precision of the calibration for the measurements.
- The phantom tissue can withstand heating up to 80°C without deterioration. This was verified experimentally.

- The complex permittivity varies linearly with the temperature. In the temperature range of interest (20-30°C), it only varies by a few percent.

6.3 Conclusion

This chapter focused on the fabrication of phantom tissue required for the experimental temperature profile measurements of the antennas. Two phantoms are developed having similar properties to that of normal saline and heart muscle. To assess their conformity and uniformity, the phantoms are fabricated several times and the complex permittivity is measured many times for each recipe. The system used for the permittivity measurements is also discussed in order to establish good confidence in the results obtained.

The fabrication of the phantom tissue is the last step before the actual experimental measurements of the temperature distribution of the antennas. In the next chapter, we present both the theoretical and experimental results that characterize the antennas.

Chapter 7

Study of Monopole Antennas for Microwave Ablation

Before presenting and discussing the numerical and experimental results, the antenna requirements for MW ablation are recalled below:

- Small physical dimensions
- Good conformity to the catheter
- Exposed metallic parts
- Low reflection coefficient
- Uniform heating pattern

In the following section, the characteristics of the three monopoles are illustrated by numerical and experimental results. The antennas are compared in a discussion of their performance and how well they meet the above criteria. An optimization of the antenna that best fulfills these requirements is then presented. After a discussion of the results, recommendations for MW ablation are given.

7.1 Modeling of Monopoles

In order to better understand the differences between possible monopole designs, the three monopoles of Figure 3.1 are simulated. Experimental measurements are conducted to confirm the simulation results.

7.1.1 Magnetic Field

Figure 7.1 displays the magnitude of H_ϕ calculated for each configuration inside the dielectric and around the antenna for an input voltage of 1 V (peak) at 2.45 GHz. The DTM shows a null field at the tip increasing towards the junction ($z = 0$). The field is much more uniform on the OTM but nonetheless decreases towards the tip. The MTM displays a minimum of the field at the junction and a maximum near the tip.

The magnetic field plots can be interpreted on the basis of the quasi-static approximation. Under this approximation, H_ϕ near the antenna is given by $I(z)/2\pi r$, where $I(z)$ is the current on the antenna. Therefore, the distribution of H_ϕ close to the z-axis is a good indication of the current distribution on the antenna.

In Figure 7.1 a), the results show that the DTM has a current null at the tip. This agrees with King [42] (see Section 3.3) which states that an insulated antenna of this type behaves like a lossy coaxial line terminated in an open-circuit at the tip.

Extending King's transmission line analogy, one can predict that the antenna current for the OTM and the MTM should be different than zero at their tip because the center conductor is in contact with the lossy ambient medium. This is confirmed by the results of Figure 7.1 b) and c). These results also reveal a considerable difference between the two current distributions. For the OTM the current magnitude is constant for the first half of the monopole and drops gradually towards the tip. For the MTM, the current magnitude varies along the antenna with the characteristics of a standing wave. At the metal-tip junction ($z = 13$ mm), the total current on the inner conductor should be the same as the total current flowing on the surface of the metal-tip. This is confirmed by the continuity of the magnetic field at $z = 13$, $r = 0.84$ mm (Figure 7.1 c). Further along the tip itself, the current drops rapidly because it spreads in the surrounding medium.

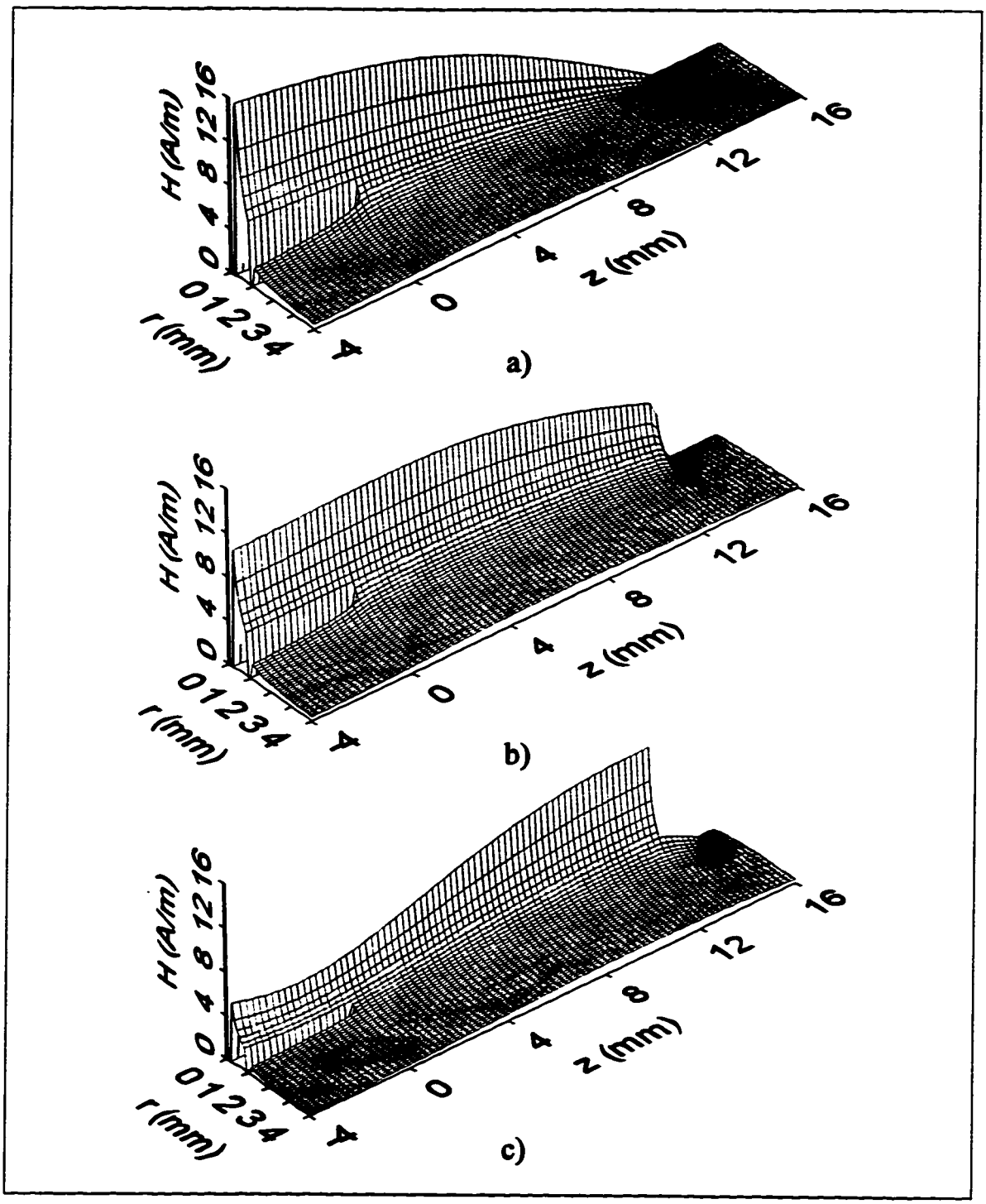

Figure 7.1: Magnitude of H_ϕ around the a) DTM, b) OTM, and c) MTM. The inner and outer conductors of the coaxial cable are at $r = 0$ and $r = 0.84$ mm respectively.

Figure 7.1 also shows the current flowing on the exterior of the outer conductor of the coaxial line, near the junction. In interstitial microwave hyperthermia, this current is problematic because it varies with the insertion depth of the applicator. Consequently, the heating pattern and reflection coefficient of the antenna also depend on the insertion depth, which is undesirable. A sleeve balun has been proposed to eliminate the current [69]. No such problem is expected in microwave ablation because the catheter is largely inside the body and the air interface is too far away to have an effect on the antenna at its tip.

7.1.2 Reflection Coefficient

In Figure 7.2 the reflection coefficients of the antennas are presented as functions of frequency. The OTM is very well matched ($|S_{11}| < -20$ dB) around 2.45 GHz. The MTM is well matched at low frequencies but at 2.45 GHz, S_{11} is only close to -5 dB. The curve for the DTM presents a wide minimum at 4 GHz comparable to measurements obtained from similar insulated antennas used for hyperthermia [47] but again at 2.45 GHz, S_{11} is only slightly better than -5 dB.

Also shown in Figure 7.2 are the experimental measurements of the reflection coefficient. These are well in agreement with the simulation results which suggest that the numerical model is valid.

The reflection coefficients at 2.45 GHz confirm the observations on antenna currents given in the previous section. The OTM presents a very low return loss indicated by the constant current magnitude up to $z = 6$ mm. On the other hand, the DTM and MTM present a standing wave pattern which in the latter case is responsible for increased tip heating.

7.1.3 Heating Patterns

Calculated SAR patterns at 2.45 GHz are plotted in Figure 7.3 for the three antennas. The curves show the longitudinal variation of the SAR at $r = 1.5$ mm. For better comparison, the data is divided by $(1-|S_{11}|^2)$ and normalized to 30 kW m^3 so that the total power dissipated is the same in all cases. The plot reveals that the SAR distributions differ significantly from one antenna to another. The DTM has a highly concentrated SAR near the junction and

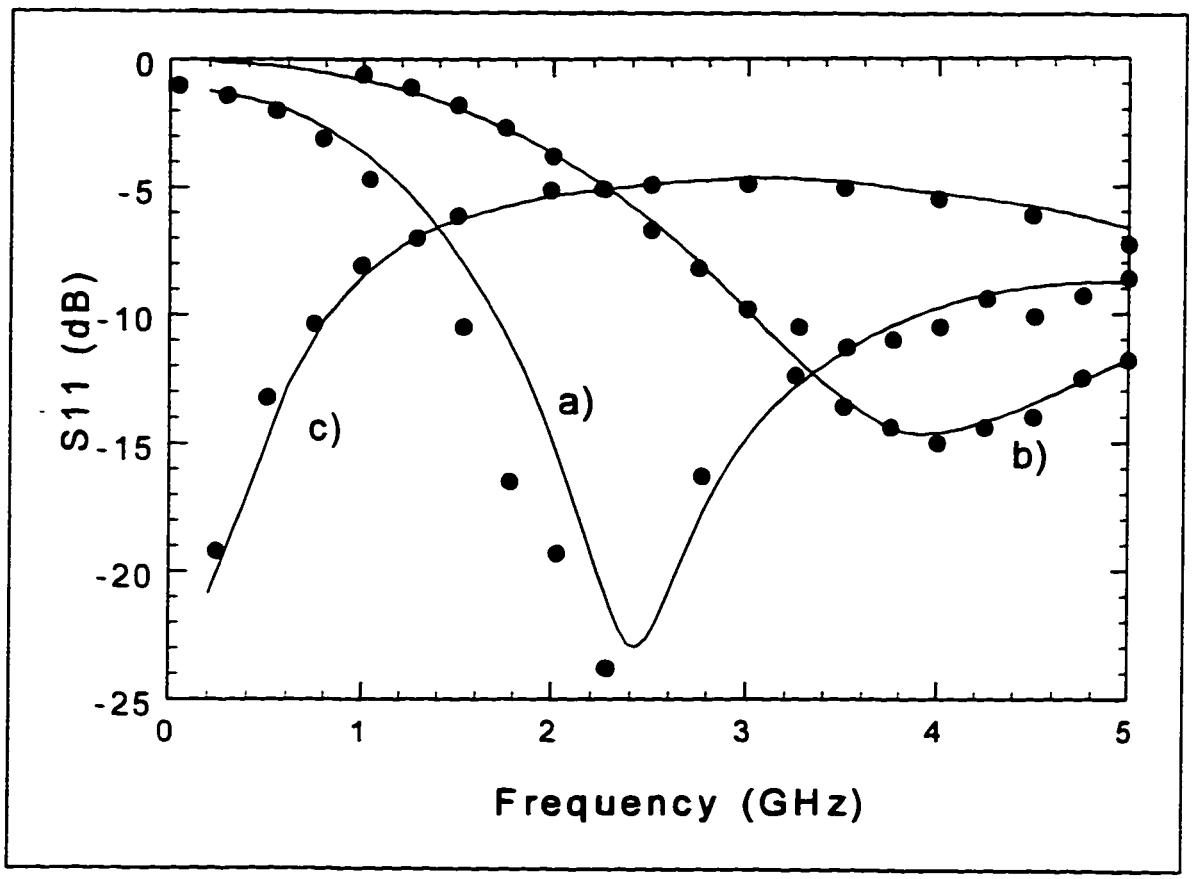

Figure 7.2: Reflection coefficient for a) OTM, b) DTM, and c) MTM. The solid curves are calculated, the discrete points are experimental.

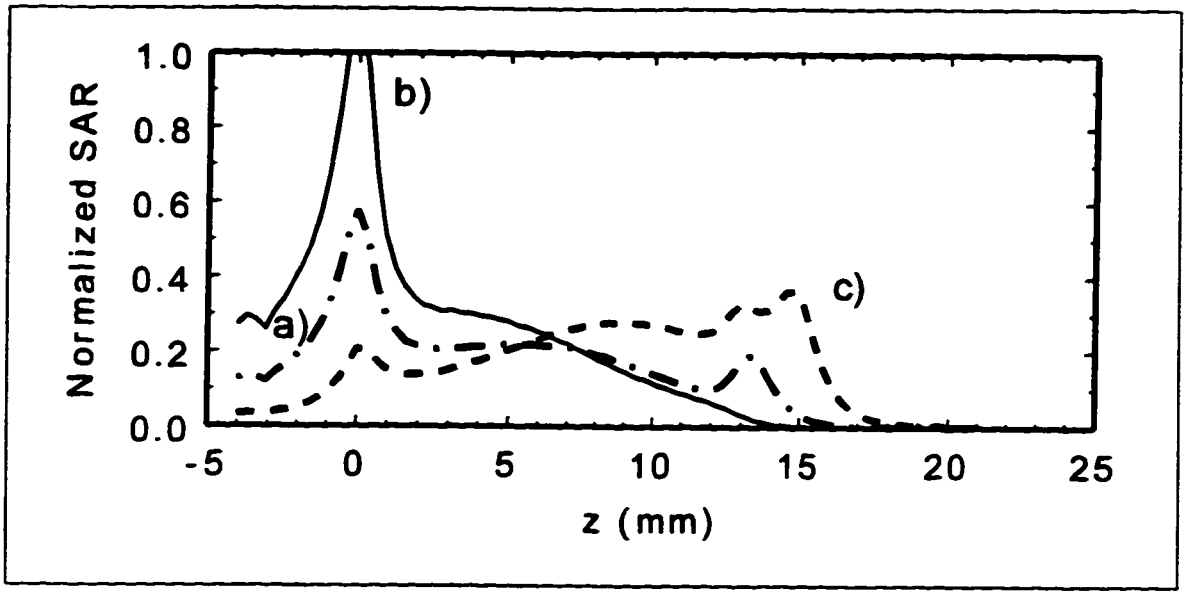

Figure 7.3: Calculated SAR patterns at $r = 1.5$ mm for a) OTM, b) DTM, and c) MTM. Curves are normalized to 30 kW m^{-}3. Curve a) peaks at 1.13.

almost none at the tip. The MTM has a more uniform distribution with a wide maximum around the tip. The OTM displays intermediate characteristics.

Figure 7.4 shows the temperature distribution recorded in Phantom 1. The blue, green, red and black color degradation corresponds to a decrease in temperature as mentioned in section 5.2.1. In all cases, power was applied for 12 seconds. Its intensity was 13.4 W for the OTM, 13.4 W for the DTM, and 11.8 W for the MTM.

Similar observations to the ones made from the SAR patterns are noted. Little heating occurs at the tip of the DTM compared to the other antennas. The shape of the isotherms clearly indicates that the DTM has a hot spot at the junction; the OTM has two hot spots, one at the tip and one at the junction; while the MTM has uniform heating with some at the tip and little along the outer conductor. These observations agree and confirm those of the numerical model.

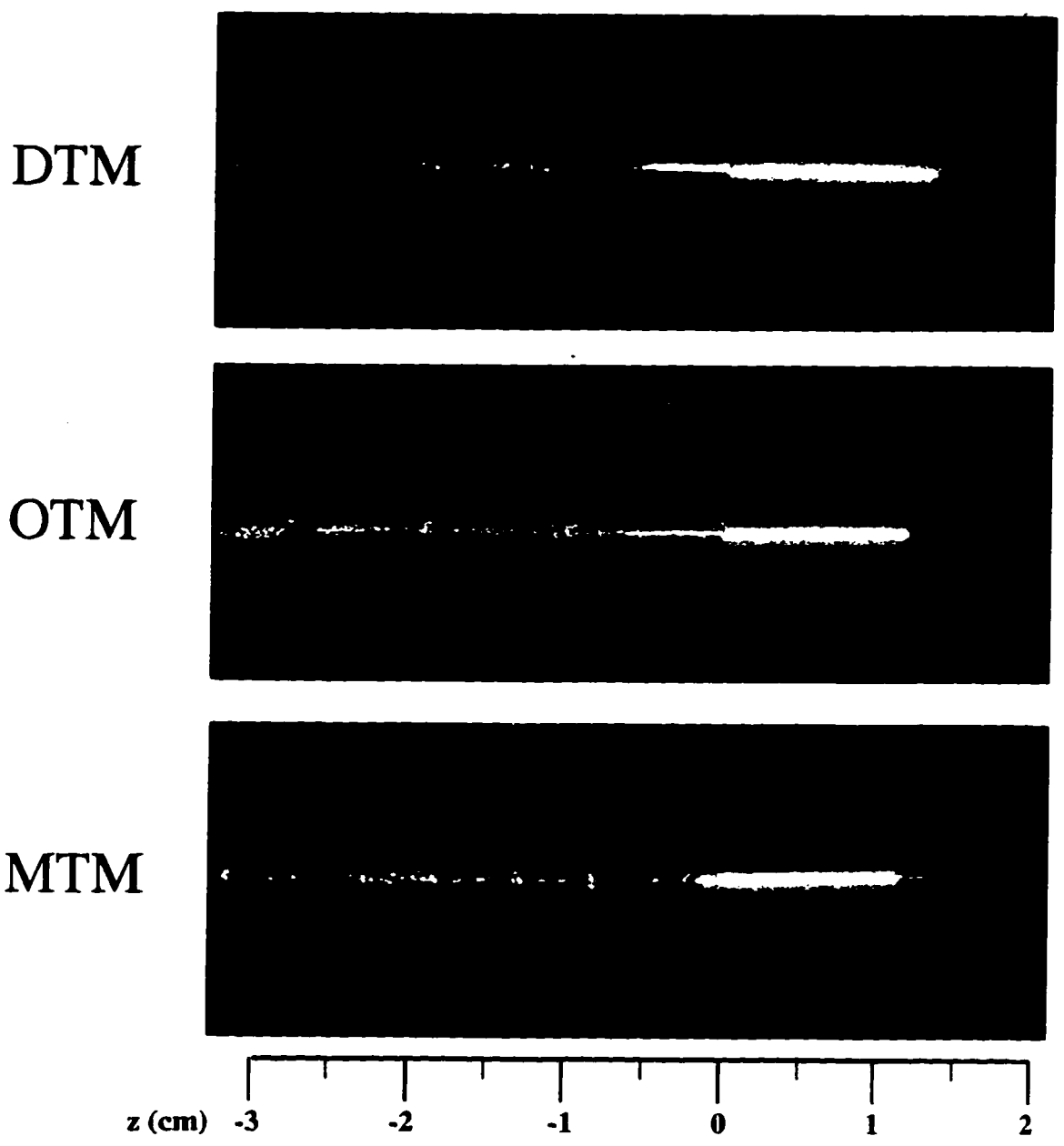

Figure 7.4: Temperature distribution of the DTM, OTM and MTM produced in Phantom 1.

7.1.4 Discussion

The three monopole designs are an extension of a coaxial cable, which becomes the catheter for MW ablation. Hence, the monopoles do conform well to the catheter. In addition, the cable has a diameter of 2.159 mm which is small enough for catheterization. The length of the monopoles, however, is bordering the limits for MW ablation, depending on how big a lesion is required. Judging from the SAR patterns and temperature distribution, heating would occur over a length of 13 mm or more.

The DTM does not have an exposed metallic part near its tip, which complicates the recording of electrocardiograms and thus catheter positioning. Furthermore, it produces a highly non-uniform heating pattern. The return loss could possibly be improved by increasing the length of the antenna but this would make it too long for practical use. The DTM is thus of limited practical interest for microwave ablation. However, it serves as a convenient means of verifying the numerical procedure and provides useful insight into the physics of the problem.

The OTM is very well matched in its current state and has a relatively uniform heating pattern. The exposed end of the inner conductor at the tip of the antenna can be used for electrocardiograms, but its small size may limit its effectiveness for this purpose. On the other hand, the MTM offers a uniform heating pattern and a large exposed metallic tip but it has a fairly high reflection coefficient at 2.45 GHz (−5 dB).

Because of the ease with which electrocardiograms can be measured, the MTM represents the best overall compromise for microwave ablation. However, the return loss of the MTM needs improvement. An attempt is made to do so in the following section by varying the dimensions of the MTM and assessing the influence on the antenna performance.

7.2 Optimization of the MTM

Two parameters of the antenna are varied so as to observe the effect on the S_{11} and on the SAR: the length of the exposed dielectric, l, and the length of the metallic tip, t. Twelve distinct configurations are modeled with l = 6.5, 10, 13 and 16 mm and t = 1, 2 and 4 mm. Larger dimensions are not considered because they are impractical for catheter ablation.

7.2.1 Magnetic Field

Plots of the magnetic field are shown in Figure 7.5 for three MTM's of various lengths: $l = 6.5$, 10, and 13 mm with $t = 4$ mm. For conciseness, only these field results are shown since the results obtained from other dimensions can easily be inferred from them. The magnetic field distribution varies smoothly and in a predictable manner as l increases. The plots show that the current on the exterior of the outer coaxial conductor ($z < 0$) is minimized for the longest antenna. This can be related to the fact that for this antenna, the inner conductor current is at a minimum at the junction (see Section 3.3). Figure 7.5 also reveals that for all MTM's, current flows along the entire length of the metal tip.

7.2.2 Reflection Coefficient

The S_{11} results are plotted in Figure 7.6 for all monopoles. Generally, for a given antenna length, l, the tip length, t, does not affect S_{11} significantly between 1.5 and 3.5 GHz. The exception is for $l = 6.5$, $t = 4$ mm which results in $|S_{11}| = -9$ dB, 2 dB less than with the other t values. At 2.45 GHz and for a given length t, S_{11} increases with l by roughly 2 dB for $l = 6$ to $l = 10$ mm and less than 1 dB for $l = 10$ to $l = 16$ mm. The best matched monopole at 2.45 GHz is $l = 6.5$, $t = 4$ mm with -9 dB return loss which is not perfect but it is acceptable.

Figure 7.7 shows plots comparing the calculated and measured reflection coefficient for the prototypes. Again, there is good agreement in general. The largest discrepancy is 0.5 dB for the $l = 13$, $t = 4$ mm between 1 and 2 GHz.

7.2.3 Heating Patterns

Curves of normalized SAR versus z at $r = 1.5$ mm are shown in Figure 7.8 for all monopoles. The SAR patterns are characterized in all cases by three peaks caused by edge effects: one at the junction, and one at each of the 2 edges of the metal tip. Depending on t, the latter two may overlap to some extent. With $t = 1$ mm, they merge and form only one peak. With $t = 4$ mm, they are clearly separated. The length t of the metal tip thus has a direct influence on the uniformity of the SAR. For $l = 6.5$ and 10 mm, the SAR peaks at the junction and at the

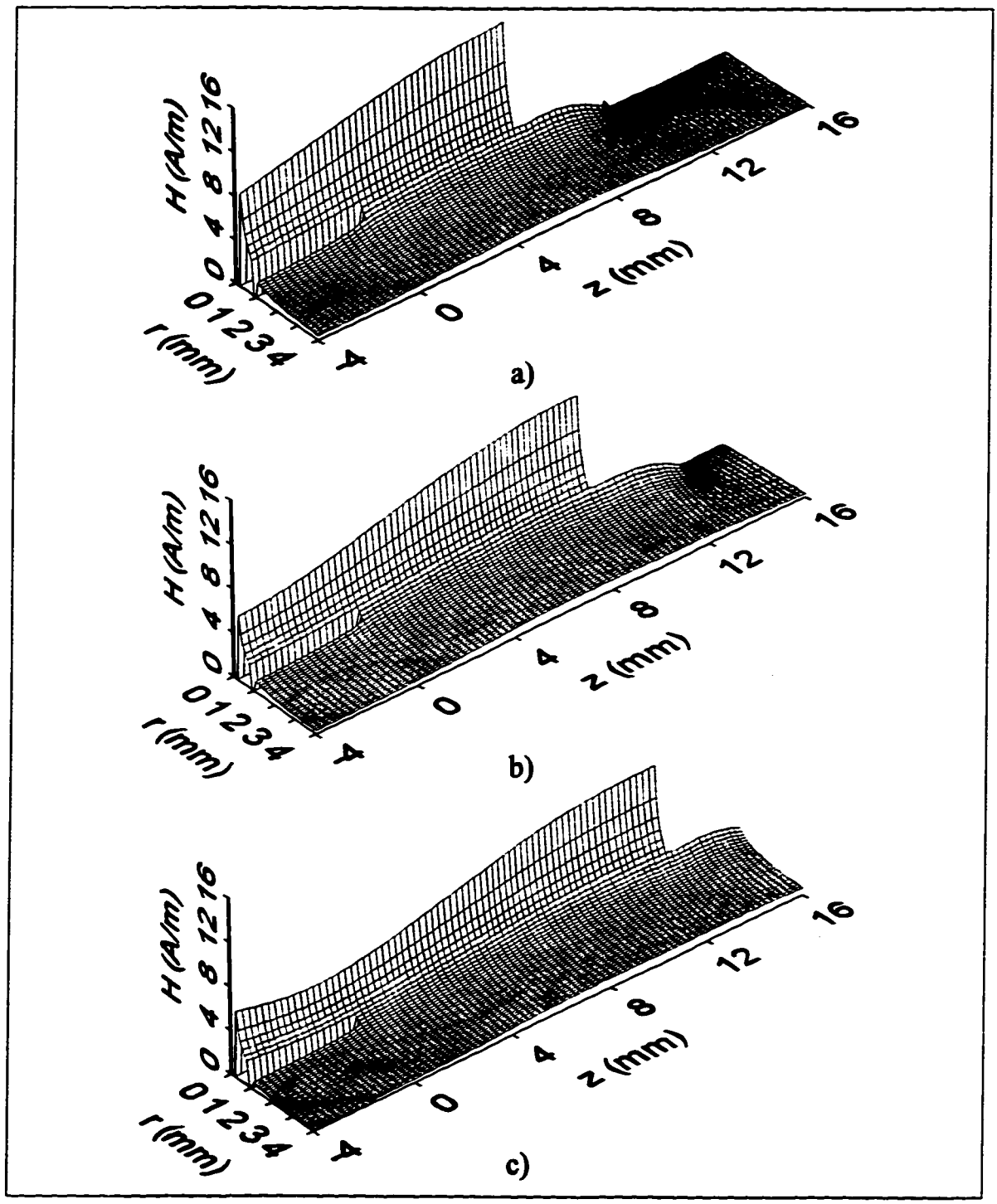

Figure 7.5: H_ϕ for 3 MTM's: a) $l = 6.5$, $t = 4$ mm, b) $l = 10$, $t = 4$ mm, and c) $l = 13$, $t = 4$ mm.

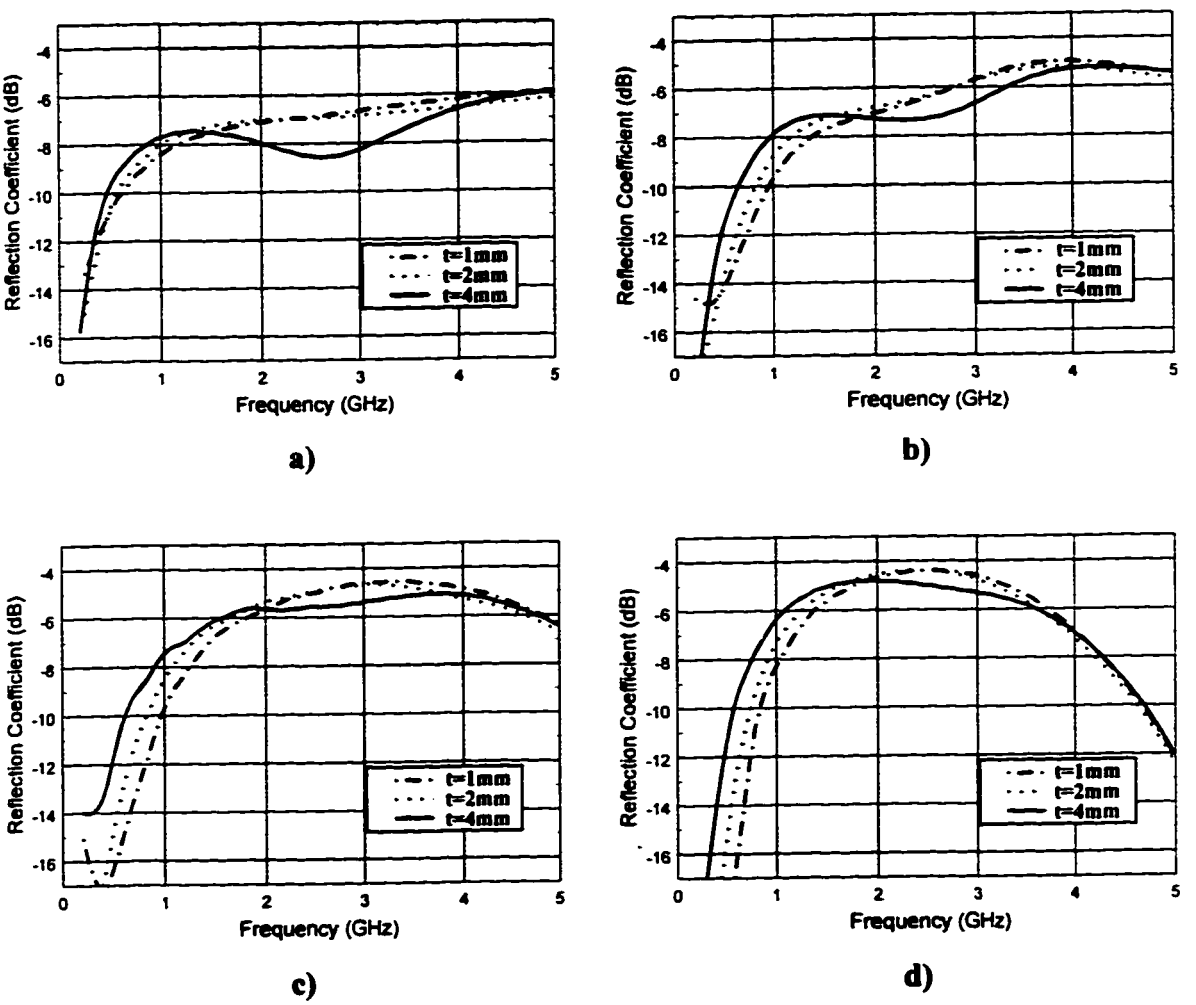

Figure 7.6: Numerical calculations of the magnitude of the reflection coefficient for MTM a) $l = 6.5$, b) $l = 10$, c) $l = 13$, and d) $l = 16$.

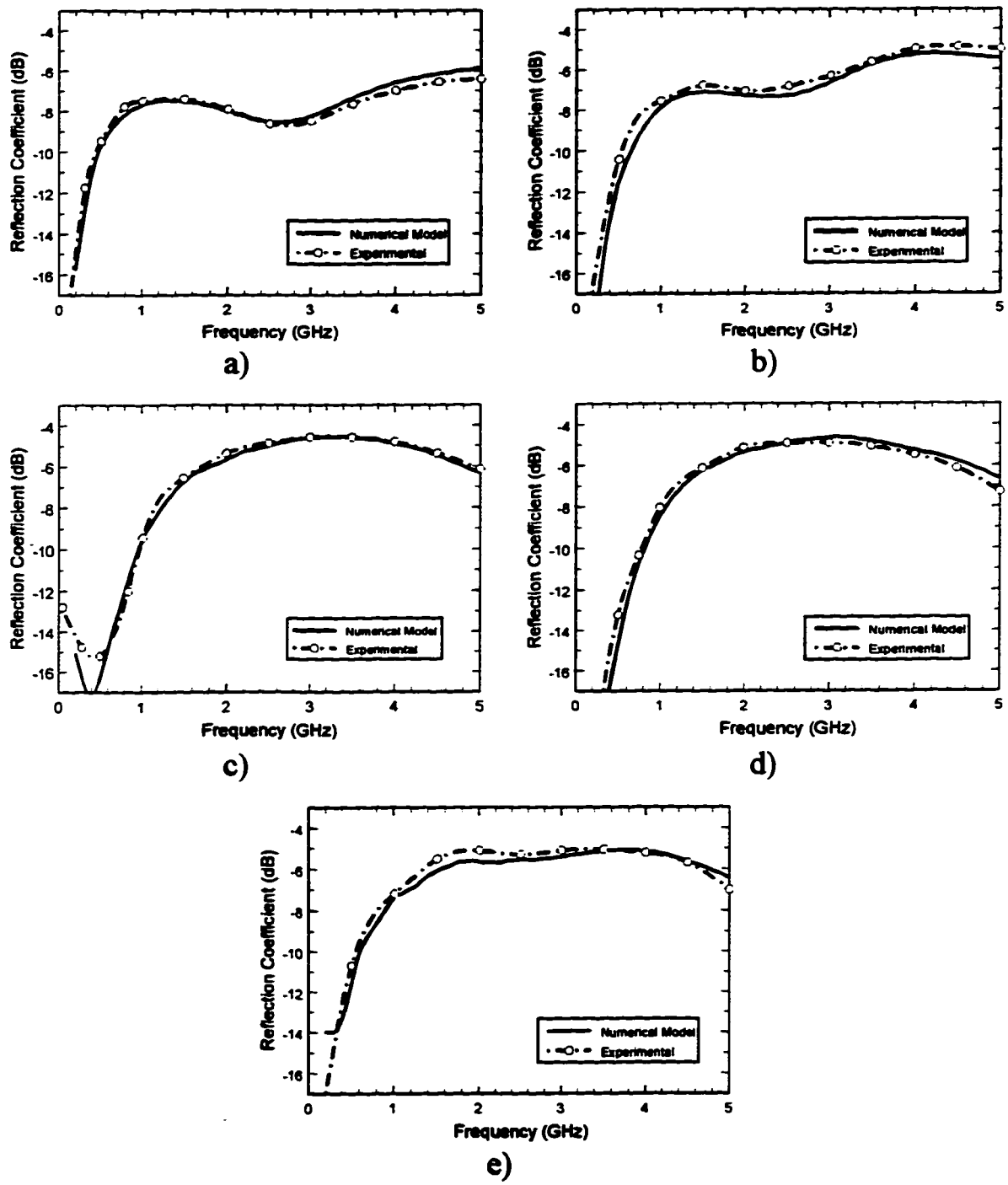

Figure 7.7: Reflection coefficient for MTM a) $l = 6.5$, $t = 4$ mm, b) $l = 10$, $t = 4$ mm, c) $l = 13$, $t = 1$ mm, d) $l = 13$, $t = 2$ mm, and e) $l = 13$, $t = 4$ mm.

tip of the antenna are of similar magnitude. For $l \geq 13$ mm, heating becomes more important at the tip than at the junction. Given this behavior, it appears that using a monopole with $l > 13$ mm is detrimental to SAR uniformity. The curves reveal that the most uniform SAR is obtained with $l = 13$ and $t = 2$ mm.

The radial variation of the SAR has also been studied and is presented in Figure 7.9. In this respect, all antennas behave similarly. At the edges of the metal tip and at the junction of the antenna, the SAR values are very high and decay rapidly radially as shown in curve b). At other points along the antenna where SAR values are lower, the radial rate of decrease is also lower. As shown in curve a), the SAR decreases by roughly 50% 1 mm away from the antenna surface.

As a final step in the monopole study, the temperature distribution of the MTM prototypes are measured in Phantom 1. The results are shown in Figure 7.10. The power applied for 12 seconds during the measurements was constant at 12.8 W for the l=6.5, t=4 mm, 13.8 W for the l=10, t=4 mm, 11.8 W for the l=13, t=2 mm, and 13.5 W for the l=13, t=4 mm configuration. All prototypes display smooth isotherms with significant heating near the tip. The increased heating of short monopoles along the outer conductor of the cable is also evident but it is unclear whether this is a drawback for ablation. In all cases, the isotherms cover the whole length of the applicator as desired. They are of comparable size and do not permit one to identify the best monopole length between 6.5 and 13 mm. The temperature distribution was also measured for all prototypes in Phantom 2. The results are similar to the previous ones and the same conclusions are drawn.

7.2.4 Discussion

As a result of this investigation, no monopole seems to satisfy all the requirements of catheter ablation. With $l = 6.5$ and $t = 4$ mm, the reflection coefficient is about -9 dB at 2.45 GHz, which is acceptable. Unfortunately, the SAR is suboptimal as heating is concentrated at the junction and the edges of the tip. This may cause problems in practice because of blood and tissue coagulation at these hot spots. However, due to surface cooling during ablation [70], the thermal distribution produced in the tissue may in fact be satisfactory. *In-vitro* experiments appear necessary to resolve the issue. The overall length of this applicator is

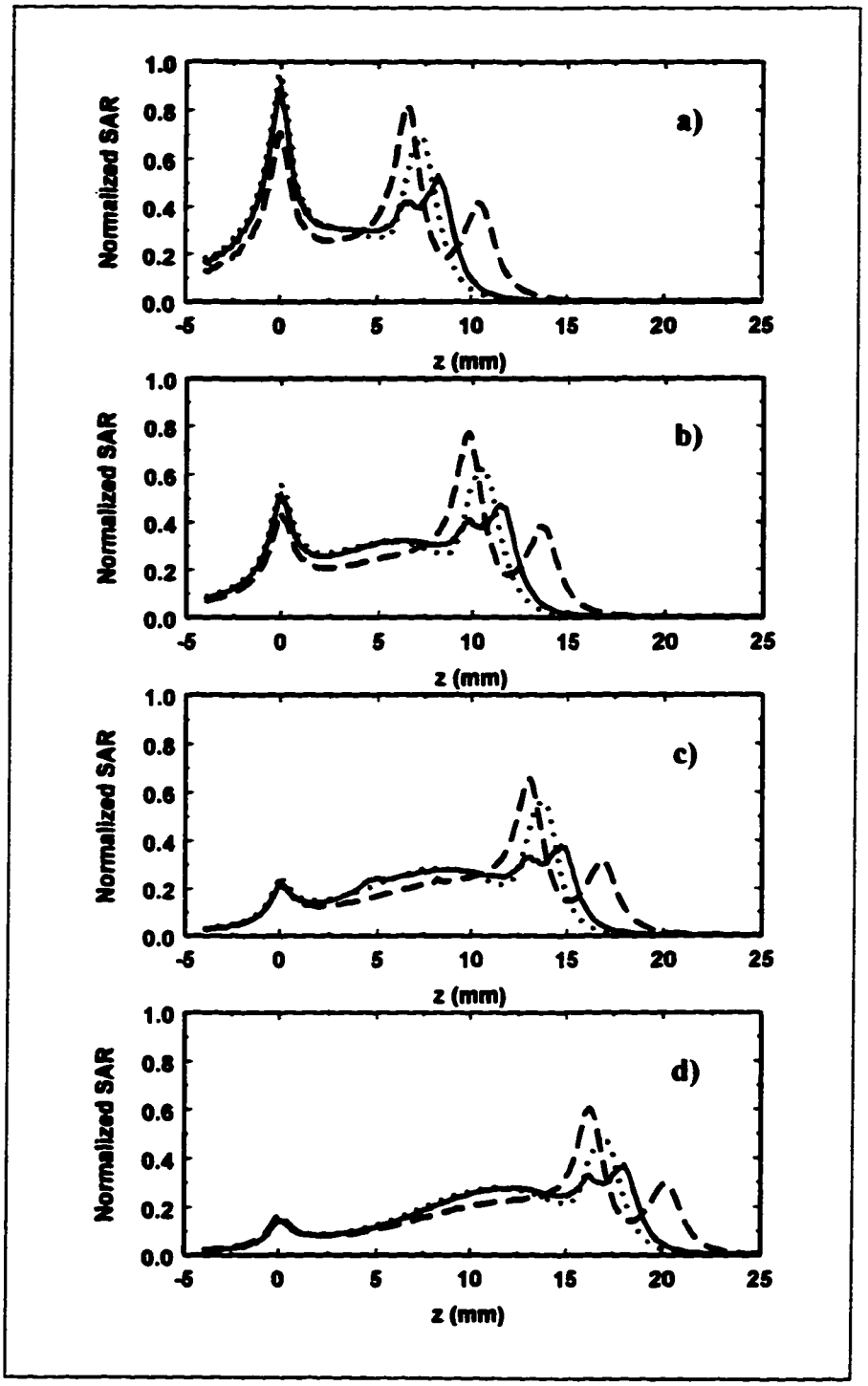

Figure 7.8: Normalized SAR at $r = 1.5$ mm for all MTM's at a) $l = 6.5$, b) $l = 10$, c) $l = 13$, and d) $l = 16$ mm. In each case the dotted line is for $t = 1$, the solid line for $t = 2$ and the dash line for $t = 4$ mm.

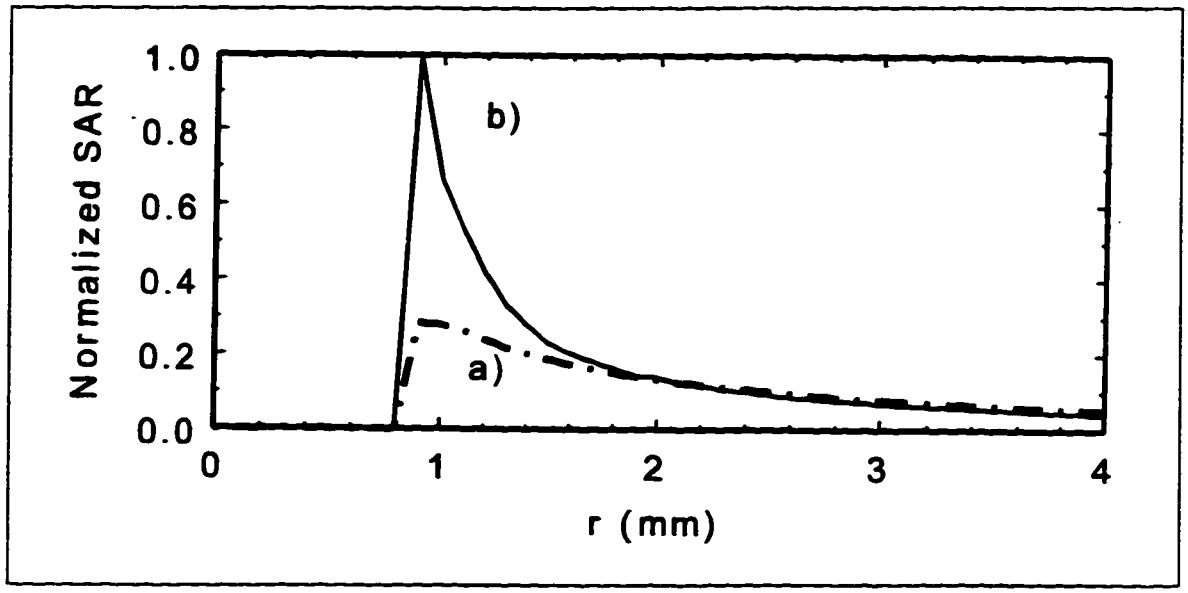

Figure 7.9: SAR patterns for $l = 10$, $t = 2$ mm at a) $z = 5$ and b) $z = 10$ mm.

10.5 mm which is adequate for catheter ablation.

The monopole with $l = 13$ and $t = 2$ mm does not present high SAR peaks and would undoubtedly produce large and uniform tissue lesions. Unfortunately, the S_{11} is fairly high at 2.45 GHz. This means that for a given amount of power dissipated in the tissue, more power is dissipated as heat in the catheter itself (because of inevitable losses) than with a better matched antenna. Of course, during ablation the catheter is continuously cooled by the flow of blood but it is not known at the moment if the catheter temperature would be low enough to avoid patient injury or catheter failure. The antenna has an overall length of 15 mm which seems fairly large for catheter ablation but may not be impractical. Again, more experimental work must be conducted to clarify this matter.

The temperature distribution measurements are in agreement with the observations made from the SAR pattern. However, an important feature not shown in Figure 7.10 is the fact that near the antennas, the temperature is higher for the short monopoles than for the longer ones due to the higher SAR. We have seen in Section 2.2.2 that during RF ablation, the maximum tissue temperature must not exceed 100°C to avoid tissue coagulation which limits current flow and lesion growth. However MW ablation may not be limited to this temperature

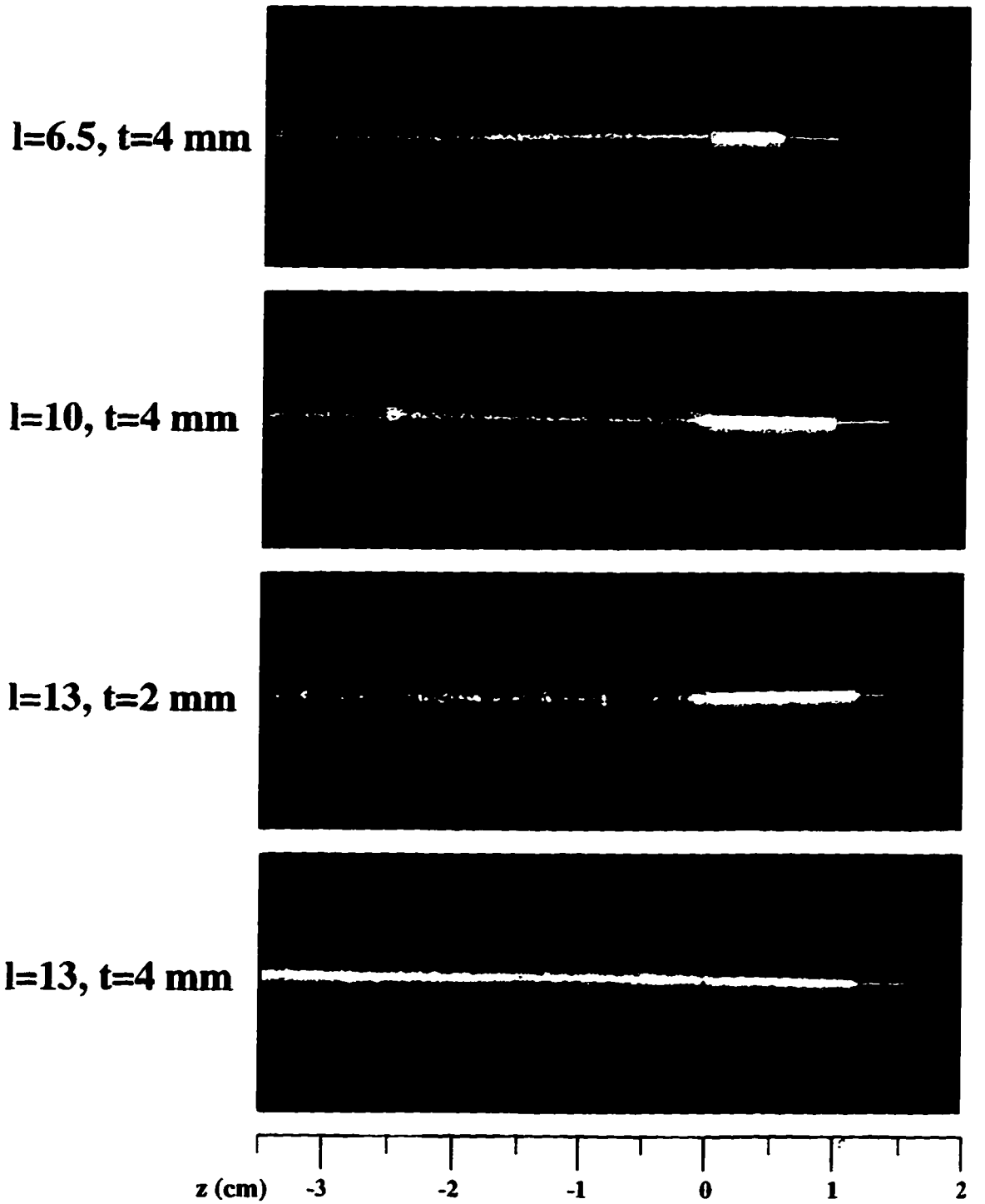

Figure 7.10: Temperature distribution of the MTM l=6.5, t=4 mm, l=10, t=4 mm, l=13, t=2 mm, and l=13, t=4 mm produced in Phantom 1.

because the process does not rely uniquely on conduction current. Nonetheless, it is likely that for other considerations, limiting the tissue temperature to a certain maximum value would also be relevant to MW ablation. In view of this, more power could be applied and larger lesions could be achieved with the longer antennas.

7.3 Future Work

The theoretical and experimental evaluation of the monopole antennas does not lead to a better performance than that obtained recently by Lin *et al.* with their cap-choke antenna [38]. This antenna has uniform SAR with heating at the tip and a very low reflection coefficient of -17 dB, which seems optimal. However, the MTM does present the advantage of being easily constructed.

The next step in the monopole antenna investigation is to assess the actual lesion size achievable. With *in vitro* measurements conducted on a bovine heart immersed in saline, the energy level and exposure duration required to achieve significant lesion size can be determined. In addition, the lesion size can be compared to the lesions obtainable during RF ablation. If these results are promising, a prototype can then be built using a low loss flexible coaxial cable. *In vivo* measurements conducted in animal subjects for ventricular tachycardia (VT) would be the next step. With such measurements the feasibility of treating VT would be established, along with the effects of the reflected power at the junction of the cable and the antenna, and the effects of high SAR peaks. The results would indicate whether further clinical studies should be conducted.

Another interesting challenge is the design of the cable used for catheterization. As the dimensions of the cable decrease, its losses increase. To compensate for the losses in the cable, it must be supplied with a higher power level for some fixed amount of power delivered to the distal antenna. Higher levels of power and losses in the cable means more power dissipated inside the cable which creates heating that can be dangerous for the patient. Therefore, the cable must be carefully designed to minimize losses. In addition, the cable must be small and flexible enough for catheterization but it must also be robust enough so that it does not break inside the patient. Finally, the cable must be able to withstand a significant amount

of power without dielectric breakdown.

Chapter 8

Conclusion

In this research, three monopole antenna designs are studied for MW ablation. A theoretical study is chosen for the following reasons: it provides a more thorough understanding of the behavior of the antennas; such an understanding leads more easily to an optimum geometry; and finally, experimental research necessitates medical expertise and equipment that is considerably more specialized than what is readily available.

A model of the real-life situation is used by considering the axisymmetry of the antennas in a homogeneous medium. This model is sufficient to characterize the behavior of the antennas in a lossy medium having properties similar to those of the heart. In addition, the model greatly simplifies the rather complex geometry of the problem. The model is analyzed using the Finite Element Method to solve for the magnetic fields. The results are used in post-processing to calculate the reflection coefficient and SAR patterns of the antennas.

Experiments are conducted to measure the reflection coefficient and temperature patterns of several prototype antennas, thus confirming the theoretical results. The reflection coefficients are measured in normal saline and the results agree well with the theoretical calculations which indicates that the numerical treatment of the model is valid. A novel way of measuring the temperature patterns is proposed using blocks of gel and a liquid crystal sheet, which is employed to reveal temperature increases. This method is an inexpensive way to view the isotherms created by the antennas during the application of MW power. However, it does not reveal hot spots that may occur in regions of high SAR.

The gel used for the temperature pattern measurements is developed to exhibit the same electrical properties as saline. Its characteristics are well established with measurements of its complex permittivity. The adequacy of these measurements is in turn established with a good understanding of the theory and procedure used to make them.

The analysis of the monopoles reveal that the metal-tip monopole is the best geometry since its antenna current reaches a maximum near the tip and produces a fairly uniform SAR along its length. The heating uniformity is also confirmed by temperature measurements. The optimization of metal-tip monopoles suggests that no solution yields an ideal performance for ablation. The short, well-matched monopole has a non-uniform SAR while longer monopoles have a more uniform SAR but a poorer reflection coefficient. Unfortunately, this work cannot recommend the best practical metal-tip monopole for MW ablation and the author feels that *in vivo* measurements are required to resolve the issue. However, this study does offer valuable insight into the problem which would prove useful in the interpretation of *in vivo* trials. Microwave catheter ablation with these antennas may result in improved treatment of ventricular arrhythmias but further work is required to prove this.

The objectives of this work have been realized. A numerical model for the calculation of the reflection coefficient and SAR patterns of the antennas has been developed. Reliable experiments have been established to measure the reflection coefficient and temperature distribution of prototypes. The measurements were used to confirm the numerical results. Finally, the three monopole designs were characterized using simulation results and experimental measurements. A comparison of the antennas revealed the geometry that best meets the requirements of catheter ablation and an optimization of this geometry revealed the trade-off in varying the lengths of the antenna. The theoretical analysis of the monopole configurations has really shed some light on the behavior of insulated monopoles in lossy media having various terminations.

Bibliography

[1] A.C. Guyton, Human Physiology and Mechanisms of Disease, 5th ed., Toronto: W.B. Saunders Co., 1992.

[2] N. Palastanga, D. Field, R. Soames, Anatomy and Human Movement: Structure and Function, 2nd ed., Oxford: Butterworth-Heinemann Ltd, 1994.

[3] D.M. Considine, Editor, Van Nostrand's Scientific Encyclopedia, eighth edition, New York: Van Nostrand Reinhold, 1995, pp.226–229 and pp. 1553–1558.

[4] D.C. Gadsby, H. S. Karagueuzian, A.L. Wit. "Normal and abnormal electrical activity in cardiac cells," in W.J. Mandel, ed., Cardiac Arrhythmias: their mechanisms, diagnosis, and management. 3rd edition, Philadelphia: J.B. Lippincott Company, 1995, pp. 55–87.

[5] S. Labonté. A Theoretical Study of Radio-Frequency Ablation of the Myocardium. Doctoral Thesis, University of Ottawa, Electrical Engineering, 1992.

[6] I.D. McRury, D.E. Haines,"Ablation for the treatment of arrhythmias," *Proceedings of the IEEE*. Vol. 84, No. 3, March 1996, pp. 404–416.

[7] M. Brignole, C. Menozzi,"Control of rapid heart rate in patients with atrial fibrillation: drugs or ablation?," *Pace*, Vol. 19, March 1996, pp. 348–356.

[8] S. Nath, D.E. Haines, "Biophysics and pathology of catheter energy delivery systems," *Progress in Cardiovascular Diseases*, Vol. 37, No. 4, Jan/Feb 1995, pp. 185–204.

[9] G. Fontaine, M.M. Scheinman, eds., "Ablation in Cardiac Arrhythmias," Mount Kisco, NY: Futura Publishing Co., Inc., 1987.

[10] M.M. Scheinman, ed., "Catheter Ablation of Cardiac Arrhythmias," Boston: Martinus Nijhoff Publishing, 1988.

[11] A. Rosen, H. Rosen, eds., "New Frontiers in Medical Device Technology," New York: Jonh Wiley & Sons, Inc., 1995, pp. 61–77.

[12] E. Rowland, D. Cunningham, A. Ahsan, A. Rickards, "Transvenous ablation of atrioventricular conduction with a low energy power source," *British Heart Journal*, Vol. 62, No. 5, 1989, pp. 361–366.

[13] R. Lemery T.K. Leung, E. Lavallée, A. Girard, M. Talajic, D. Roy, M. Montpetit, "In vitro and in vivo effects within the coronary sinus of nonarcing shocks using a new system of low-energy DC ablation," *Circulation*. Vol. 83, No. 1, January 1991, pp. 279–293.

[14] G.H. Bardy, P.L. Sawyer, G. Johnson, T.D. Ivey, D.D. Reichenbach, "Effects of voltage and charge of electrical ablation pulses on canine myocardium," *American Journal of Physiology*, Vol. 26, No. 5, November 1989, pp. H1534-H1542.

[15] G.T. Evans, M.M. Scheinmann, the Executive Committee of the Registry, "The Percutaneous Cardiac Mapping and Ablation Registry: Final summary of results," *PACE*, Vol. 11, No. 11. 1988, pp. 1621-1626.

[16] S.K. Huang, Radiofrequency Catheter Ablation of Cardiac Arrhythmias: Basic Concepts and Clinical Application, Armonk, NY: Futura Publishing Company, Inc., 1995.

[17] M.M. Scheinman, ed., *Progress in Cardiovascular Diseases: Ablative therapy for cardiac arrhythmias*, Vol. 37, No. 4-5, Jan/Feb, Mar/Apr 1995.

[18] W.H. Kou, F. Morady, "Radiofrequency catheter ablation in the treatment of cardiac arrhythmias," in R.W. Schrier, F.M. Abboud, J.D. Baxter, A.S. Fauci, eds., "Advances in Internal Medicine," Vol. 40, Mosby—Year Book Inc., Toronto, 1995, pp. 533-571.

[19] G.N. Kay, V.J. Plumb, "The present role of radiofrequency catheter ablation in the management of cardiac arrhythmias," *The American Journal of Medicine*, Vol. 100, No. 3, March 1996, pp. 344-356.

[20] J.G. Whayne, S. Nath, D.E. Haines, "Microwave catheter ablation of the myocardium in vitro: Assessment of the characteristics of tissue heating and injury," *Circulation*, Vol. 89, No. 5, May 1994, pp. 2390-2395.

[21] A. Kadish, J. Goldberger, "Ablative therapy for atrioventricular nodal reentry arrhythmias," *Progress in Cardiovascular Diseases*, Vol. 37, No. 5, Mar/Apr 1995, pp. 273-294.

[22] L.S. Klein, W.M. Miles, "Ablative therapy for ventricular arrhythmias," *Progress in Cardiovascular Diseases*, Vol. 37, No. 4, Jan/Feb 1995, pp. 225-242.

[23] NASA-JSC Commercial Technology Opportunity, "Microwave heart catheter for treatment of cardiac arrhythmias," http://technology.jsc.nasa.gov/techops/hrtcath/hrtcath.htm.

[24] T. Satoh, P.R. Stauffer, "Implantable helical coil microwave antenna for interstitial hyperthermia," *International Journal of Hyperthermia*, Vol. 4, No. 5, 1988, pp. 497-512.

[25] R.L. Wonnell, P.R. Stauffer, J.J. Langberg, "Evaluation of microwave and radio frequency catheter ablation in a myocardium-equivalent phantom model," *IEEE Trans. on Biomedical Engineering*, Vol. 39, No. 10, Oct. 1992, pp. 1086-1095.

[26] D. Coggins, M. Chin, R. Wonnell, P. Stauffer, M. Scheinman, J. Langberg, "Efficacy of microwave energy for ventricular ablation," Abstract, *PACE*, Vol. 14, Part II, April 1991, p. 703.

[27] T.J. Cohen, D. Coggins, M.C. Chin, P. Stauffer, M.M. Scheinman, J.J. Langberg, "Microwave ablation of ventricular myocardium: the effects of varying duration on lesion volume," Abstract, *Circulation*, Vol. 84, Suppl. 2, 1991, p. 711.

[28] D.E. Haines, J.G. Whayne, "What is the radial temperature profile achieved during microwave catheter ablation with a helical coil antenna in canine myocardium?," Abstract, *Journal of the American College of Cardiology*, Vol. 19, No. 3, March 1992, p. 99A.

[29] J.J. Langberg, T. Wonnell, M.C. Chin, W. Finkbeiner, M. Scheinman, P. Stauffer, "Catheter ablation of the atrioventricular junction using a helical microwave antenna: a novel means of coupling energy to the endocardium," *PACE*, Vol. 14, No. 12, Dec. 1991, pp. 2105–2113.

[30] J.J. Langberg, K. Diehl, M. Gallagher, M. Harvey, A. Arbor, "Catheter modification of the AV junction using a microwave antenna," Abstract, *Journal of the American College of Cardiology*, Vol. 19, No. 3, March 1992, p. 26A.

[31] M.S. Mirotznik, N. Engheta, K.R. Foster, "Heating characteristics of thin helical antennas with conducting cores in a lossy medium — I: noninsulated antennas," *IEEE Trans. on Microwave Theory and Techniques*, Vol. 41, No. 11, Nov. 1993, pp. 1878–1886.

[32] L. Taylor, "Implantable radiators for cancer therapy by microwave hyperthermia," *Proceedings of the IEEE*, Vol. 68, No. 1, Jan. 1980, pp. 142–149.

[33] R.W. Paglione, "Miniature microwave antennas for inducing localized hyperthermia in human malignancies," *RCA Review*, Vo. 44, Dec. 1983, pp. 611–624.

[34] J.C. Lin, Y. Wang, "An implantable microwave antenna for interstitial hyperthermia," *Proceedings of the IEEE*, Vol. 75, No. 8, August 1987, pp. 1132–1133.

[35] J.C. Lin, Y.-L. Wang, R.J. Hariman, "Comparison of power deposition patterns produced by microwave and radio frequency cardiac ablation catheters," *Electronics Letters*, Vol. 30, No. 12, June 1994, pp. 922–923.

[36] J.C. Lin, K.J. Beckman, R.J. Hariman, S. Bharati, M. Lev, Y.-J. Wang, "Microwave ablation of the atrioventricular junction in open-chest dogs," *Bioelectromagnetics*, Vol. 16, 1995, pp. 97–105.

[37] J.C. Lin, Y.-J. Wang, "A catheter antenna for percutaneous microwave therapy," *Microwave and Optical Technology Letter*, Vol. 8, No. 2, Feb. 1995, pp. 70–72.

[38] J.C. Lin, Y.-J. Wang, "The cap-choke catheter antenna for microwave ablation treatment," *IEEE Trans. on Biomedical Engineering*, Vol. 43, No. 6, June 1996, pp. 657–660.

[39] R.M. Rosenbaum, A.J. Greenspon, S. Hsu, P. Walinsky, A. Rosen, "RF and microwave ablation for the treatment of ventricular tachycardia," *IEEE MTT-S International Microwave Symposium Digest*, Vol. 2, 1993, pp. 1155–1158.

[40] J.G. Whayne, S. Nath, D.E. Haines, "Microwave catheter ablation of myocardium in vitro: assessment of the characteristics of tissue heating and injury," *Circulation*, Vol. 89, No. 5, May 1994, pp. 2390–2395.

[41] T.H. Rho, M. Ito, H.P. Pride, B. Waller, D.P. Zipes, "Microwave ablation of canine atrial tachycardia induced by aconitine," *American Heart Journal*, Vol. 129, No. 5, May 1995, pp. 1021–1025.

[42] R.W.P. King, G.S. Smith, Antennas in Matter: Fundamentals, Theory, and Applications, Cambridge MA: The MIT Press, 1981.

[43] M. Oeff, J.J. Langberg, M.C. Chin, W.E. Finkbeimer, M.M. Scheinman, "Ablation of ventricular tachycardia using multiple sequential transcatheter application of radio-frequency energy," *PACE*, Vol. 15, Aug. 1992, pp. 1167–1176.

[44] R.W.P. King, B.S. Trembly, J.W. Strohbehn, "The electromagnetic field of an insulated antenna in a conduction or dielectric medium," *IEEE Trans. on Microwave Theory and Techniques*, Vol. MTT-31, No. 7, July 1983, pp. 574–583.

[45] J.P. Casey, R. Bansal, "The near field of an insulated dipole in a dissipative dielectric medium." *IEEE Trans. on Microwave Theory and Techniques*, Vol. MTT-34, No. 4, April 1986, pp. 459–463.

[46] Y. Zhang, N.V. Dubal, R. Takemoto-Hambleton, W.T. Joines, "The determination of the electromagnetic field and SAR pattern of an interstitial applicator in a dissipative dielectric medium." *IEEE Trans. on Microwave Theory and Techniques*, Vol. 36, No. 10, Oct. 1988, pp. 1438–1444.

[47] M.F. Iskander, A.M. Tumeh, "Design optimization of interstitial antennas," *IEEE Trans. on Biomedical Engineering*, Vol. 36, No. 2, Feb. 1989, pp. 238–246.

[48] A.M. Tumeh, M.F. Iskander, "Performance comparison of available interstitial antennnas for microwave hyperthermia," *IEEE Trans. on Microwave Theory and Techniques*, Vol. 37, No. 7, July 1989, pp. 1126–1133.

[49] G. Cerri, R. De Leo, V.M. Primiani, "'Thermic end-fire' interstitial applicator for microwave hyperthermia," *IEEE Trans. on Microwave Theory and Techniques*, Vol. 41, No. 6/7, June/July 1993, pp. 1135–1142.

[50] P. Walinsky, A. Rosen, A.J. Greenspon, Method and Apparatus for High Frequency Catheter Ablation, U.S. Patent Number 4,641,649, Feb. 10, 1987.

[51] S. Labonté, A.S.L. Tang, V.M. Walley, "Microwave ablation of the myocardium with a monopole antenna," *Proceedings of the 14th Annual International Conference of the IEEE Engineering in Medicine and Biology Society*, Part 2, 1992, pp. 713–714.

[52] H.P. Schawn, K.R. Foster, "RF-field interactions with biological systems: electrical properties and biophysical mechanisms," *Proceedings of the IEEE*, Vol. 68, 1980, pp. 104–113.

[53] A. Nyshadham, C.L. Sibbald, S.S. Stuchly, "Permittivity measurements using open-ended sensors and reference liquid calibration — an uncertainty analysis," *IEEE Trans. on Microwave Theory and Techniques*, Vol. MTT-40, No. 2, Feb. 1992, pp. 305–313.

[54] D.M. Pozar, Microwave Engineering, New York: Addison-Wesley Publishing Company, 1990.

[55] R.W.P. King, Tables of Antenna Characteristics, New York: IFI/Plenum, 1971.

[56] H.O Ali, G.I. Costache, "Accurate frequency domain modelling of coaxially driven axisymmetric microwave structures," *IEEE Microwave and Guided Wave Letters*, Vol. 4, No. 12, December 1994, pp. 390–392.

[57] O.C. Zienkiewicz, R.L. Taylor, Finite Element Method, 4th ed., vol. 2, New York: McGraw-Hill, 1989.

[58] D.S. Burnett, Finite Element Analysis: From Concepts to Applications, Reading, MA: Addison-Wesley, 1987.

[59] R.C. Boonton, Computational Methods for Electromagnetics and Microwaves, New York: John Wiley & Sons, 1992.

[60] P.P. Silvester, Finite Elements for Electrical Engineers, New York: Cambridge University Press, 1983.

[61] J. Jin, The Finite Element Method in Electromagnetics, Toronto: John Wiley & Sons, 1993.

[62] J.G. Maloney, G.S. Smith, W.R. Scott, "Accurate computation of the radiation from simple antennas using the Finite-Difference Time-Domain Method," *IEEE Trans. on Antennas and Propagation*, Vol. 38, July 1990, pp. 1059–1068.

[63] H.O. Ali, Finite Element Time-Domain Analysis of Axisymmetrical Radiating Structures, Master Thesis, University of Ottawa, Electrical Engineering, 1992.

[64] E. Sumbar, F.E. Vermeulen, F.S. Chute, "Implementation of radiation boundary conditions in the finite element analysis of electromagnetic wave propagation," *IEEE Trans. on Microwave Theory and Techniques*, Vol. 39, 1991, pp. 267–273.

[65] K.S. Kundert, Configuration Macro Definitions for Sparse Matrix Routines, U.C. Berkeley, 1993.

[66] K.S. Kundert, Sparse Fortran Module, U.C. Berkeley, 1993.

[67] C.K. Chou, G.W. Chen, A.W. Guy, K.H. Luk, "Formulas for preparing phantom muscle tissue at various radio frequencies," *Bioelectromagnetics*, Vol. 5, 1984, pp. 435–441.

[68] E. Kreyszig, Advanced Engineering Mathematics, Sixth Ed., Toronto: John Wiley & Sons, 1988, p. 986.

[69] W. Hurter, F. Reinhold, W.J. Lorenz, "A dipole antenna for interstitial hyperthermia," *IEEE Trans. on Microwave Theory and Techniques*, Vol. 39, No. 6, June 1991, pp. 1048–1054.

[70] S. Labonté, "A computer simulation of radio-frequency ablation of the endocardium," *IEEE Trans. on Biomedical Engineering*, Vol. 41, No. 9, Sept. 1994, pp. 883–889.

[71] A.R. Von Hippel, Dielectric Materials and Applications, Cambridge, MA: MIT Press, 1954.

[72] A. Stogryn, "Equations for Calculating the Dielectric Constant of Saline Water," *IEEE Trans. on Microwave Theory and Techniques*, Vol. MTT-19, Aug. 1971, pp. 733-736.

[73] A. Rosen, P. Walinsky, D. SMith, et al, "Percutaneous transluminal microwave angioplasty catheter," *IEEE MTT-S Digest*, Section D, 1989, pp. 167–170.

[74] Stuchly M.A., Stuchly S.S., "Permittivity of Mammalian Tissues in vivo and in vitro - Advances in experimental techniques and recent results," *International J. Electronics*, Vol. 56, No. 4, 1984, pp. 443-456.

[75] M.A. Stuchly, T.W. Athey, G.M. Samaras, G.E. Taylor, "Measurements of radio frequency permittivity of biological tissues with an open-ended coaxial line: part II experimental results," *IEEE Transactions on Microwave Theory and Techniques* , Vol. MTT-30, No. 1, January 1982, pp. 87-92.

[76] Athey T.W., Stuchly M.A., Stuchly S.S., "Measurement of Radio Frequency Permittivity of Biological Tissues with an Open-Ended Coaxial Line: Part I," *IEEE Trans. Microwave Theory Tech.*, Vol. MTT-30, No. 1, Jan. 1982, pp. 82-86.

[77] Gajda G.B., Stuchly S.S., "Numerical Analysis of Open-Ended Coaxial Lines," *IEEE Trans. Microwave Theory Tech.*, Vol. MTT-31, No.5, May 1983, pp.380-384.

[78] Misra D., Chabbra M., Epstein B. R., Mirotznik M., Foster K. R., "Noninvarsive Electrical Characterization of Materials at Microwave Frequencies Using an Open-Ended Coaxial Line: Test of an Improved Calibration Technique," *IEEE Trans. Microwave Theory Tech.*, Vol. 38, No. 1, Jan. 1990, pp. 8-14.

[79] Kraszewski A., Stuchly M.A., Stuchly S.S., "ANA Calibration Method of Dielectric Properties," *IEEE Trans. on Instr. and Measurement*, Vol IM-32, No. 2, June 1983, pp. 385-387.